University of Strathclyde

Department of Naval Architecture, Ocean and Marine Engineering

Structural Vibration Control of Fixed Offshore Wind Foundations

By

Arash Hemmati Topkanloo

A thesis submitted in fulfillment of the requirements for the degree of Doctor of Philosophy

Glasgow, U.K.

AUTHOR STATEMENT

This thesis is the result of the author's original research. It has been composed by the author and has not been previously submitted for examination which has led to the award of a degree.

Signed: Date:

ACKNOWLEDGEMENTS

I wish to express my sincere appreciation to those who have supported me during my PhD journey. First of all I want to thank my supervisor Dr. Erkan Oterkus. All his patience, the amount of his time he gave me and the level he finally made me reach are admirable. I am grateful to all the support, technical feedback, and opportunities he offered me to perform my research. I would like to thank Prof. Nigel Barltrop as my second supervisor, for his technical feedback and useful discussions over the course of my PhD.

I also would like to thank Dr Mahdi Khorasanchi (now at Sharif University) and Dr Narakorn Srinil (now at Newcastle University) for supervising my PhD.

I thank all the staff of the Naval Architecture, Ocean and Marine Engineering Department, and all my colleagues, which have always been collaborative, helpful and supportive, and have contributed in making the department a friendly and pleasant environment to work. Among the colleagues, I would like to thank Dr Saeid Lotfian, Dr Milad Armin, and Dr Dennj De for making the tea breaks more enjoyable.

The scholarship support of University of Strathclyde is acknowledged. In addition, I wish to acknowledge the financial support from the Institute of Marine Engineering, Science and Technology (IMarEST) for John Black Main postgraduate award.

I would also like to take this opportunity to thank Dr M. Amir Siddiq, my external viva examiner, for his constructive comments and suggestions.

Finally, I would like to say a heartfelt thank you to my family for always believing in me and encouraging me to follow my dreams. Words cannot express the feelings I have for my parents for their constant unconditional support. Their love and support helped me in overcoming the challenges I faced during my PhD.

” The scientist discovers a new type of material or energy and the engineer discovers a new use for it”

Gordon Lindsay Glegg

ABSTRACT

Due to the high flexibility of new offshore wind turbines (OWT) and dynamic content of the loading from wind, wave and earthquake applied to OWT systems, they are prone to excessive vibrations and this may result in serviceability issues as well as low fatigue lives of structural members. Therefore, control systems capable of mitigating undesired vibrations can help to reduce serviceability issues and increase fatigue lives. In this research, numerical models of jacket and monopile OWTs are developed and the effect of different types of vibration control devices such as Tuned Mass Dampers (TMDs) and Tuned Liquid Columns Dampers (TLCDs) on the dynamic responses of OWTs under various loadings is investigated. The dynamic responses are compared with those of the baseline system in which no vibration control device is used. Then, fragility analysis based on Multiple Stripe Analysis is performed to estimate the fragility reduction due to the implementation of vibration control devices. Different limit states for different equipment inside the nacelle are considered in the fragility analysis. The results show that the fragility reduction offered by the tuned liquid column dampers is higher for low-intensity earthquakes. In addition, the corresponding values for the parked condition are greater due to the lack of aerodynamic damping in this condition. Therefore, the implementation of an optimal TLCD can increase the overall reliability of the system, especially for parked conditions under low-intensity earthquake motions. Then a model for offshore wind turbine systems equipped with a semi-active time-variant tuned mass damper is developed considering nonlinear soil–pile interaction phenomenon and time-variant damage conditions. The adaptive concept of this tuned mass damper assumes a slow change in its structural properties. Stochastic wind and wave loadings in conjunction with ground motions are applied to the system. Damages to soil and tower caused by earthquake strokes are considered and the semi-active control device is retuned to the instantaneous frequency of the system using short-time Fourier transformation (STFT). The performance of semi-active time-variant vibration control is compared with its passive counterpart in operational and parked conditions. The results show that a semi-active mass damper with a mass ratio of 1% performs significantly better than a passive tuned mass damper with a mass ratio of 4%.

TABLE OF CONTENTS

LIST OF FIGURES

LIST OF TABLES

ABBREVIATIONS

OWT	Offshore Wind Turbines
TMD	Tuned Mass Dampers
TLD	Tuned Liquid Damper
TLCD	Tuned Liquid Column Damper
FEM	Finite Element Method
PSD	Power Spectrum Density
PGA	Peak Ground Acceleration
BEM	Beam Element Method
PTMD	Passive Tuned Mass Damper
STMD	Semi-Active Tuned Mass Damper
ATMD	Active Tuned Mass Damper
EOM	Equation of motion
MSA	Multiple Stripe Analysis
LC	Load Case
RNA	Rotor Nacelle Assembly
NREL	National Renewable Energy Laboratories
IM	Intensity Measure
IDA	Incremental Dynamic Analysis

STFT	Short-Time Fourier Transformation
JONSWAP	Joint North Sea Wave Observation Project
IEC	International Electrotechnical Commission
DNV	Det Norske Veritas

NOMENCLATURE

I_i	Area moment of inertia for each level of OWT jacket
I_{ij}	Area moment of inertia for each structural member at the each level
R	Radius of each member
T	Thickness of each member
θ	Angle between the member and the horizontal direction
K	Stiffness matrix
M	Mass matrix
X	Vector of amplitudes
ω	Natural frequencies of the system
ϕ	Angle of internal friction of soil
$J_x,\ J_y,\ J_z$	Area second moments of inertia
L_e	Original length of element from the start node to the end note
A_z	Cross section area of the element
G	Shear moduli
E	Young moduli
ρ	Material density
$K_{sx},\ K_{sy}$	Shear correction factors

p	Soil resistance acting against pile
y	Lateral deflection of pile
E_p	Young's module of elasticity of pile
I_P	Second moment of inertia of the pile,
E_s	Young's module of elasticity of soil
H	Depth of soil
p_u	Ultimate lateral bearing capacity
C_1 , C_2, C_3	Dimensionless factors
$\overline{v}(z)$	Mean velocity of wind
$\hat{v}(t)$	Turbulent wind velocity component
$\overline{v}$	Constant mean wind load
V_{ref}	Mean velocity at the reference height
H_{ref}	Reference height
z_0	Roughness length
L_k	Integral scale parameter
C_D	Drag coefficient
A_T	Total surface area of tower subjected to wind

W	Width of the body [m]
A	Surface area of the body [m^2]
$S_{v_k v_l}(f)$	Cross power spectral density function of wind velocity between locations k and l
$S_{v_k v_k}$, $S_{v_l v_l}$	Wind velocity auto spectra at points k and l
$Coh(k,l;f)$	Spatial coherence function
a	Coherence decrement
ν	Poisson's coefficient
L_c	Coherence scale parameter
C_d	Drag and inertia coefficients
C_m	Inertia coefficients
$\dot{\upsilon}$	Horizontal acceleration of water
υ	Velocity of fluid particles induced by wave excitations
g	Acceleration of gravity
γ	Peak enhancement factor
η	Function of water surface elevation
U_{10}	Mean wind velocity at 10 m from the sea surface
F	Fetch length
ϕ_f	Shape function of the offshore structure subjected to wave loading

B	Horizontal distance between two columns
u_L	Change in the elevation of the liquid inside the columns
u	Horizontal deflection at the base of TLCD
ξ	Non-linear coefficient of head loss
ψ	Opening ratio of the orifice (ratio of the diameter of the orifice to the diameter of the horizontal tube)
L_T	Total length of the tube
ω_L	Natural circular frequency of the TLCD
$P(t)$	N-dimensional vector of external force applied to the main structure
γ	Tuning ratio
μ	Mass ratio
m_{TLCD}	Mass of TLCD
R_σ	Reduction coefficient of standard deviation
$\sigma_{Uncontrolled}$	Standard deviation of fore-aft displacement of the top of tower without TLCDs
$\sigma_{Controlled}$	Standard deviation of fore-aft displacement of the top of tower with TLCDs
IM	Intensity measure
$\Phi(\bullet)$	Standard normal cumulative distribution function

θ	Median values of the fragility function
β	Standard deviation of *IM*
$\hat{x}(\tau)$	Weighted signal
τ	Moving time
ω_{id}	Dominant frequency
ω_{inst}	Instantaneous frequency
k_d^t	Time-variant stiffness of tuned mass damper

Chapter 1 Introduction

1.1 Introduction

Modern societies require larger quantities of energy and with a constantly increasing demand for energy and a higher level of public environmental concerns over conventional energy sources, wind energy has become the key part of renewable energy. Offshore wind energy is particularly becoming more popular due to steady and high wind speed, and less visual impact. Even though the offshore wind energy is constantly becoming more mature, the technology is still young and it faces technical and economic challenges. To increase benefits and reduce the costs, larger offshore wind turbines in deeper water depths are being designed and installed. These large wind turbines require larger foundations which are subjected to highly dynamic loading including wind, wave, current, and excitations due to the frequencies of the turbine itself in conjunction with seismic loading in places vulnerable to earthquake events such as New Zealand, Japan, China, and the USA. High flexibility and slenderness of offshore wind turbine foundations induced by the mentioned simultaneous loadings result in excessive vibrations and consequently high fatigue damage and serviceability issues. Therefore, these excessive vibrations need to be minimized to ensure the safety of these structures during their foreseen lifetime (20-25 years). One method to mitigate excessive vibrations is to use structural control devices installed in the wind turbine. In this chapter, a short discussion of offshore wind turbine foundations with an emphasis on the dynamic behaviour of the wind turbine and support structures is presented. Then, the objectives of the research are highlighted. Finally, the structure of the chapters in this dissertation is presented and a summary of the information contained in this chapter is given in the last section.

1.2 Offshore Wind-Trends

The constant increase in electricity consumption due to the improvement in lifestyles in modern societies can be identified in Fig. 1.1, where electricity consumption per capita rose from 2.06 MWh/capita to 3.11 MWh/capita during the period of 1990-2016 which means 51% increase over the period of 26 years [1]. This increase is anticipated to be sharper in the coming decades [1].

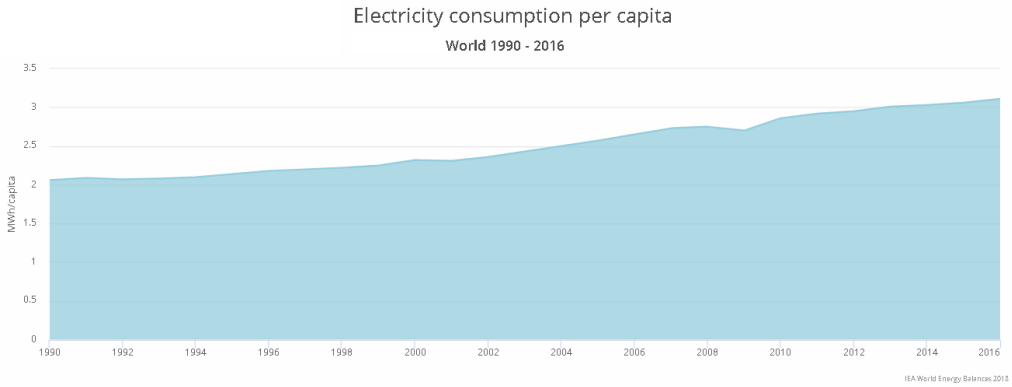

Figure 1.1 Electricity consumption per capita (1990-2016) [1]

As a result of new environmentally friendly policies of developed and developing countries, the electricity generation from renewable energy saw a steady increase from 1990-2016. Fig. 1.2 shows electricity generation from various sources of renewables from 1990-2016. The figure suggests that among different sources of renewable energy, wind energy experienced a very sharp rise from approximately 4000 GWh to 1000000 GWh [1]. This sharp increase in electricity generation from renewable energy can be linked to the increased price of fossil fuels and more incentives offered by the governments to invest in renewable energy. For the coming decades, the Energy Information Administration also predicted 69% increase in renewable electricity.

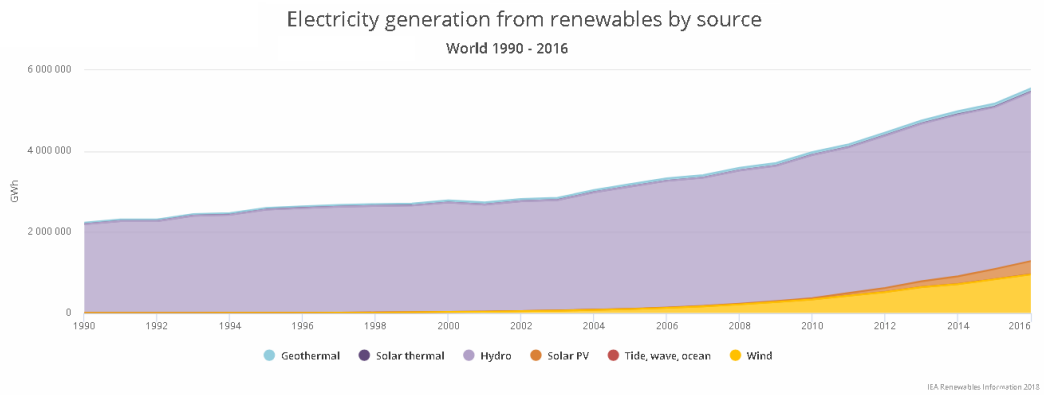

Figure 1.2 Electricity generation from renewables (1990-2016) [1]

Offshore wind is particularly gaining attention due to steady and high wind speed, and less visual impact. The capacity of the installed offshore wind turbines has increased more than three times over the past two decades as depicted in Fig 1.3 Not only the installed wind turbine capacity has increased but also the average size and rated power of newly-installed turbines have seen a tremendous increase. For example, the average capacity of the newly-installed turbines has grown from 4.8 MW in 2016 to 5.9 MW in 2017, with a 23% increase [2]. The current trend of offshore wind development shows that not only North sea countries are investing in offshore wind but also new areas including China, Taiwan, Australia, and Brazil are entering the market. However, Europe remains the largest offshore wind farm developer as 84% of all offshore installations were located in the North sea coasts [2]. Among these countries, the UK is the largest offshore wind market which accounts for more than one-third of the whole installed capacity. Based on the current trend and the anticipation of future trends, it is expected that the offshore wind sector is expanding and new wind turbines are being installed in deeper water depths and in diverse places not only in the less seismically active regions like the North Sea but also earthquake-prone areas such as China, US, and Korea.

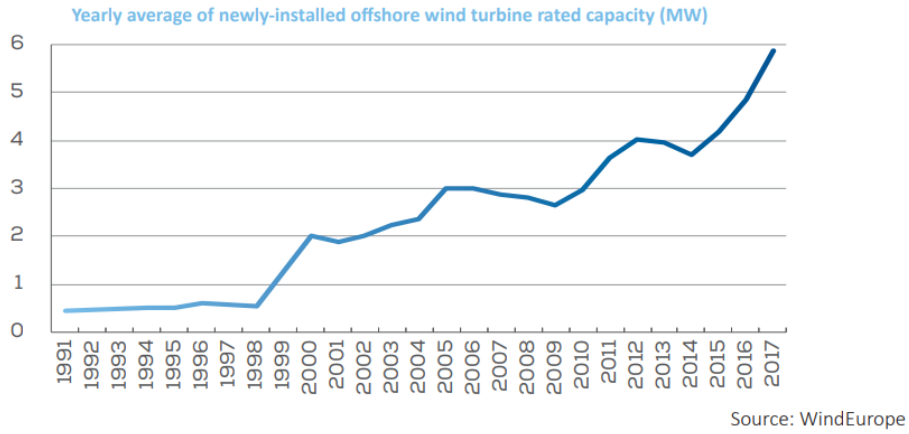

Figure 1.3 Yearly average of newly-installed offshore wind turbine rated capacity [2]

Fig 1.4 shows average water depth and distance to the shore of fixed offshore wind foundations and the size of bubbles indicates the overall capacity of the site. The blue bubbles represent online offshore wind turbines which were installed mostly in shallow and intermediate water depths. This figure clearly indicates that upcoming wind turbines tend to have larger capacities and to be installed in deeper water depths far from the coasts.

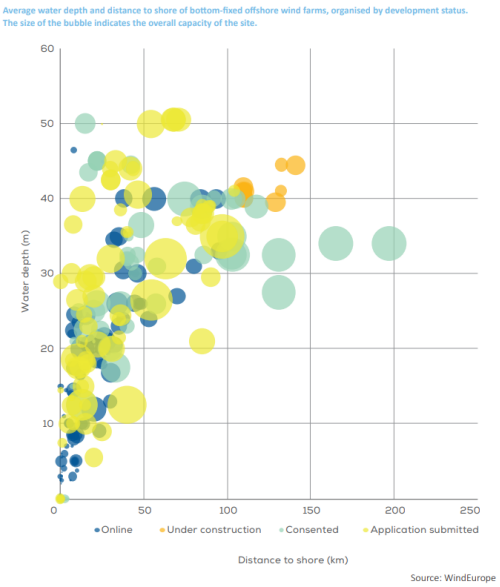

Figure 1.4 Average water depth and distance to the shore of fixed offshore wind farms [2]

However, this high growth in the size of wind turbines and increase in water depths of upcoming wind farms poses new challenges within the sector in terms of technicalities of large foundations. Since the nature of loading of offshore wind foundations is different from oil and gas foundations due to its large cyclic and horizontal forces, it is exposed to large dynamic loading resulting in large vibrations. These large vibrations cause risks in terms of serviceability and fatigue life. In terms of serviceability, large vibrations in the nacelle may increase downtime periods in which the equipment, generators, and machines in the nacelle should be switched off and this causes a reduction in the electricity generations. In terms of fatigue limit states, these large vibrations reduce fatigue lifetime of the foundations. Therefore, it is vital to mitigate these large vibrations using vibration control devices which have been developed in other fields such as civil engineering. This is the reason why this PhD dissertation aims to study the application of vibration control devices for offshore wind turbine foundations

1.3 Offshore Wind Foundations

While the configuration and layout of wind turbines including nacelle and towers usually remain the same for each wind farm and are manufactured by wind turbine manufacturers, the design and selection of offshore wind turbine foundations are governed by several other factors such as seabed conditions, geotechnical properties of soil, water depths, and hydrodynamic loadings. In general, the offshore wind foundations can be described as the entire structure from above the splash zone to below the seabed. The main function of offshore wind foundations is to transfer all horizontal and vertical loadings induced by wind, wave, current, seismic, and turbine excitations to the ground. Another function of offshore wind turbines is to support cables coming from the turbines and connect them to cable arrays on the seabed. Offshore wind foundations also give access to the turbine for maintenance using boat landing platforms. The offshore wind foundations should be designed in such a way that withstands the high dynamic loading. The design should also be cost-effective and practical in terms of fabrication and transportation. Considering these parameters,

various types of foundations have been developed and installed. Fig 1.5 shows the schematic configurations of five main offshore wind foundations in the industry. Because monopile and jacket foundations will most likely remain the dominant foundation types in foreseeable future, these foundation types are investigated through this study.

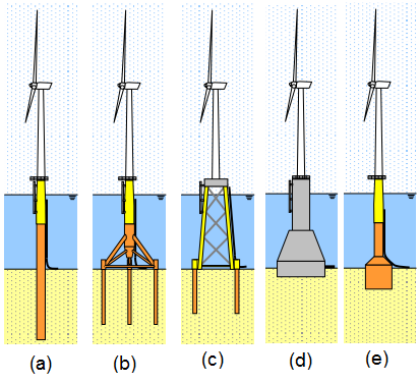

Figure 1.5 The main offshore wind foundation configurations a) Monopile b) Tripod c) Jacket d) Gravity Base e) Suction Bucket

1.3.1 Monopile

Monopile foundations consist of a single large diameter pipe which is either drilled or driven into the seabed. This is the simplest type of foundations which represent 81.7% of all installed substructures in Europe as shown in Fig 1.6 The main advantage of monopiles is their easy fabrication and installation. Furthermore, it does not require thorough seabed preparation. The tower is bolted to a transition piece which is attached to the monopile. The horizontal loading is transferred to the seabed by bending moment and passive soil resistance should be large enough to withstand the horizontal loading; otherwise, it may cause instability and collapse of the foundation. The vertical loading is transferred to the seabed through shaft friction as well as tip resistance. Although the simple configuration of this type of foundation made it reliable and economical, its disadvantage is that it is highly sensitive to the formation of scour and it may change

the fundamental natural frequency of the system which can affect the dynamic behaviour of the system. Furthermore, monopiles installed in seabeds with low soil resistances have smaller natural frequencies which may be close to the frequency of dominating wave and this can cause large excitations. Another disadvantage of monopiles is that they produce large hydrodynamic loading as wave loads increase drastically with the pile diameter. Difficulties due to limitations of pile driving equipment for large diameter monopile remain another challenge for this type of foundations. Therefore, the monopile concept might not be applicable beyond certain water depths and in seabed with weak geotechnical parameters.

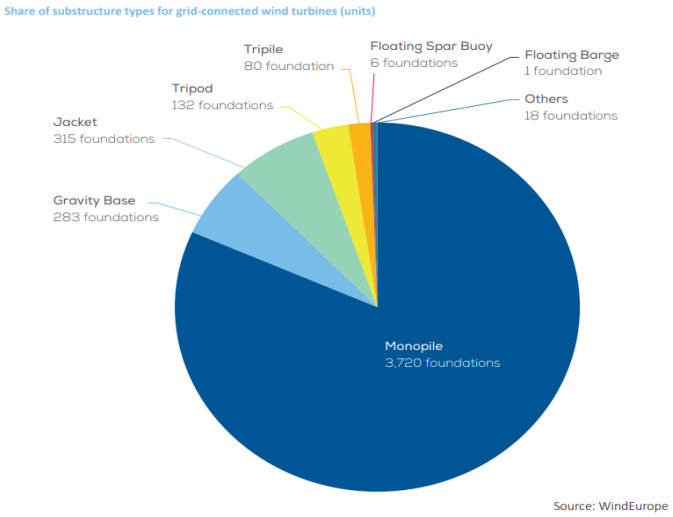

Figure 1.6 The share of foundation types for offshore wind farms in Europe [2]

1.3.2 Jacket

A jacket foundation is a bottom founded structure consisting of three or more legs connected by braces in a number of bays (bracing levels). Loads are mostly transferred in members in axial direction and the bracing system increases the stiffness of the foundation in the horizontal direction. The jacket foundations have been used

extensively in offshore oil and gas industry. However, the difference between the jacket used in oil and gas and the wind industry is that jackets in oil and gas must withstand large vertical loads from topside, however, the jackets in offshore wind must withstand large horizontal forces from wind, and wave. The main advantage of the jackets is that its multimember configuration makes it highly transparent to wave loading, resulting in smaller hydrodynamic loadings. It also has a larger resistance to overturning moments due to its large base especially in larger water depths. Furthermore, jackets are lighter and require less steel material compared to monopiles. The main disadvantage of this concept is that it requires high fabrication costs due to the need for complex design and welding at every single node. Transportation of this type of foundation to the wind farm is another important limitation as it requires a lot more space compared to monopiles especially while installing a large number of foundation for a wind farm. The jacket foundations can be fabricated in various types. Although the jacket foundations in the oil and gas industry normally have four, six or eight legs, the jackets in the offshore wind industry have a maximum of four legs. The jacket in the offshore wind industry can also have three legs; however, it requires more complicated welding due to the small angle between the legs. In this study, only four-legged jacket is considered as it is the most common type of jacket in offshore wind.

1.4 Objectives of research

The research described in this thesis has four main objectives:

- Creation of numerical models for offshore wind turbines (jackets and monopiles) equipped with vibration control devices in time domain considering non-linear soil-pile interaction. The jacket model is based on lumped mass modelling and the monopile is based on the Timoshenko beam theory.

- Performing some parametric studies for the developed models to investigate the effect of basic configurations on the modal properties of the system.

- Investigating the effect of different vibration control devices TMD, TLCD and the combined TLCD-TMD on the global behaviour of the offshore wind turbine system under various loading patterns (monotonous, impulse, harmonic, and stochastic).

- Performing fragility analysis for the uncontrolled and controlled offshore wind turbines and comparing the fragility reduction offered by the vibration control devices under multi-hazard loading (wind, wave, and seismic).

- Investigating the effect of implementation of semi-active vibration control devices on the overall behaviour of offshore wind turbines and comparing it with the passive vibration control devices.

1.5 Structure of the thesis

This thesis is constituted by the following seven chapters:

- Chapter 1. This chapter provides basic information about the current trend of the offshore wind industry in terms of water depth and turbine size, the technicalities and challenges of future offshore wind foundations. The objectives of research and the organization of this thesis are described.

- Chapter 2. This chapter provides the historical overview and literature review on the vibration control structures. It also provides the literature review on the offshore wind turbines under multi-hazard loading as well as fragility analysis of offshore wind foundations. A brief literature review on the soil pile interaction of offshore wind turbines is also provided. The need for vibration control of offshore wind turbines, which justify the need for further research in this field is provided. In this regard, the benefits of implementation of vibration control devices with a focus of the novelty of this research are highlighted.

- Chapter 3. This chapter provides basic information about numerical model utilized in this study for offshore wind monopiles and jackets. The multi lumped

mass modelling for jacket foundation is described and then a convergence study for jackets is presented. Verification study for the dynamic loading is included and some parametric studies on the effect of the main dimensions and configuration of the jacket on the natural frequencies are provided. Similarly, the finite element model for monopile foundation is described and a verification study is provided. Soil-pile interaction modelling and some studies on various models of soil-pile interaction considering diameter effects are provided. Finally, the stochastically generated wind, wave and seismic loadings used in the next sections are introduced.

- Chapter 4. In this chapter, a parametric study was provided that highlights the sensitivity of the structural control devices. The effect of tuned mass dampers (TMDs) and tuned liquid column dampers (TLCDs) on fixed offshore wind turbine foundations for the benchmark 5MW NREL turbine under various loading patterns were investigated. Also, the combined TLCD-TMD devices are studied. Then, the model subjected to stochastically generated wind loading in operational, parked, startup, and shutdown conditions are examined.

- Chapter 5. This chapter examines the effect of vibration control devices in the fragility of offshore wind turbines. A fragility analysis based on acceleration capacity thresholds is performed to estimate reliability improvement using the structural control devices. The fitted fragility functions based on multiple stripes analysis are constructed and compared with the empirical cumulative distribution curves.

- Chapter 6. This chapter describes the semi-active structural control of offshore wind turbines. A control algorithm for semi-active tuned mass dampers is explained. The damage development models for soil and tower is described and then the performance of semi-active time variant vibration control devices are compared to passive vibration control devices in operational and parked conditions.

- Chapter 7. This chapter reviews the research objectives, summarises the major findings, highlights the novelty and contribution to the field of this research study, discusses the gaps and the recommended future work, and closes with final remarks.

Chapter 2 Literature Review

2.1 Introduction

The scope of this chapter is to present a summary of the literature review undertaken for the realisation of this work. This research aims to investigate the effect of vibration control devices on the global behaviour of offshore wind turbine foundations under multi-hazards considering non-linear soil-pile interaction. Therefore, the literature review consists of five subsections. First, an overview of the literature review undertaken on the vibration control of offshore wind turbines with a focus on Tuned Mass Damper (TMD) and Tuned Liquid Dampers and various control algorithms is offered. Next, a literature review on the seismic analysis of offshore wind turbines with deterministic and probabilistic approaches is discussed. Furthermore, a historical overview of fragility analysis approaches is given. Then, the state of the art concerning the soil pile interaction modelling for offshore wind turbines is given. Finally, a summary of the information contained in this chapter is given in Section 2.7.

2.2 Vibration control

Vibration control systems developed in other fields such as civil and mechanical engineering can be used in offshore wind systems to mitigate the oscillation and consequently improve the lifetime and serviceability of the system. Three main structural control systems such as active, passive, and semi-active have been used in a number of structures. The applications and descriptions of these methods utilized in buildings and wind turbine structures were reviewed by Symans and Constantinou [3] and Chen and Georgakis [4]. Passive control systems can enhance structural damping, stiffness, and strength without employing force devices, complex sensors, and instrumental equipment. The vibrations are not tracked via sensors in this method as the properties of this system are constant. This method is widely used due to easy implementation and maintenance. The main outcome of using a passive control system is to minimize the oscillation of the system. Active vibration control system is a more

sophisticated method in which not only mechanical properties are adjusted in the time domain but also external forces are employed. Thus, the active control method requires the presence of active forces from external sources, resulting in high cost and complexity of the system. Active vibration control has also been studied for the application of wind turbines by a number of researchers [5-11]. Semi-active vibration control system is the modified version of the passive control system with the capability of adjusting the properties of the system in the time domain with respect to certain properties of vibration forces such as frequency content and amplitudes. Vibration amplitudes and frequencies are tracked down using sensors and signal processing techniques in order to adjust the structural properties. Therefore, the semi-active system optimizes vibration control capacity without employing external forces. In other words, semi-active system enjoys the best of both active and passive systems; therefore, it can be a more reliable and economically viable option for offshore wind turbines which are subjected to changes in their natural frequencies.

There are various damping devices such as tuned mass dampers, tuned liquid dampers, and fluid dampers. Tuned mass dampers have been implemented in tall buildings, towers and bridges and its effectiveness during earthquakes has been well proved [12]. Due to the simplicity and effectiveness of TMDs, they have been popular in the wind industry and there have been a number of studies focusing on wind turbine tower using TMDs [13-17]. One of the early studies in this field was done by Enevoldsen and Mørk [18] in which effects of passive tuned mass dampers on a 500 kW wind turbine were studied and a cost-effective design was achieved owing to the implementation of structural control devices. Later on, Murtagh et al. [19] investigated the use of tuned mass dampers (TMD) for mitigating along-wind vibrations of wind turbines. They concluded that the dynamic responses could be reduced providing that the device is tuned to the fundamental frequency. Stewart and Lackner [15] examined the impact of passive tuned mass dampers considering wind-wave misalignment on offshore wind turbine loads for monopile foundations. The results demonstrated that TMDs are efficient in damage reduction of towers, especially in side-side directions. Stewart and Lackner [16] in another study investigated the effectiveness of TMD systems for four

different types of platforms including monopile, barge, spar buoy, and tension-leg and they observed tower fatigue damage reductions of up to 20% for various TMD configurations. There have also been some investigations on the impact of TMDs on wind turbine blades [6, 7, 20].

Most studies of active control systems for wind turbines were focused on the vibration control of the blades. The use of active tuned mass dampers for control of in-plane vibrations of wind turbine blades was studied by [6] and they demonstrated promising results especially for high turbulent loadings. In addition, Brodersen et al. (2017) investigated the effect of an active tuned mass damper (ATMD) on the tower vibrations in frequency and time domains. The actuator force used in their study is controlled by the absolute displacement of the tower and the relative velocity of the damper mass. They concluded that the ATMD provides a considerable decrease in the frequency response. Their results showed that the ATMD is also superior in reducing the vibrations in transient conditions. Furthermore, Fitzgerald et al. [21] incorporated an ATMD into the tower of an onshore wind turbine and estimated the improved reliability of the system under stochastically generated wind loads. Their results showed a significant improvement in reliability of the system at the rated wind speed. The viability of application of semi-active tuned mass dampers to control undesired flapwise vibrations in wind turbine blades was investigated by [22]. They proposed a frequency-tracking algorithm based on the short-time Fourier transform technique in order to retune the frequency of the tuned mass damper. Furthermore, using multiple tuned mass dampers (MTMD) was proposed to improve the performance of vibration control systems [23]. They investigated the application of MTMDs for structural control of nacelle and tower of spar floating wind turbines and concluded that MTMDs are more efficient in displacement reductions. Then using MTMDs to control excessive vibration excited by higher modes of offshore wind turbine tower under multi-hazard was proposed by [24] and they concluded that installing the control devices along the tower improve the performance of the system.

More recently, Sun [25] explored semi-active tuned mass dampers for the NREL (National Renewable Energy Laboratory) 5 MW baseline wind turbine excited by

environmental loadings in conjunction with seismic motions considering post-earthquake damage to soil and tower stiffnesses. The author demonstrated the superiority of semi-active vibration control over the passive one in multi-hazard conditions. Although Sun's [29] work is well founded, it is limited to only one earthquake record (1994 Northridge Newhall 90) and further study for a group of earthquake records with different frequency contents and intensities is required. Another limitation of the aforementioned work is that soil–pile interaction was modeled using a simplified method (closed-form solution) in which the stiffness of embedded pile is considered with a constant rotation and lateral stiffness value in seabed level. More advanced soil–pile interaction model based on time-variant nonlinear stiffness considering soil damage phenomena can enhance the previous works. In addition, the effect of semi-active tuned mass dampers on other structural responses such as base shear and base moment should be investigated.

Tuned Liquid Column Dampers (TLCDs) are another popular vibration control system that has been used in civil engineering due to its easier maintenance requirements and costs. Bauer [26] was one of the first to propose using a container filled with liquids to mitigate the oscillation of a cantilever beam. The application of this kind of structural control device in buildings has been studied by [27, 28]. Fujino, Sun [29] and [30] further investigated the behavior of the fluid motion in an oscillating rectangular tank. With regard to optimization of TLCDs, Yalla and Kareem [31] proposed a new approach to find the optimal parameters of tuned liquid column dampers in order to improve their performance. The effectiveness of TLCDs in structural control of wind turbine systems has been studied by a number of researchers [32-36]. Ghaemmaghami, Kianoush [32] concluded that tuned liquid dampers are effective for small amplitude excitations. Colwell and Basu [33] studied effects of TLCD on offshore wind turbine systems to suppress the excessive vibration and found that TLCD can minimize vibration up to 55% of peak response compared to the uncontrolled system. There have also been studies on the effectiveness of TLCD on vibration suppression of wind turbine blades that achieved improved results [34, 35]. Karimi et al. [37] proposed a controllable valve in tuned liquid column dampers for the

application of offshore wind turbines. In addition, the use of semi-active tuned mass dampers in control of flapwise vibrations of wind turbines was examined by Arrigan [22]. The authors proposed a frequency-tracking algorithm for retuning the vibration control device and they observed significant vibration reductions owing to the semi-active mechanism. Semi-active control mechanism for tuned liquid column dampers (TLCDs) was also studied by Sonmez et al. [38]. The authors used a control algorithm based on short-time Fourier transformation (STFT) and investigated the effectiveness of the proposed device under random excitations.

Mensah and Dueñas-Osorio [36] investigated reliability improvement of an onshore wind turbine system using TLCD and their results show a considerable reduction in displacement and bending moment in the tower. Although their findings are comprehensive, their work is limited to onshore wind turbines and a study focusing on reliability improvements of offshore wind turbines offered by structural control devices is needed as offshore wind turbines face larger environmental loadings and consequently lower reliability levels. Furthermore, their work is limited to reliability analysis for only wind and wave loading for places located with low risk of earthquake events in which the seismic loading can be ignored in the reliability analysis. However, more wind turbines are being installed in earthquake-prone places and including seismic excitations in the structural analysis of wind turbines is becoming more necessary.

2.3 Seismic

Due to the fact that the wind farms developed in the last two decades were located in the places where earthquake events rarely occur, few studies considering seismic loading have been performed. Prowell et al. [39, 40] and Zhao et al. [41, 42] studied the behavior of onshore wind turbines under seismic excitations using nonlinear time domain simulations based on multi-body dynamic formulations. Prowell et al. [39, 40] claimed that seismic bending moment demand at the base of the tower is considerably above the demand from other extreme events such as extreme wind under various

operational and non-operational conditions and the seismic design consideration may be a design driving factor for large wind turbines. Zhao et al. [41, 42] concluded that force and bending moment at the base of the structure are highly affected by even weak seismic excitations especially in the side-side direction where aerodynamic loading is lacking.

There have been two main approaches regarding seismic hazards in wind turbines: deterministic and probabilistic. Bazeos et al. [43] performed both deterministic and probabilistic analyses for wind turbines subjected to seismic loading and observed similar results for two analysis methods. They investigated the seismic behaviour of a 37 m high wind turbine's tower. In that study, first a refined finite element model for the tower was analysed using the elastic spectrum. Then, the tower was analysed using response history analysis method in which six seismic accelerograms based on the code spectrum were applied to the tower and they observed almost identical results (displacements and accelerations at the tower's top). Witcher [44] conducted time domain simulation for wind turbines considering full aeroelasticity of GH Bladed wind turbine simulation package under turbulent wind loading in conjunction with seismic loading. Song et al. [45] investigated the dynamic response of offshore wind turbine tower supported by a monopile under seismic loading. They analysed the dynamic response of the system under different seismic waves using M method which simulates the soil pile interaction by assuming that resistance of soil increases linearly with increase in depth. They concluded that the inclusion of the earthquake ground motions for the reliability of a wind turbine is necessary. Furthermore, their results show that the dynamic responses were more affected under the far-field seismic wave due to the slenderness of offshore wind turbine foundations [45]. In addition, Alati et al. [46] investigated the impact of seismic motion on tripod and jacket foundations for offshore wind turbines considering operational conditions. They performed fully coupled nonlinear time simulations using three-dimensional models considering soil-pile interaction. The results of the aforementioned research showed that the contribution of seismic loading increased the overall dynamic responses of the system considerably even for moderate seismic records. Furthermore, they concluded that higher dynamic

structural responses are observed for multi-hazard conditions compared to the results from typical design load cases which are prescribed by the relevant design standards such as IEC [47]. They confirmed that the seismic design load is the dominating design driver. As the results of the aforementioned studies are limited to one particular offshore wind turbine under particular loading conditions and seismic records, more studies concerning the behaviour of offshore wind turbines under multi-hazard condition are necessary.

Jin et al. [48] studied the seismic behavior of wind turbines using an integrated multi-body system and concluded that the power production is threatened when there is a sudden earthquake during the operational time. With regard to the probabilistic approach for seismic loading, fewer studies can be found. Nuta et al. [49] conducted research on probabilistic assessment of seismic induced wind turbines using an incremental dynamic analysis procedure (IDA) and generated probabilistic estimations for various Damage Stages (DS). Furthermore, Mardfekri and Gardoni [50] developed a probabilistic model under the multi-hazard condition of the offshore wind turbine and analyzed the reliability of the wind turbines. This study covered a wide range of structural characteristics for the operational wind turbine using the annual occurrence probability of the hazards and claimed that the actual probability of failure is higher than the target safety recommended by standards. Kim et al. [51] investigated the responses of the NREL 5MW wind turbine on a monopile under real and artificial seismic excitation using a simplified lumped mass model including nonlinear springs representing soil-pile interaction. They proposed that the fragility curves for various peak ground accelerations (PGAs) can be constructed by static pushover analysis. The fragility analyses performed in the previous studies were mostly based on conventional methods. Baker [52] investigated the effectiveness of various methods for fragility analysis under seismic loading based on drift threshold for general structures and showed that multiple stripe analysis produces more efficient fragility functions compared to other conventional methods. However, the applicability of this method for offshore wind turbines under multi-hazard condition should be investigated.

2.4 Soil-Pile Interaction

Soil-pile interaction of fixed offshore wind foundations is a key parameter in the design as it affects dynamic behaviour of the system in terms of natural frequency analysis and fatigue analysis. The dynamic soil-pile interaction is dependent on the nature of the loading as well as the mechanical properties of soil and structural properties of the pile. The development of offshore wind piles have been driven mostly based on the approaches and experience in offshore oil and gas industry. There are various approaches concerning soil pile interaction of offshore wind turbines. Jalbi et. al [53] introduced various practical methods to model the soil-pile interaction of offshore wind turbine foundations. Zaaijer [54] also utilized a number of approaches to model soil pile interaction and compared the numerical results with the measured data. The approaches used in Zaaijer's work [54] are distributed springs, apparent fixity length, stiffness matrix, and uncoupled springs. In the aforementioned study, the results of the five offshore wind matched with the expected result from the models, however, the measured data from two wind turbines showed high inaccuracy. Bush and Manuel [55] investigated two approaches as apparent fixity and distributed spring for modelling soil pile interaction of offshore wind turbines. In the apparent fixity model, the soil pile interaction model is replaced by a continuous cylinder which is fixed at the point of apparent fixity. The apparent fixity length, which is defined as the depth below seabed where the cylinder is assumed to be fixed, is dependent on the soil properties, pile properties and magnitude of the loading applied to the foundation. The distributed spring model consists of the exact length of the pile which is supported by soil layers which are modelled by elastic springs. They concluded that the application of these two models leads to larger extreme loads compared to the fixed model.

Winkler modelling approach is another method to model the soil-pile interaction. In this method, soil is regarded as a series of discrete springs which are mutually independent [56]. The uncertainty about this approach arises from the uncertainty of the mechanical properties of soil and nonlinear behaviour due to soil degradation, and the cyclic nature of loading. With regard to small-displacement vibration which

corresponds to the natural frequency analysis of offshore wind turbines, recent data from various measurement campaigns conducted in a number of offshore wind farms suggests that soil stiffness prescribed by offshore standards [57] gives errors in natural frequency prediction due to the fact that most of the soil stiffness parameters were based on the measurements and experiments on the offshore oil and gas piles. Therefore, there have been various studies conducted to modify the soil stiffness for the application of offshore wind [58-61]. In the next section, various stiffness models for natural frequency analysis as well as nonlinear soil pile interaction model based on p-y curves for dynamic analysis will be discussed.

2.5 Summary

The historical overview of studies concerning the implementation of various vibration control devices in wind turbine systems has been given. Various types of control algorithm of vibration control devices such as passive, semi-active and active are introduced. The application of tuned mass dampers (TMDs) and tuned liquid column dampers (TLCDs) in the wind turbines are discussed. Then, the historical overview of research works about seismic considerations in offshore wind turbines is given. Two most common types of seismic analysis for wind turbine systems are discussed. The state of the art of deterministic and probabilistic approaches to consider seismic loading in the offshore wind turbine systems is explained. Finally, a brief review of the soil pile interaction models for offshore wind foundations is given. The following list summarises the findings that are of most relevance to this research:

- The dynamic responses of offshore wind foundations equipped with vibration control devices could be reduced providing that the device is tuned to the fundamental frequency of the system.

- Tuned mass dampers are efficient in damage reduction of towers, especially in side-side directions.

- Active tuned mass dampers are superior in reducing the vibrations in transient conditions.
- Tuned liquid dampers are effective for small amplitude excitations.
- Frequency-tracking algorithm for retuning the vibration control device can be used and the significant vibration reduction can be obtained.
- Under seismic excitation, the contribution of seismic loading in the bending moment at the base of the tower is considerably higher than the contribution of the other excitation sources in extreme conditions under various operational and non-operational conditions.
- Power production is considerably threatened when there is a sudden earthquake during the operational conditions.
- Seismic design consideration may be a design driving factor for large wind turbines.

Chapter 3 Modelling and Formulation

3.1 Introduction

In this chapter, the structural model for jacket and monopile foundations are described. The jacket foundation model is based on lumped mass modelling and the monopile foundation is established based on the Timoshenko modelling. The convergence study is performed for these two models. Then, verification study for natural frequency analysis as well as nonlinear dynamic analysis is discussed. Some parametric studies are performed to investigate the effects of the main dimensions and configurations on the natural frequencies and mode shapes. Furthermore, the nonlinear soil pile interaction model adopted in this study is described. The different soil pile interaction models which account for the diameter effect have been examined. Finally, the definition of various loading such as wind, wave and seismic used in the next sections is described.

3.2 Jacket modelling (Lumped mass modelling)

The stiffness and mass matrices were built using a system based on the multi-degree-of-freedom lumped-mass model in which the complete offshore wind turbine system includes the piling system, jacket substructure, transition piece, tower, hub, and blades as depicted in Fig. 3.1.

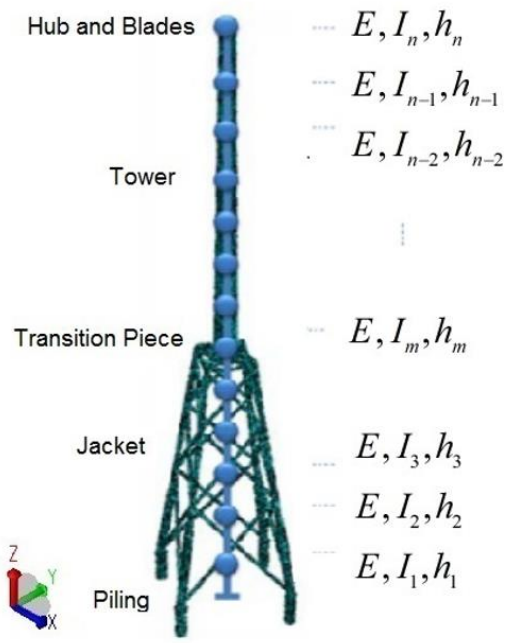

Figure 3.1 3-D schematic configuration of offshore wind turbine system

For each level, the area moment of inertia I_i contributed by all the vertical members of the structure can be expressed as:

$$I_i = \sum I_{ij} \tag{3.1}$$

where I_{ij} is the area moment of inertia for each structural member at the same level. For each member such as jacket leg/brace and tower, the area moment of inertia can be obtained as

$$I_{ij} = \frac{\pi}{4}(R^4 - (R-T)^4) \times \cos(\theta) \tag{3.2}$$

in which R and T are the radius and thickness of the member; θ is the angle between the longitudinal direction of the member and the horizontal direction. The stiffness matrix is based on the discrete system for a multi-degree-of-freedom system made of *n* masses as following:

$$[K_s]=\begin{bmatrix}
E\left(\frac{3I_1}{h_1^3}+\frac{4I_2}{h_2^3}+\frac{I_3}{h_3^3}\right) & -2E\left(\frac{I_1}{h_1^3}+\frac{I_2}{h_2^3}\right) & E\frac{I_2}{h_2^3} & 0 & 0 & 0 & \cdots & \cdots & 0 \\
-2E\left(\frac{I_1}{h_1^3}+\frac{I_2}{h_2^3}\right) & E\left(\frac{I_2}{h_2^3}+\frac{4I_3}{h_3^3}+\frac{I_4}{h_4^3}\right) & -2E\left(\frac{I_2}{h_2^3}+\frac{I_3}{h_3^3}\right) & E\frac{I_3}{h_3^3} & 0 & 0 & \ddots & \ddots & \vdots \\
E\frac{I_2}{h_2^3} & -2E\left(\frac{I_2}{h_2^3}+\frac{I_3}{h_3^3}\right) & E\left(\frac{I_3}{h_3^3}+\frac{4I_4}{h_4^3}+\frac{I_5}{h_5^3}\right) & \ddots & \ddots & \ddots & \ddots & \ddots & \vdots \\
0 & E\frac{I_3}{h_3^3} & \ddots & \ddots & \ddots & \ddots & \ddots & \ddots & \vdots \\
\vdots & 0 & \ddots & \ddots & \ddots & \ddots & \ddots & E\frac{I_{N-2}}{h_{N-2}^3} & \vdots \\
\vdots & \vdots & \ddots & \ddots & \ddots & \ddots & \ddots & \ddots & \vdots \\
\vdots & \vdots & \ddots & \ddots & \ddots & -2E\left(\frac{I_{N-3}}{h_{N-3}^3}+\frac{I_{N-2}}{h_{N-2}^3}\right) & E\left(\frac{I_{N-2}}{h_{N-2}^3}+\frac{4I_{N-1}}{h_{N-1}^3}+\frac{I_N}{h_N^3}\right) & -2E\left(\frac{I_{N-2}}{h_{N-2}^3}+\frac{I_{N-1}}{h_{N-1}^3}\right) & E\frac{I_{N-1}}{h_{N-1}^3} \\
\vdots & \vdots & \ddots & \ddots & \ddots & E\frac{I_{N-2}}{h_{N-2}^3} & -2E\left(\frac{I_{N-2}}{h_{N-2}^3}+\frac{I_{N-1}}{h_{N-1}^3}\right) & E\left(\frac{I_{N-1}}{h_{N-1}^3}+\frac{4I_N}{h_N^3}\right) & -2E\frac{I_N}{h_N^3} \\
\vdots & 0 & \cdots & \cdots & \cdots & 0 & E\frac{I_{N-1}}{h_{N-1}^3} & -2E\frac{I_N}{h_N^3} & E\frac{I_N}{h_N^3}
\end{bmatrix} \tag{3.3}$$

The mass matrix is obtained based on the method of distribution of the masses as by multiplying the height and mass density. The mass matrix can be expressed as:

$$[M_s]=\begin{bmatrix}
m_1 & 0 & 0 & \cdots & \cdots & 0 & 0 \\
0 & m_2 & 0 & & & & \vdots \\
0 & 0 & m_3 & \ddots & & & \vdots \\
\vdots & & \ddots & \ddots & \ddots & & \vdots \\
\vdots & & & \ddots & \ddots & 0 & 0 \\
\vdots & & & & 0 & m_{N-1} & 0 \\
0 & 0 & \cdots & \cdots & 0 & 0 & m_N
\end{bmatrix} \tag{3.4}$$

Table 3.1 tabulates the material properties of the steel used in the tower and jacket of the offshore wind turbine. The density of the steel in the tower is taken 8 % higher than that of the steel to take into account the weight of the paint, bolts, welds, and flanges which are not modeled directly [62].

Table 3.1 Material properties of jacket

Component	Density (kg/m^3)	Young's modulus (GPa)	Poisson's ratio
Tower	8500	210	0.3
Jacket	7850	210	0.3

The free vibration analysis of a multi-degrees of freedom (MDOF) system for the case of undamped condition can be expressed by the following equation.

$$[K]\{X\} - \omega^2 [M]\{X\} = 0 \tag{3.5}$$

in which *K* is the stiffness matrix, *M* is the mass matrix, *X* is the vector of amplitudes, and ω is the natural frequencies of the system. To solve this equation, the determinant of the coefficient matrix should be to equal to zero:

$$\left|[K] - \omega^2 [M]\right| = 0 \tag{3.6}$$

The above equation is called the characteristic equation [63]. The motion equation of the system can be described as:

$$[M]\{\ddot{X}\} + C\{\dot{X}\} + [K]\{X\} = F(t) \tag{3.7}$$

in which *C* is damping matrix and *F(t)* is applied loading matrix in time domain.

3.2.1 Turbine Model Description

In this study, NREL 5 MW wind turbine was considered as it is widely used as the turbine for benchmark studies [64]. This turbine is supported by baseline jacket foundation designed during the UpWind project [65]. The general configuration of the turbine is shown in Fig 3.2 and its particulars can be found in Table 3.2.

Table 3.2 Properties of NREL 5MW baseline turbine

Rating	5MW
Rotor Orientation	UpWind, 3 Blades
Control System	Variable Speed, Collective Pitch
Rotor, Hub Diameter	126.0 m, 3.0 m
Hub Height	90.0 m
Cut-In, Rated, Cut-Out Wind Speed	3 m/s, 11.4 m/s, 25 m/s
Cut-In, Rated Rotor Speed	6.9 rpm, 12.1 rpm
Rotor Mass, Nacelle Mass	110,000 kg, 240,000 kg
Nacelle Dimensions	18 m*6 m *6 m

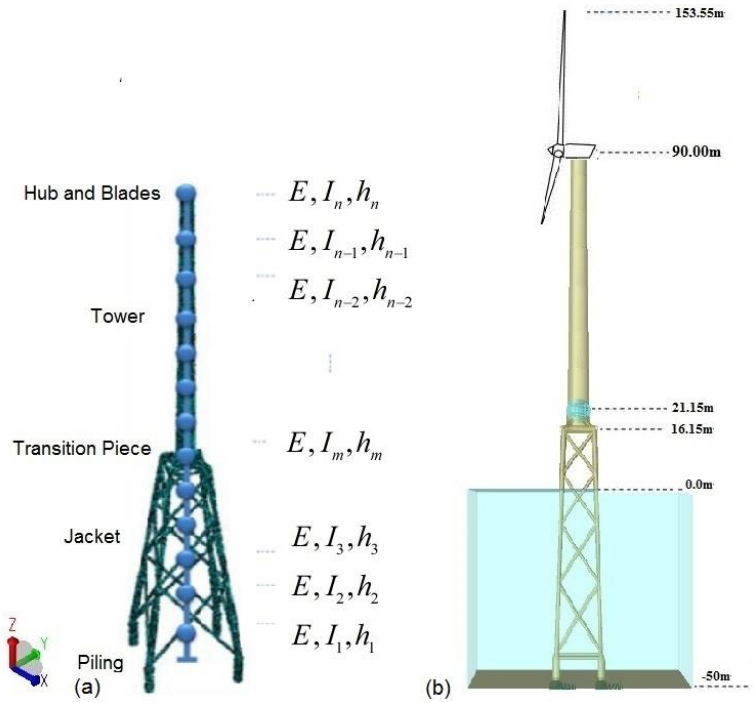

Figure 3.2 (a) 3-D schematic (b) configuration dimensions of the offshore wind turbine system

3.2.2 Convergence test

The main concept of application of lumped-mass modeling for multi-member structures like jackets is that the whole structure is divided into discrete sections as lumped massed in order to simplify the model and reduce computation efforts. However, the number of lumped mass used in the analysis is the main factor in accuracy and computational efficiency of the system. Therefore, there should be a balance between these two by finding the optimised number of lumped mass in which high accuracy is achieved by the minimum number of lumped masses. Using the convergence study, the question of how many masses are needed can be answered. It is vital to perform convergence study with the increasing number of masses. The number of masses can be considered to be sufficient provided that the interested results (for example natural frequency) remain almost unchanged for the number of masses larger than the previous ones. For convergence study, the number of masses is increased from 30 to 2000. As can be seen

in Fig 3.3, the first and second natural frequencies do not change by a large percentage for the models with the number of masses higher than 360.

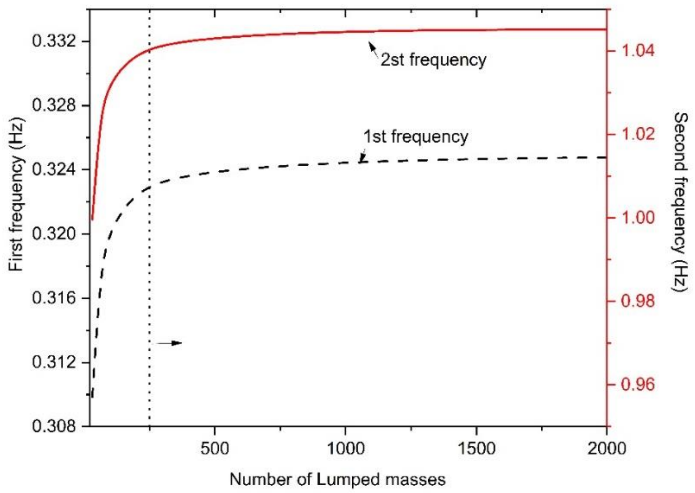

Figure 3.3 Natural frequency variation with change in the number of lumped masses

Table 3.3 tabulates first and second natural frequencies of the system with various number of masses. As can be seen in the table, first and second natural frequencies do not change considerably after 360 number of masses.

Table 3.3 Natural frequencies for convergence test of lumped mass model for jacket OWT

Number of masses	First natural frequency (Hz)	Second natural frequency(Hz)
30	0.30985	0.99967
60	0.31757	1.02452
90	0.32008	1.03196
180	0.32261	1.03941
360	0.32389	1.04313
2000	0.32481	1.04569

Fig 3.4 shows the first four mode shapes of the system for different number of masses. As can be seen in the figure, the mode shapes become smoother with the increase in the number of masses. The mode shapes captured by finite element models(SESAM) are also shown in Fig 3.5. The figures are shown to compare the mode shapes qualitatively

in terms of location of maximum deflections. The first three mode shapes show better match with the lumped mass model and as the first two mode shapes contribution to dynamic behaviour of the fixed foundations are much higher than the rest of mode shapes, modelling the whole jacket with lumped masses give acceptable dynamic results.

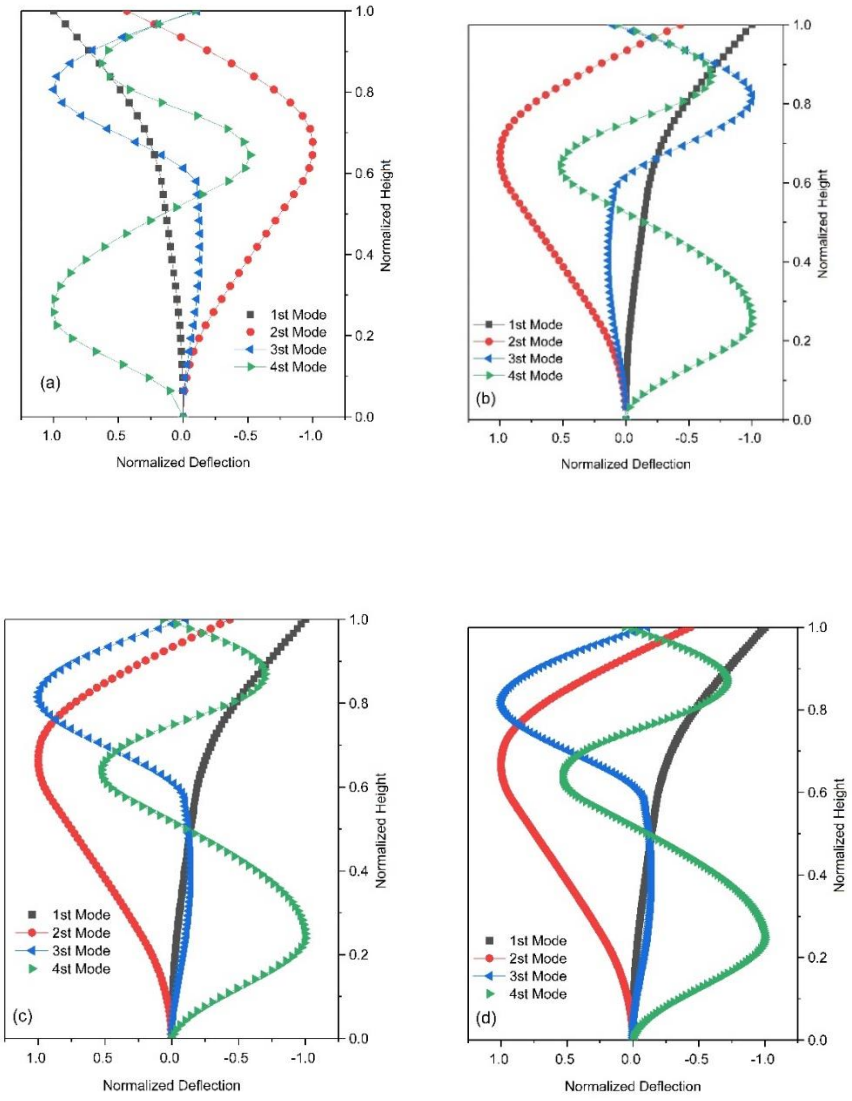

Figure 3.4 Mode shapes of the lumped mass model with a) 30 b) 60 c) 90 d)180 number of masses

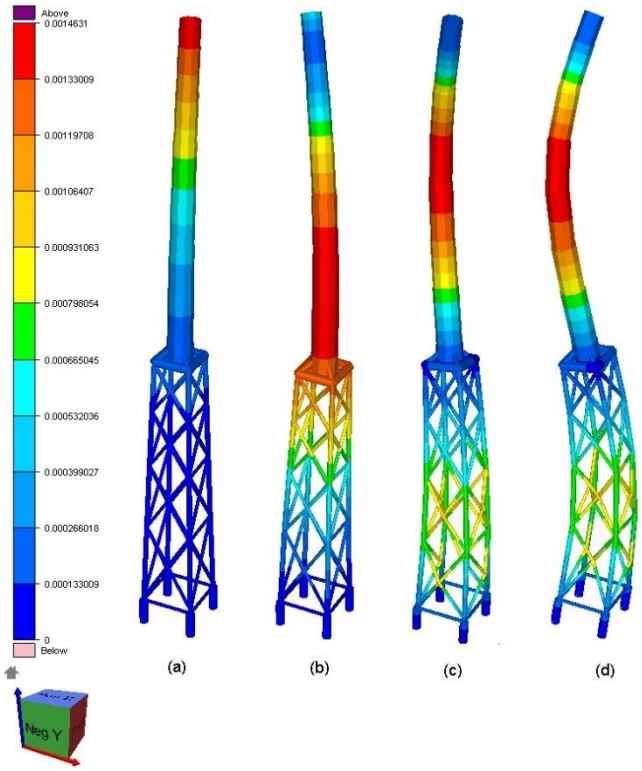

Figure 3.5 Mode shapes obtained by finite element method (SESAM) a) first modal shape; b) second modal shape c) third modal shape d) fourth modal shape

Since a higher number of masses in the lumped mass model requires more calculation time, it is necessary to find a minimum number of lumped masses that fulfill the requirement of accuracy and convergence. From Fig 3.6 in which computation time is plotted for a different number of masses, it can be concluded that computation time for a natural frequency analysis is only 0.1 second run using a normal personal computer when the results converge with 360 lumped masses. This highlights the high computation efficiency of the proposed model for jackets.

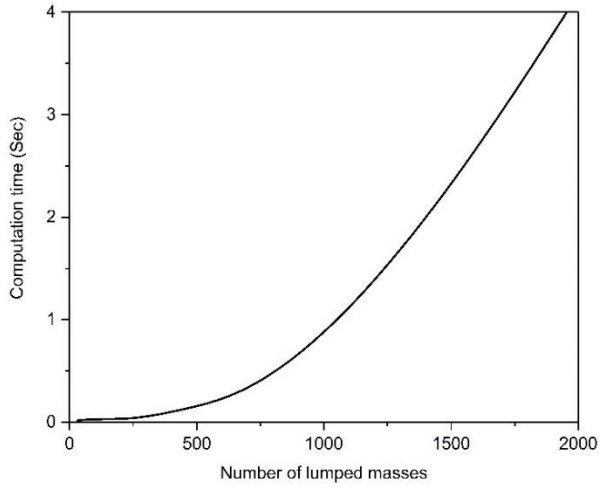

Figure 3.6 Computation time of performing one natural frequency analysis vs number of lumped masses

3.2.3 Parametric Study

3.2.3.1 Natural frequency analysis

The fundamental free vibration analysis is performed for the jacket model using both the developed code in MATLAB and commercial software package (SESAM). Fig 3.7 shows the first two natural frequencies calculated by two methods as a function of the leg thicknesses. From the results, it can be concluded that there is a good agreement between the results of the lumped mass model and the finite element model. Looking into the differences between the results in Fig 3.8, it can be demonstrated that a maximum error of 3% is experienced because of the simplified model of lump mass. This error is attributed to the difference in modelling the jacket in which multi-member configuration are simplified with lumped mass modelling.

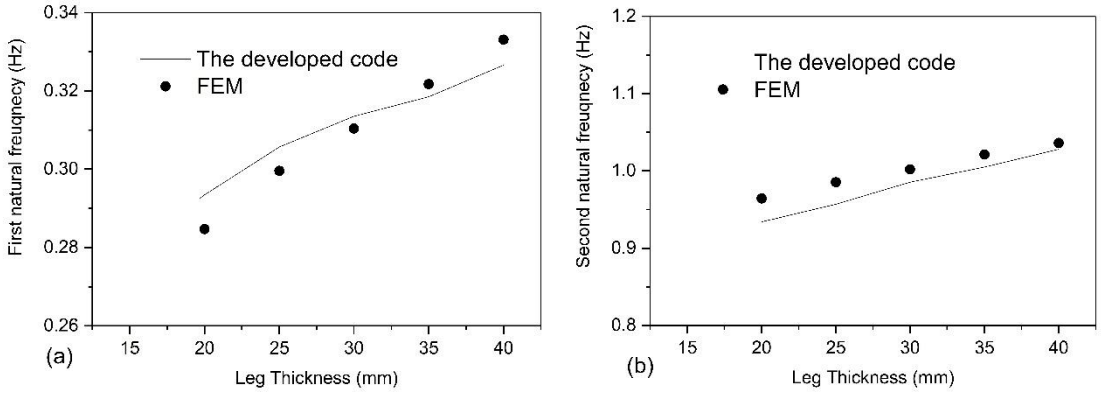

Figure 3.7 Natural frequencies for wind turbine jacket as a function of leg thickness by the developed code (line) and FEM (dots) a) first natural frequency b) second natural frequency

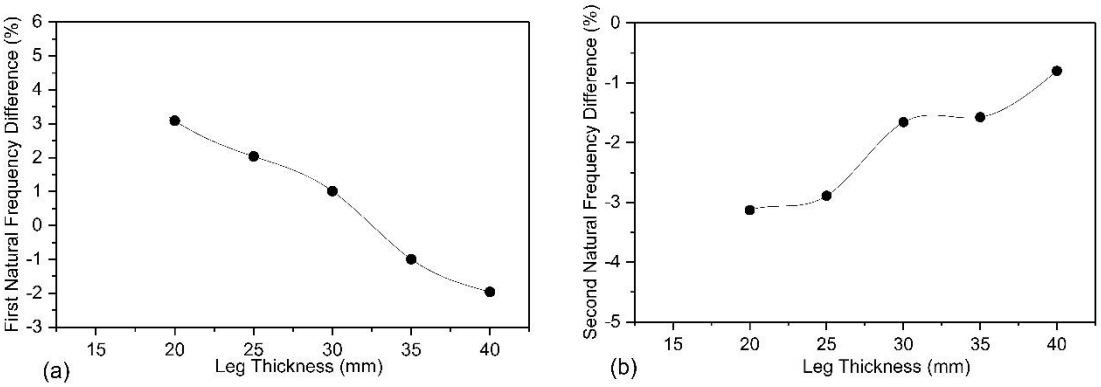

Figure 3.8 Natural frequency difference between the developed code & FEM a) first natural frequency b) second natural frequency

The parametric study on the effects of configurations of the jacket on the natural frequencies is conducted by the developed code using a lumped mass model. The first two natural frequencies of the offshore wind turbine system as a function of leg radius are shown in Fig 3.9. It can be seen that the first two natural frequencies increase slightly with increasing leg radius and this increase is sharper for the second natural frequency. As can be seen in Fig 3.10, the trend of the first two natural frequencies in the UPWIND project report also reveals similar results [66].

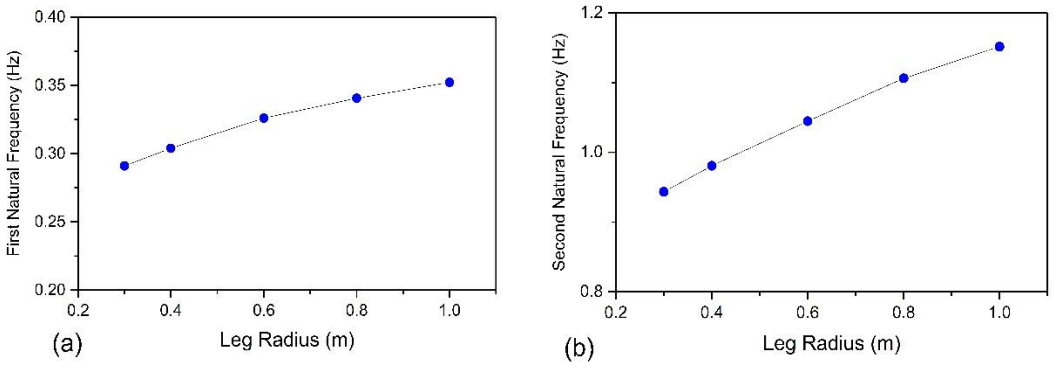

Figure 3.9 Natural frequency vs leg radius a) first natural frequency b) second natural frequency

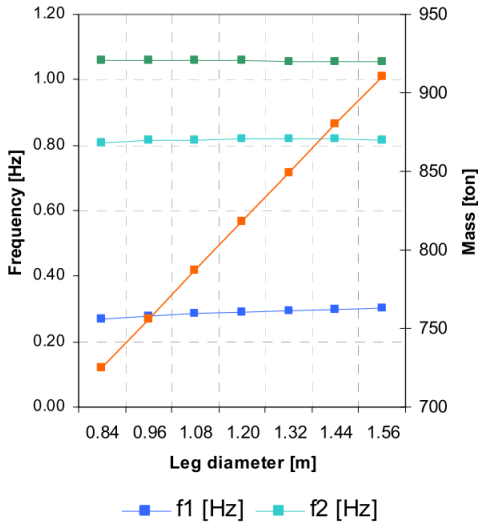

Figure 3.10 First and second natural frequency vs leg diameter [66]

Similarly, a parametric study on the effect of brace configurations has been performed and shown in Fig. 3.11. The first natural frequency of the offshore wind turbine slightly increases with the increasing brace thickness from 10mm to 35mm. Again, this increase is more pronounced for the second natural frequency in which there is a maximum of 5% increase in the second natural frequency.

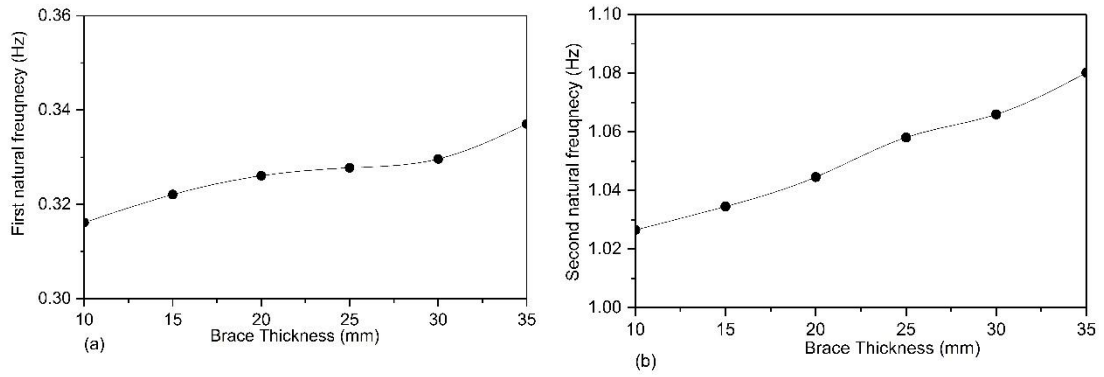

Figure 3.11 Natural frequency vs brace thickness a) first natural frequency b) second natural frequency

The parametric study of the effect of brace radius on the natural frequencies of the system is depicted in Fig. 3.12 The figure shows a slight increase in the first natural frequency. However, a sharper increase in the second natural frequency is seen in Fig. 3.12b.

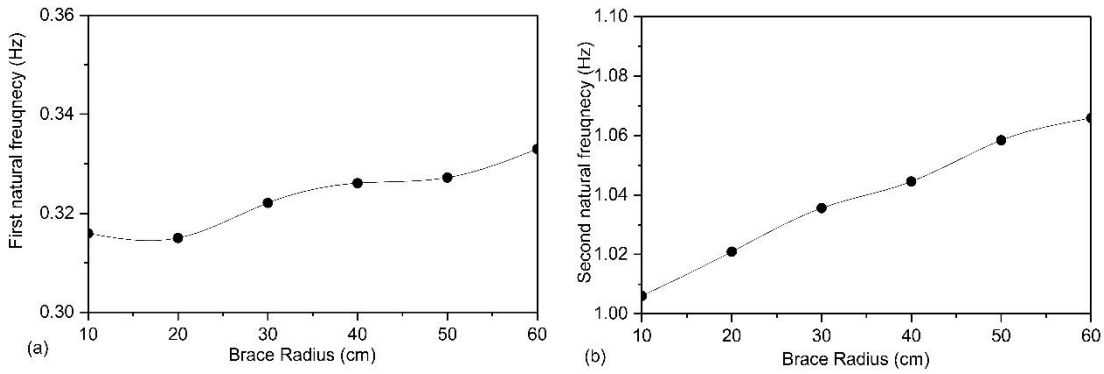

Figure 3.12 Natural frequency vs brace radius a) first natural frequency b) second natural frequency

Since monopiles are becoming less suitable in deeper water depth due to the decrease in natural frequency as well as high hydrodynamic loading on the large diameter of monopile, jacket foundations become more applicable for these water depths. As the jacket height is variable as a function of water depth, it is vital to investigate the effect of jacket height on the first natural frequencies of the system. In this section, the effect

of jacket height on the mode shapes and natural frequencies are investigated. Fig. 3.13a and Fig. 3.13b shows the first and second natural frequencies as a function of jacket height. It can be seen that the two frequencies decrease with increasing jacket height. This trend is due to the decreasing stiffness of the jacket. This implies that the decreasing rate of the second frequency is smaller than that of the first frequency. Fig. 3.13c and Fig. 3.13d are the corresponding modal shapes as a function of jacket height. Arrows in the figures indicate the direction of jacket height increasing from 40 to 94 meters. Again, the first modes exhibit the largest end deflections whereas the second modes exhibit the inflection points whereby the curvatures change their sign. It is also seen how the higher jacket substructures possess larger slopes of modal shapes.

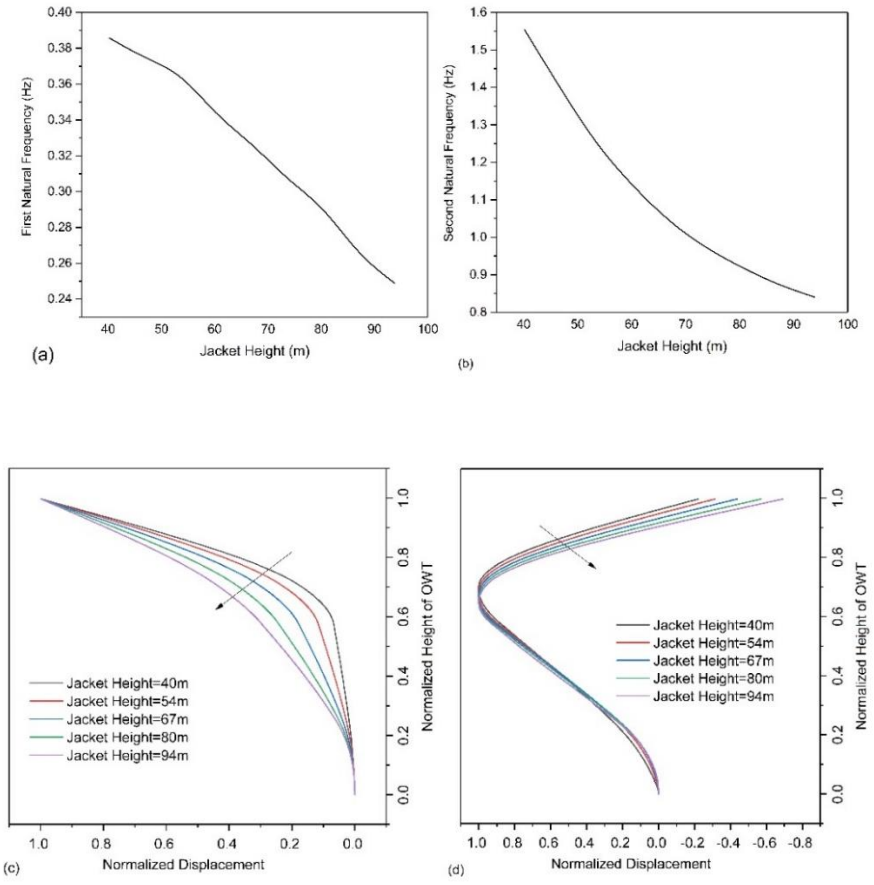

Figure 3.13 a) first natural frequency vs jacket height b) second natural frequency vs jacket height c) and d) the first two mode shapes for different jacket heights with arrows showing the trend of increasing jacket height

The effect of turbine tower height on the first two natural frequencies of wind turbine jacket is now investigated by the developed code. As seen from Fig. 3.14, the first two natural frequencies decrease with the increasing tower height. This is reasonable since the stiffness of the tower decreases when the height of the tower increases which results in the decreasing natural frequencies.

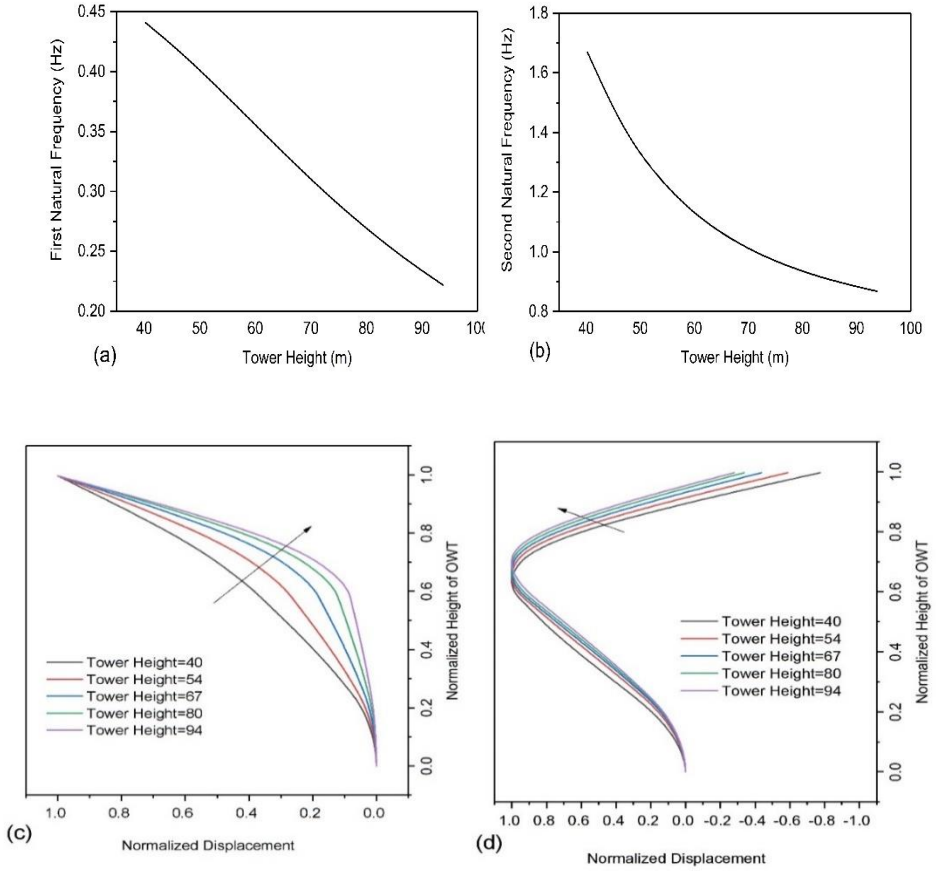

Figure 3.14 a) first natural frequency vs tower height b) second natural frequency vs tower height c) and d) the first two mode shapes for different tower heights with arrows showing the trend of increasing tower height

The footprint dimensions of the jacket foundations are the most important configuration parameters which are capable of securing wind turbines. In this study, the footprint of the jacket is assumed as a square between the four piles. By using the developed code, a parametric study to investigate the effect of footprint dimension on the natural frequencies of the system is performed. To do this, only footprint widths are changed

and other dimensions remain unchanged. Fig. 3.15a and Fig. 3.15b show the first two natural frequencies of offshore wind turbine as a function of footprint width. It can be seen that the aforementioned frequencies increase with an increase in the footprint substantially. This is consistent with the results of the UpWind project report shown in Fig 3.16 [66]. Fig 3.15c and Fig 3.15d are the corresponding mode shapes as a function of footprint width. The arrow in the plots indicates the direction of increase in the footprint width from 7.2m to 16.8m. The first mode shows the largest deflections near the top tower region whereas the second mode exhibits the inflection points whereby the curvatures change their signs. In the meanwhile, one can observe the larger slopes of modal shapes for the wider jacket footprints. First mode shapes in Fig 3.15d are seen to uniquely locate at the top of the tower. In Fig 3.15d, the second mode shapes are much more different than the first mode shapes, when varying footprint widths.

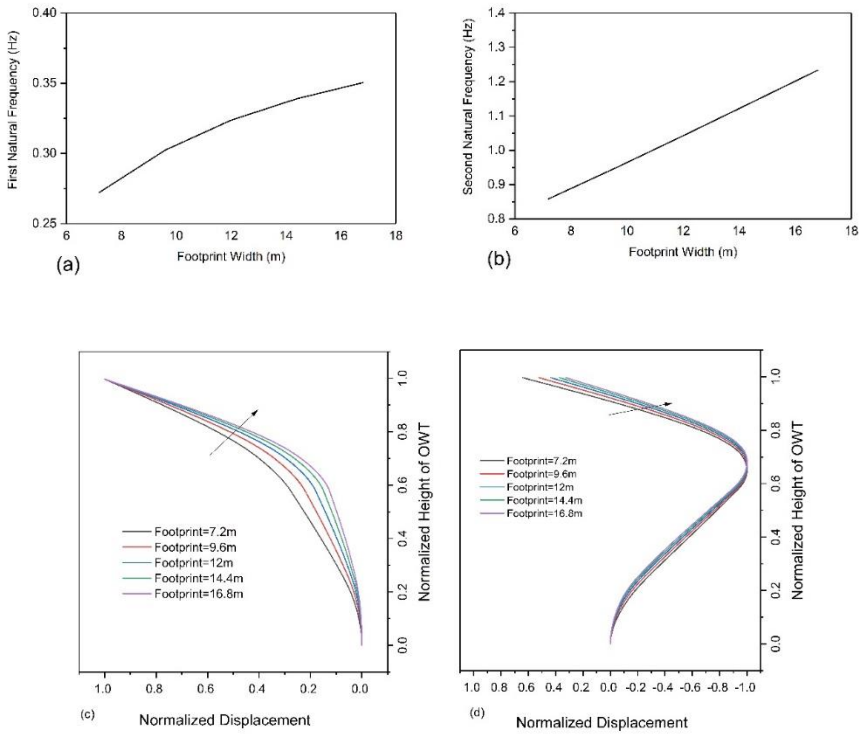

Figure 3.15 (a) 1st and (b) 2nd natural frequencies for OWT jacket as a function of footprint width (c) and (d) are the first two mode shapes for different footprints with arrows showing the trend of increasing footprint width

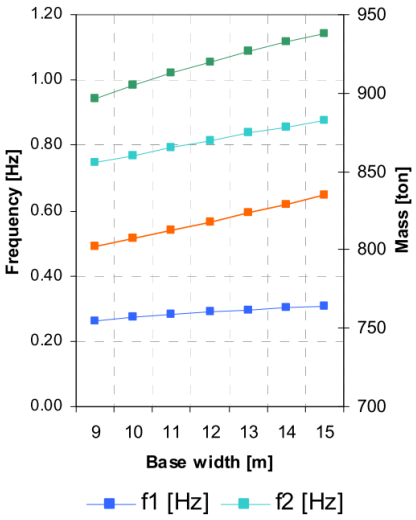

Figure 3.16 First and second natural frequencies vs base width [66]

The effects of turbine parameters such as RNA mass and transition piece mass on the first and second natural frequencies of the system are investigated and depicted in Fig 3.17. In these figures, the RNA mass (sum of mass of rotors, nacelle and hub) is varied +/-33% with respect to the reference value of 450 tons. The transition piece mass is also varied between 400 tons and 900 tons. As can be seen in Fig 3.17a, it is clear that RNA mass affects the first natural frequency heavily, while the first natural frequency is slightly affected by the change in the transition piece mass. In Fig 3.17b, the second natural frequency is highly dependent on the transition piece mass, whereas it is affected by the RNA mass to a small degree. This is due to the fact that RNA is located at the top of the tower where the deflection is maximum in the first mode shape and the transition piece is located close to the curvature point of the second mode shape. Therefore, the RNA mass and the transition piece mass are important parameters in the first and second natural mode shapes, respectively.

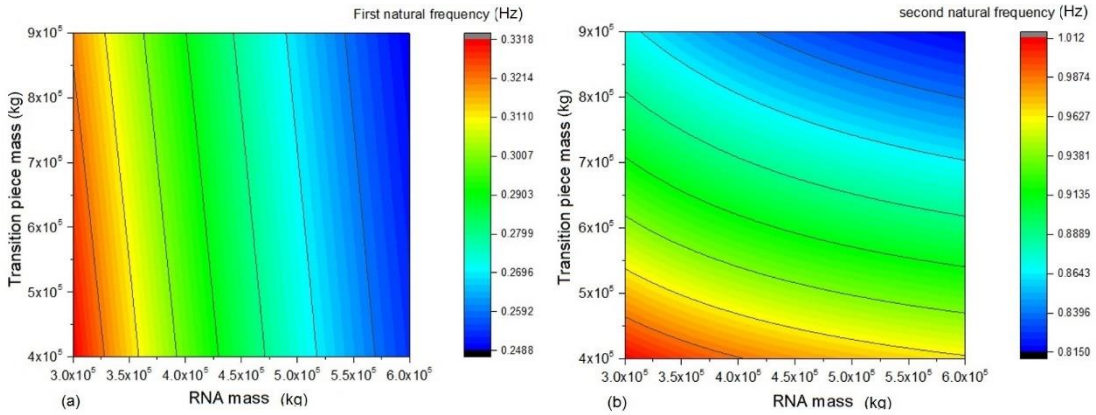

Figure 3.17 (a) 1st and (b) 2nd natural frequencies for OWT jacket as a function of transition piece mass and RNA mass

The variation of the natural frequency for various soil conditions is examined and plotted in Fig 3.18. The soil profile is assumed as sand and soil condition is varied by the angle of internal friction ϕ (detailed soil pile interaction model will be discussed in section 3.3). The friction angle is varied between 32 and 45 degrees and other soil parameters such as submerged unit weight are kept constant. First natural frequency increases from 0.295 Hz to 0.305 Hz when the internal friction angle changes from 32 to 45 degrees, with only a 3% increase. This means that the first natural frequency of the jacket OWT is slightly affected by the soil stiffness. Therefore, this type of foundations may be suitable for soil conditions with low mechanical properties.

Second natural frequency increases from 1.01 Hz to 1.08 Hz by increasing the internal friction angle; 7% increase in the second natural frequency. Therefore, one can conclude that the second natural frequency of jacket OWTs is more sensitive to the soil conditions.

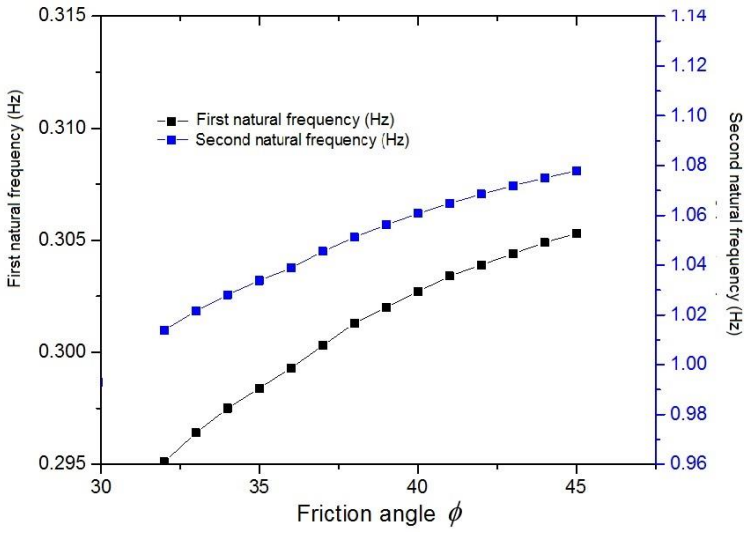

Figure 3.18 First and second natural frequencies for OWT jacket as a function of friction angle of soil

3.2.3.2 Nonlinear Dynamic analysis

Due to nonlinearities involved in the model (non-linear soil pile interaction and some nonlinear terms in the equation of motion of vibration control devices which will be discussed in the next chapters), the well-known Newmark's method [67] for solving nonlinear systems has been used. In 1959, Newmark developed a time-stepping method to solve linear structural dynamic vibrations. Later on, Newmark extended the method for nonlinear systems [67]. The nonlinear Newmark's solution is the most popular for performing earthquake analysis as well as nonlinear structural dynamic vibrations. The summary of the time-stepping solution of Newmark's method is explained in Appendix B.

Newmark's solution is used in solving the dynamic vibration of the OWT jacket developed using lumped mass modelling and the dynamic responses are compared with the dynamic responses obtained from SESAM software package. Time history of a stochastic loading is applied at the top of the tower and the dynamic deflection at the top of the tower generated in the developed code as well as SESAM software package is recorded and compared in Fig 3.19. The results are acceptable since they use different

theoretical methods and stiffness matrices and consequently the damping matrices slightly differ.

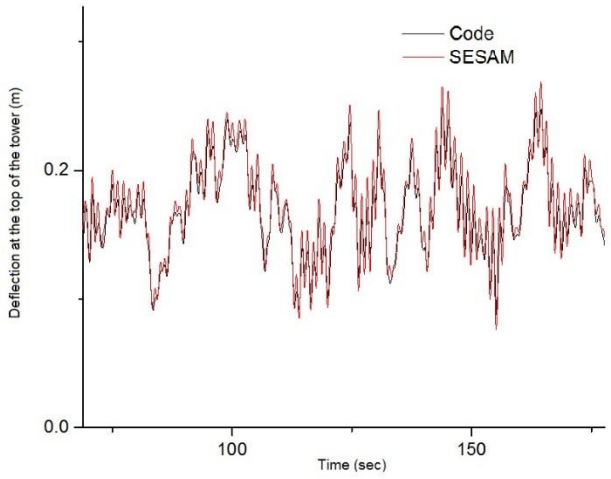

Figure 3.19 Time history of the deflection at the top of the tower for OWT jacket in the developed code and SESAM software

3.3 Monopile modelling (Timoshenko model)

To model OWT monopiles, Timoshenko beam element for the uniform section is utilized. The uniform Timoshenko element is the modified version of the Euler-Bernoulli element in which the shear deformation is introduced.

The generic two-mode element stiffness and mass matrices are used as following [68].

$$K = \begin{bmatrix} K_1 & K_2 \\ K_2 & K_3 \end{bmatrix} \tag{3.8}$$

$$M = \begin{bmatrix} M_1 & M_2 \\ M_2 & M_3 \end{bmatrix} \tag{3.9}$$

$$[K_1]=\begin{bmatrix} \frac{12EJ_y}{L_e^3(1+K_{sy})} & 0 & 0 & 0 & \frac{6EJ_y}{L_e^2(1+K_{sy})} & 0 \\ 0 & \frac{12EJ_x}{L_e^3(1+K_{sx})} & 0 & \frac{-6EJ_x}{L_e^2(1+K_{sx})} & 0 & 0 \\ 0 & 0 & \frac{EA_z}{L_e} & 0 & 0 & 0 \\ 0 & \frac{-6EJ_x}{L_e^2(1+K_{sx})} & 0 & \frac{(4+K_{sx})EJ_x}{L_e(1+K_{sx})} & 0 & 0 \\ \frac{6EJ_y}{L_e^2(1+K_{sy})} & 0 & 0 & 0 & \frac{(4+K_{sy})EJ_y}{L_e(1+K_{sy})} & 0 \\ 0 & 0 & 0 & 0 & 0 & \frac{GJ_z}{L_e} \end{bmatrix} \tag{3.10}$$

$$[K_2]=\begin{bmatrix} \frac{-12EJ_y}{L_e^3(1+K_{sy})} & 0 & 0 & 0 & \frac{6EJ_y}{L_e^2(1+K_{sy})} & 0 \\ 0 & \frac{-12EJ_x}{L_e^3(1+K_{sx})} & 0 & \frac{-6EJ_x}{L_e^2(1+K_{sx})} & 0 & 0 \\ 0 & 0 & -\frac{EA_z}{L_e} & 0 & 0 & 0 \\ 0 & \frac{6EJ_x}{L_e^2(1+K_{sx})} & 0 & \frac{(2-K_{sx})EJ_x}{L_e(1+K_{sx})} & 0 & 0 \\ \frac{-6EJ_y}{L_e^2(1+K_{sy})} & 0 & 0 & 0 & \frac{(2-K_{sy})EJ_y}{L_e(1+K_{sy})} & 0 \\ 0 & 0 & 0 & 0 & 0 & -\frac{GJ_z}{L_e} \end{bmatrix} \tag{3.11}$$

$$[K_3]=\begin{bmatrix} \frac{12EJ_y}{L_e^3(1+K_{sy})} & 0 & 0 & 0 & \frac{-6EJ_y}{L_e^2(1+K_{sy})} & 0 \\ 0 & \frac{12EJ_x}{L_e^3(1+K_{sx})} & 0 & \frac{6EJ_x}{L_e^2(1+K_{sx})} & 0 & 0 \\ 0 & 0 & \frac{EA_z}{L_e} & 0 & 0 & 0 \\ 0 & \frac{6EJ_x}{L_e^2(1+K_{sx})} & 0 & \frac{(4+K_{sx})EJ_x}{L_e(1+K_{sx})} & 0 & 0 \\ \frac{-6EJ_y}{L_e^2(1+K_{sy})} & 0 & 0 & 0 & \frac{(4+K_{sy})EJ_y}{L_e(1+K_{sy})} & 0 \\ 0 & 0 & 0 & 0 & 0 & \frac{GJ_z}{L_e} \end{bmatrix} \tag{3.12}$$

$$[M_1]=\rho\begin{bmatrix}
\frac{13A_zL_e}{35}+\frac{6J_y}{5L_e} & 0 & 0 & 0 & \frac{11A_zL_e^3}{210}+\frac{J_y}{10} & 0\\
0 & \frac{13A_zL_e}{35}+\frac{6J_x}{5L_e} & 0 & -\frac{11A_zL_e^2}{210}-\frac{J_x}{10} & 0 & 0\\
0 & 0 & \frac{A_zL_e}{3} & 0 & 0 & 0\\
0 & -\frac{11A_zL_e^2}{210}-\frac{J_x}{10} & 0 & \frac{A_zL_e^3}{105}+\frac{2L_eJ_x}{15} & 0 & 0\\
\frac{11A_zL_e^3}{210}+\frac{J_y}{10} & 0 & 0 & 0 & \frac{A_zL_e^3}{105}+\frac{2L_eJ_y}{15} & 0\\
0 & 0 & 0 & 0 & 0 & \frac{J_zL_e}{3}
\end{bmatrix} \tag{3.13}$$

$$[M_2]=\rho\begin{bmatrix}
\frac{9A_zL_e}{70}-\frac{6J_y}{5L_e} & 0 & 0 & 0 & -\frac{13A_zL_e^2}{420}+\frac{J_y}{10} & 0\\
0 & \frac{9A_zL_e}{70}-\frac{6J_x}{5L_e} & 0 & \frac{13A_zL_e^2}{420}-\frac{J_x}{10} & 0 & 0\\
0 & 0 & \frac{A_zL_e}{6} & 0 & 0 & 0\\
0 & \frac{13A_zL_e^2}{420}-\frac{J_x}{10} & 0 & -\frac{A_zL_e^3}{140}-\frac{L_eJ_x}{30} & 0 & 0\\
-\frac{13A_zL_e^2}{420}+\frac{J_y}{10} & 0 & 0 & 0 & -\frac{A_zL_e^3}{140}-\frac{L_eJ_y}{30} & 0\\
0 & 0 & 0 & 0 & 0 & \frac{J_zL_e}{6}
\end{bmatrix} \tag{3.14}$$

$$[M_3]=\rho\begin{bmatrix}
\frac{13A_zL_e}{35}+\frac{6J_y}{5L_e} & 0 & 0 & 0 & -\frac{11A_zL_e^2}{210}-\frac{J_y}{10} & 0\\
0 & \frac{13A_zL_e}{35}+\frac{6J_x}{5L_e} & 0 & \frac{11A_zL_e^2}{210}+\frac{J_x}{10} & 0 & 0\\
0 & 0 & \frac{A_zL_e}{3} & 0 & 0 & 0\\
0 & \frac{11A_zL_e^2}{210}+\frac{J_x}{10} & 0 & \frac{A_zL_e^3}{105}+\frac{2L_eJ_x}{15} & 0 & 0\\
-\frac{11A_zL_e^2}{210}-\frac{J_y}{10} & 0 & 0 & 0 & \frac{A_zL_e^3}{105}+\frac{2L_eJ_y}{15} & 0\\
0 & 0 & 0 & 0 & 0 & \frac{J_zL_e}{3}
\end{bmatrix} \tag{3.15}$$

in which J_x, J_y, and J_z are the area second moments of inertia; L_e is the original (undeformed) length of element from the start node to the end note; A_z is the cross section area of the element; G, E, and ρ are Shear Moduli, Young Moduli, and material density, respectively. In the aforementioned matrices, shear deformation is introduced by K_{sx} and K_{sy} as shear correction factors which are expressed as [68]:

$$K_{sx} = \frac{12EJ_y}{GA_{sx}L_e^2} \tag{3.16}$$

$$K_{sy} = \frac{12EJ_x}{GA_{sy}L_e^2} \tag{3.17}$$

in which shear areas along the principal axes are defined as:

$$A_{sx} = k_{ax}A_z \tag{3.18}$$

$$A_{sy} = k_{ay}A_z \tag{3.19}$$

For pipes with hollow circular cross sections, k_{ax} and k_{ay} are expressed as follows [69]:

$$k_{ax} = k_{ay} = \frac{6(1+\nu)^2\left(1+\left(\frac{D_i}{D_o}\right)^2\right)^2}{\left(1+\left(\frac{D_i}{D_o}\right)^2\right)^2(7+14\nu+8\nu^2)+4\left(\frac{D_i}{D_o}\right)^2(5+10\nu+4\nu^2)} \tag{3.20}$$

The baseline monopile foundation developed in the second phase of Offshore Code Comparison (OC3) project conducted by NREL is used in this study [70]. The total length of the monopile is 66 m, in which 10 m, 20 m, and 36 m are above the mean sea level, in the water and under the seabed, respectively. The general configuration of the turbine is shown in Fig 3.20. The total offshore wind turbine system is modeled by three-dimensional Timoshenko beam theory. The material properties of monopile is given in Table 3.4.

Table 3.4 Material properties of monopile

Component	Density (kg/m^3)	Young's modulus (GPa)	Poisson's ratio
Tower	8500	210	0.3
Monopile	7850	210	0.3

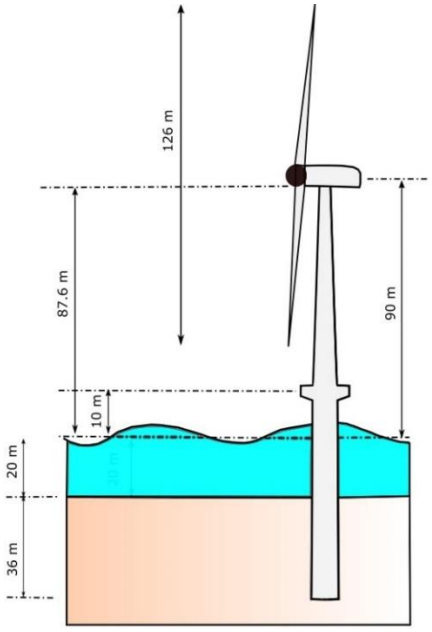

Figure 3.20 Schematic configuration of the offshore wind turbine monopile

3.3.1 Verification study

3.3.1.1 Natural frequency analysis

In this section, the developed model in MATLAB is verified by performing natural frequency analysis. To perform the natural frequency analysis, the stiffness of nonlinear soil pile interaction is linearized by obtaining initial stiffness of the *p-y* curves [71]. The resulting first and second natural frequencies are listed in Table 3.5 and compared with the results of the model constructed by commercial finite element software ANSYS and the results from the literature [51]. There is a good agreement between the results of natural frequency analyses.

Table 3.5 Frequency analysis results

Mode	Code	ANSYS	Dong Hywan Kim et al [51]
1st Fore-aft	0.235	0.234	0.234
1st Side-to-side	0.235	0.234	0.233
2st Fore-aft	1.426	1.426	1.406
2st Side-to-side	1.426	1.426	1.515

3.3.1.2 Dynamic analysis

Next, the results of the dynamic analysis for the offshore wind turbine subjected to Kobe ground motion are compared with the results obtained from the dynamic analysis performed in ANSYS. Fig 3.21a shows the non-scaled time history of acceleration of Kobe earthquake starting from the instant of 100 s. Fig 3.21b shows the time history of the top tower displacement simulated with the code written in MATLAB and the corresponding results obtained from ANSYS. The good agreement between two responses verifies the dynamic analysis solution used in the code.

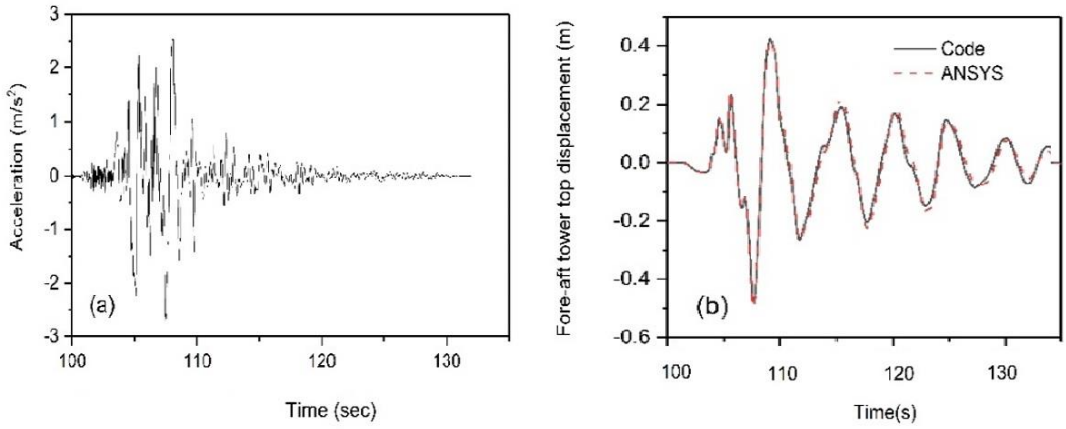

Figure 3.21 (a) Time history of acceleration of seismic excitation (Kobe) (b) time history of fore-aft tower top displacement simulated with ANSYS and the developed code under Kobe earthquake

3.3.2 Parametric study

In this section, a parametric study on the effect of dimensions, soil stiffness and water depth on the first and second natural frequencies of OWT monopile is given. First the effect of the embedded depth and the pile diameter on the first and second natural frequencies is shown in Fig 3.22. The embedded depth varies between 10 m and 36 m, and the pile diameter varies between 4 m and 8 m. Looking into the first natural frequencies in Fig 3.22a, it can be seen that the first natural frequency remains constant

after a specific embedded depth and this specific embedded depth is different for various pile diameters. For small pile diameters where the behaviour of the pile is more flexible, the aforementioned embedded depth is smaller. This is due to the fact that for example for the pile diameter of 4m, the natural frequency remains nearly constant (0.16 Hz) after 15m water depth. This means the natural frequency does not change for the embedded depth beyond 15m. For larger pile diameters which show more rigid behaviour, the first natural frequency remains constant after larger embedded depths. For example, for the pile diameter of 8 m, the first natural frequency remains constant for the embedded depths beyond 22 m. Fig 3.22b shows the second natural frequencies for different pile diameters and embedded depths. It is interesting that second natural frequencies show a different trend. In smaller embedded depths (smaller than 15m), the second natural frequency of the system is higher for small pile diameters, however for larger embedded depths, the natural frequency becomes higher when the pile diameter increases. This is due to the fact that when the pile diameter increases, the stiffness of the system increases due to the larger section area. However, the added mass of water inside the pile also increases in larger pile diameters and it reduces the second natural frequency considerably as the second natural frequency is highly dependent on the added mass of water. The reason that in smaller embedded depths the second natural frequency becomes smaller with an increase in pile diameter is that the effect of added mass in the natural frequency analysis becomes more dominating compared to the effect of increases in section area.

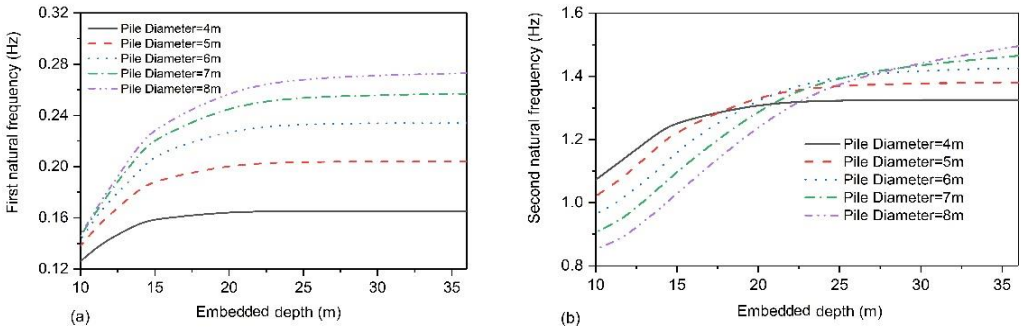

Figure 3.22 Natural frequency vs embedded depth of OWT monopile for different pile diameters a) first natural frequency b) second natural frequency

Fig 3.23 shows the first and second natural frequencies for different pile thickness and pile diameters. The first and second natural frequencies show some quadratic relations with pile thickness. However, this quadratic relation is more pronounced in the second natural frequency as shown in Fig 3.23b.

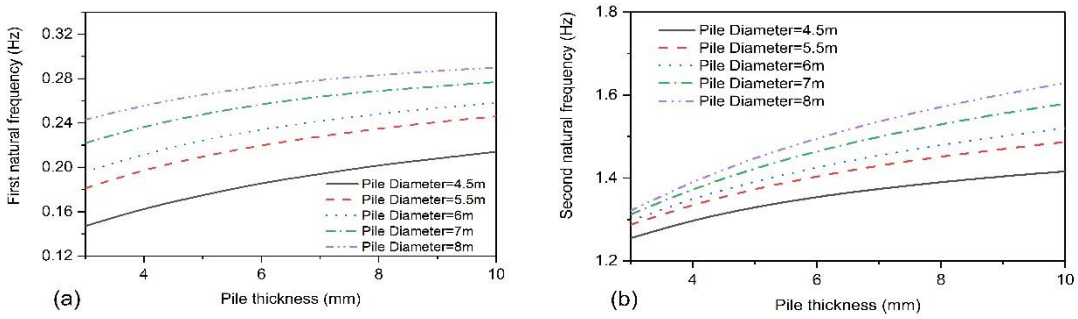

Figure 3.23 Natural frequency versus pile thickness of OWT monopiles for different pile diameters a) first natural frequency b) second natural frequency

Fig 3.24 shows the effect of water depth and angle of internal friction of soil on the natural frequencies of the system. Looking into the effect of water depth on the natural frequencies as shown in Fig 3.24a, it can be seen that the water depth has insignificant effect on the first natural frequency of the system. However, the effect of water depth on the second natural frequency is significant as the added mass of the water is located in lower elevations where there is higher deflection in the second mode. Fig 3.24b shows the natural frequencies as a function of angle of internal friction of soil. The angle of internal friction of soil is a measure of stiffness in sandy soil and will be explained in the next section. In Fig 3.24b, the angle of internal friction of soil is varied between 25 and 42 degrees and as expected, both natural frequencies increase when the angle of internal friction of soil increases, however second natural frequency shows larger variations. The first natural frequency increased from 0.22 Hz to 0.24 Hz, a 9% increase. However, the second natural frequency increased from 1.35 Hz to 1.75 Hz, with 30% increase. This highlights the highly dependency of the second natural frequency to the soil parameters.

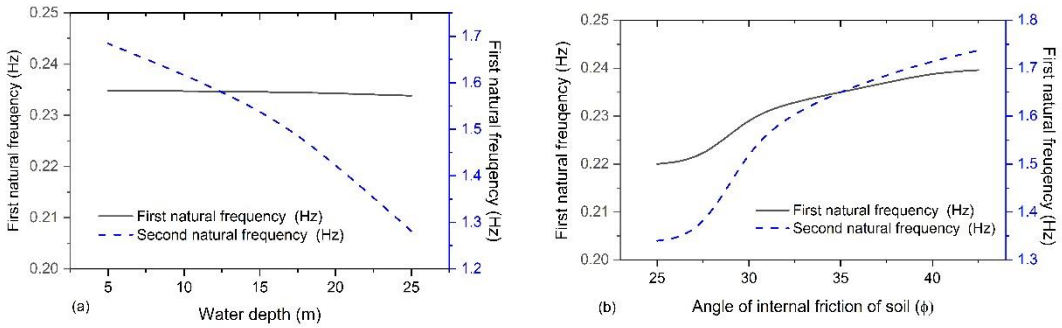

Figure 3.24 Natural frequencies of OWT monopile vs a) water depth b) angle of internal friction of soil

3.4 Soil-Pile Interaction Modeling

To model the soil-pile interaction of piles embedded in soil, the Winkler model approach using soil resistance-deflection *p-y* curves is often used [56]. These *p-y* curves represent the non-linear relation between soil resistance acting against pile, *p*, and lateral deflection of pile, *y*. The *p-y* curves recommended in design regulations such as the American Petroleum Institute API [57] and Det Norske Veritas DNV [72] are used in industry. These *p-y* curves are proposed by Reese et al. [73] and O'Neill and Murchison [74]. However, alternative approaches such as the finite element/difference method, model tests and strain-wedge method are also used. The main drawback of using these *p-y* curves is that they are derived on the basis of the Mustang Island tests for pile diameters around 2 m with length to diameter *L/D* ratio of 34. However, pile diameters in monopile for offshore wind are usually between 4 and 6 m or larger in XL monopiles and therefore *L/D* of OWT monopiles is around 5 which is well below that of the proposed *p-y* curves. This low length-diameter ratio changes the behaviour of piles from flexible to stiff as shown in Fig. 30. Dobry et al. [75], Budhu et al. [76] and Poulus et al. [77] proposed some criteria for flexibility of piles in a way that piles are either stiff or flexible. Based on Poulus et al. [77], a pile is flexible when the following relation is met

$$L > 4.44\left(\frac{E_p I_p}{E_s}\right)^{0.25} \tag{3.21}$$

L is the embedded length of pile, E_p is Young's modulus of elasticity of pile, I_P is the second moment of inertia of the pile, and E_s is Young's modulus of elasticity of soil.

However, criteria for rigid piles is as below:

$$L < 1.48\left(\frac{E_p I_p}{E_s}\right)^{0.25} \tag{3.22}$$

Given the diameter of 6.2 m, the embedded length of 24 m, and wall thickness varying between 4 to 8 cm for UpWind baseline monopile, the pile behaves flexibly if $E_s > 520$ MPa. This equation is unlikely to be met as the hardest sand profiles have Young's modulus of elasticity below 100 MPa. Therefore, the mentioned foundation that is studied in this paper and most old and new monopiles for OWT's behave as rigid piles. Thus, modelling stiffness of soil using *p-y* curves developed for rigid piles is essential in order to estimate the natural frequency and damping of the system accurately.

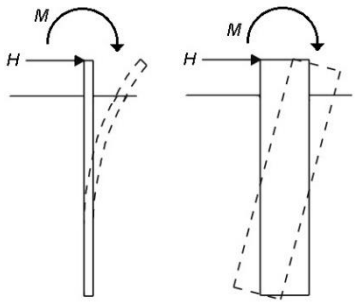

Figure 3.25 Flexible (Slender) pile versus rigid (Non-slender) pile

3.4.1 Initial Stiffness of p-y Curves

The main parameter of soil-pile interaction is the initial stiffness of *p-y* curves as it is used in finding the natural frequency of the system. According to API and DNV, the initial module of subgrade and initial stiffness of *p-y* curves are independent of the diameter of pile [57, 72]. There have been studies on the effect of diameter on soil-pile interaction [78]. The most recent studies on diameter effect in initial stiffness of *p-y* curves for offshore wind have been carried out by Sørensen et al. 2010 [60], Sørensen 2012 [59] and Kallehave et al. 2012 [61]. The calculation of initial stiffness using these studies and API method are listed in the following.

3.4.1.1 API Approach

The approach recommended by API is based on Mustang Island project in which initial stiffness was dependent on the angle of internal friction and relative density [57]. In this method, the ultimate soil resistance is determined by the following equation.

$$P = Ap_u tanh\left[\frac{kH}{Ap_u} y\right] \tag{3.23}$$

where A is a constant and equal to 0.9 for cyclic loading. K is the initial modulus of subgrade reaction. H is depth and p_u is the ultimate lateral bearing capacity determined from the following equation using the dimensionless parameters, C_2, and C_3 [57].

$$p_u = min\begin{cases} p_{us} = (C_1 H + C_2 D)\gamma H \\ p_{ud} = C_3 D\gamma H \end{cases} \tag{3.24}$$

Soil layer properties are shown in Fig 3.26a. The nonlinear resistance-deflection curves constructed based on the aforementioned method for different soil layers are illustrated in Fig 3.26b.

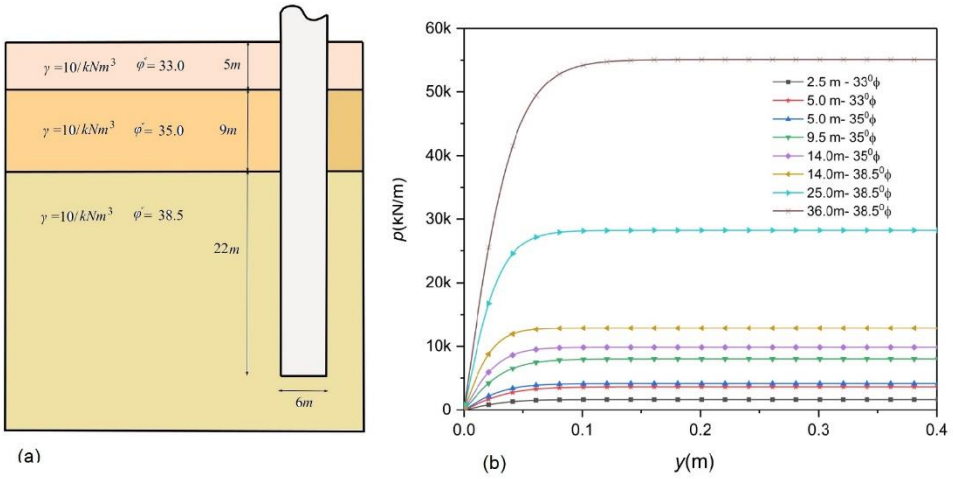

Figure 3.26 a) Soil layer properties b) nonlinear resistance-deflection curves

The *p-y* curve method presented in API RP 2GEO is developed for slender piles with diameters up to 2 m. Initial stiffness at $y = 0$ as proposed by API RP 2GEO:

$$E_{py}^{*} = \frac{dp}{dy}\Big|_{y=0} = Ap_u \frac{\frac{kx}{Ap_u}}{\cosh^2(\frac{kxy}{Ap_u})}\Big|_{y=0} = kx \tag{3.25}$$

In this formulation, initial stiffness of soil is only dependent on depth and initial modulus of subgrade reaction which is determined from the friction angle of soil, and there is no diameter effect in this formulation. However, the initial stiffness is a function of soil structure interaction that depends on the dimension, shape and material properties of soil and piles. Three most recent modified empirical relations proposed by some researches are used in this study as below.

3.4.1.2 Modification proposed by Sørensen et al. 2010

In 2010 Sørensen et al. [60] presented a modification of the initial stiffness of the pile-soil system for stiff piles of OWTs by introducing a power law relation for pile diameter and depth. This modification is based on a series of 3D FE analyses with Mohr-Coulomb failure criterion. The model has been calibrated based on a number of tests. In this formula, "*a*" is a constant value which is recommended as $a = 50\ MPa$. Three dimensionless constants are introduced as, $b = 0.6$, $c = 0.5$ and $d = 3.6$. x and

D are depth below mudline and the outer pile diameter respectively, with the reference values as $x_{ref} = 1.0m$ and $D_{ref} = 1.0\,m$. φ is the internal friction angle of soil in radian.

$$E^*_{py.Sor2010} = a.\left(\frac{x}{x_{ref}}\right)^b\left(\frac{D}{D_{ref}}\right)^c.\varphi^d \tag{3.26}$$

3.4.1.3 Modification proposed by Sørensen 2012

Later in 2012, Sørensen [59] modified the previous formulation by replacing the friction angle term to a term depending on the initial Young's modulus of the soil E_S . In this study, Sørensen concluded that E_S is a more appropriate parameter to account for soil structure interaction in the analysis. In the modified formula, $a = 1\,MPa$, $b = 0.3$, $c = 0.5$, $d = 0.8$, and $E_{S,ref} = 1\ MPa$.

$$E^*_{py.Sor2012} = a.\left(\frac{x}{x_{ref}}\right)^b\left(\frac{D}{D_{ref}}\right)^c.\left(\frac{E_s}{E_{S,ref}}\right)^d \tag{3.27}$$

3.4.1.4 Modification proposed by Kallehave et al. 2012

Kallehave [61] introduced a method for modelling large diameter piles of offshore wind by modifying the initial stiffness of the API formulation. The new formulation is based on theoretical analysis and benchmarking with full-scale operational measurements from Walney and Horns Rev wind farms. Here, the suggested initial stiffness depends on the initial stiffness calculated based on the offshore codes, k , with adding depth and diameter dimensionless parameters. The reference diameter is taken from the diameter of the pile used in the Mustang Island Field Test, $D_{ref} = 0.61m$. The dimensionless parameter for depth is $m = 0.6$. The reference depth is $x_{ref} = 2.5m$.

$$E^*_{py.Kallehave} = kx_{ref}.\left(\frac{x}{x_{ref}}\right)^m\left(\frac{D}{D_{ref}}\right)^{0.5} \tag{3.28}$$

3.4.2 Comparison of modified p-y curves

In this formulation, diameter effect is accounted by the square root of diameter ratio. Whereas, depth effect is accounted by the power terms ranging from 0.3 to 0.6. In order to compare these modifications, a comparison is made for three soil profiles (soft, medium, and hard) for two piles with 6.2 m diameter as of the baseline UpWind monopile [66] and a second pile with diameter of 9.0 m as the diameters of XL monopiles that are being designed. According to Figs. 3.27-28, there are greater differences in the values taken from four formulations in deeper depth. The Sorensen 2010 gives lower initial stiffness compared to API formulation. This is contradictory to the measurements of operational wind farms that suggest initial stiffness for small operational loading is greater than values recommended by API [79]. However, Sorensen 2012 [59] suggests higher initial stiffness for the top one-third of the pile, but again gives lower stiffness for the rest of the pile. The Kallehave formulation suggests mostly higher initial stiffness compared to API formulation, with more pronounced difference in XL monopiles.

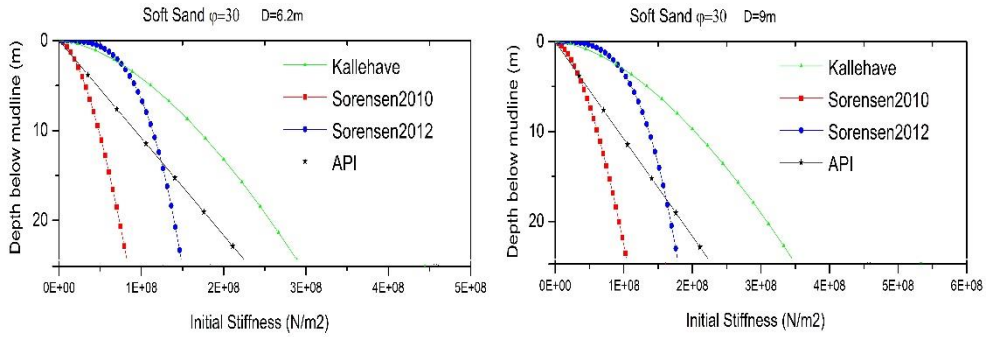

Figure 3.27 Comparison of initial stiffness for soft sand

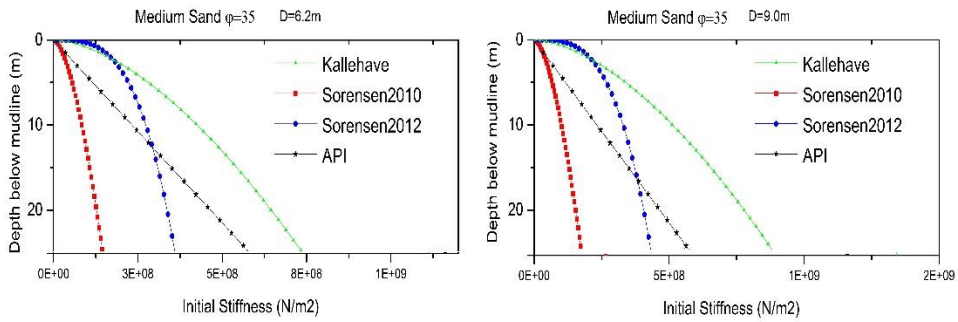

Figure 3.28 Comparison of initial stiffness for medium sand

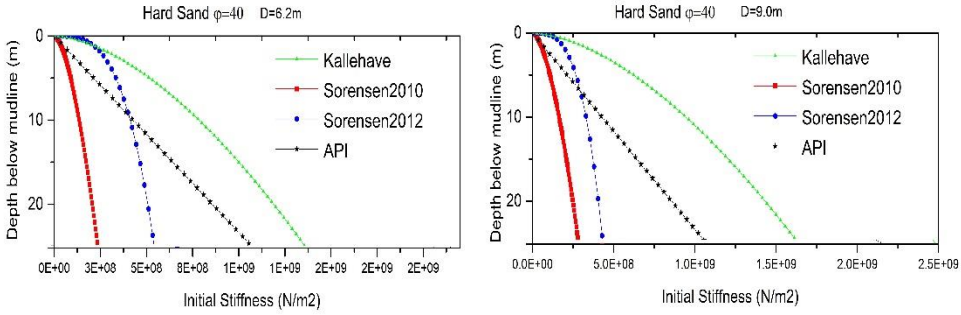

Figure 3.29 Comparison of initial stiffness for hard sand

Next, natural frequencies of the total system in three soil profiles are calculated and compared in Table 3.6 and 3.7. The first natural frequency according to Sorensen 2010 formula decreases by 1.5% for all soil profiles compared to that of API. However, the first natural frequency calculated from the two other formulae (Sorensen 2012 and Kallehave) are greater than that of API, by 1.4-2.5%. This is consistent with the results of the vibration experiments carried out for a number of wind farms that indicated higher natural frequency compared to design natural frequency [79].

The value of second natural frequency decreases similarly in Sorenson 2010 formulation. Whereas, it increases based on the other two formulations. It should be noted that the second natural frequency experiences more variations compared to the first natural frequency, with around two times the variation of first natural frequency.

Table 3.6 First natural frequencies

Soil Profile	API	Sorensen 2010	Sorensen 2012	Kallehave
Soft	0.277	0.273(-1.5%)	0.283(2.2%)	0.284(2.5%)
Medium	0.283	0.279(-1.4%)	0.288(1.8%)	0.288(1.8%)
Hard	0.286	0.282(-1.4%)	0.290(1.4%)	0.291(1.4%)

Table 3.7 Second natural frequencies

Soil Profile	API	Sorensen 2010	Sorensen 2012	Kallehave
Soft	1.246	1.207(-3.1%)	1.323(6.2%)	1.326(6.4%)
Medium	1.317	1.269(-3.6)	1.378(4.6%)	1.378(4.6%)
Hard	1.352	1.311(-3.1)	1.397(3.3%)	1.397(3.3%)

3.5. Loading Description

This section describes the formulation and properties of wind, wave, and seismic loadings applied to the model for the next sections.

3.5.1 Wind

The wind speed acting on the system can be represented by a constant mean wind load $\bar{v}$, and a turbulent wind component $\hat{v}(t), v(t) = \bar{v} + \hat{v}(t)$. The mean velocity $\bar{v}(z)$ is calculated using the logarithmic wind profile as:

$$\bar{v}(z) = V_{ref} \frac{\log(z / z_0)}{\log(H_{ref} / z_0)} \tag{3.29}$$

where V_{ref} is the mean velocity at the reference height $H_{ref} = 90m$, z is the vertical coordinate, and z_0 is the roughness length.

The Kaimal spectrum [80] is adopted in this study to calculate the turbulent wind velocity and can be expressed as

$$S_v(f) = \frac{4I^2 L_k}{(1+6fL_k/\bar{v})^{5/3}} \tag{3.30}$$

where I is the wind turbulence intensity, f is the frequency (Hz), and L_k is the integral scale parameter.

For continuous structures modeled as a multi degrees of freedom system, the power spectrum of fluctuating drag force is represented by the following [81]

$$S_{f,j}(f) = (C_D A_T \rho)^2 \sum_{k=1}^{N}\sum_{l=1}^{N} S_{v_k v_l}(f)\bar{v}_k \bar{v}_l \phi_j(k)\phi_j(l) \tag{3.31}$$

where C_D is the drag coefficient; A_T is the total surface area of the tower subjected to the wind, ρ is the air density, k and l are spatial nodes, $\bar{v}_k$ and $\bar{v}_l$ are the mean wind velocities at the mentioned nodes, $\phi_j(k)$ and $\phi_j(l)$ are the jth mode shape at the nodes, and $S_{v_k v_l}(f)$ is the cross power spectral density function of wind velocity between locations k and l which is defined as

$$S_{v_k v_l}(f) = Coh(k,l;f)\sqrt{S_{v_k v_k}(f) S_{v_l v_l}(f)} \tag{3.32}$$

in which $S_{v_k v_k}$ and $S_{v_l v_l}$ are the wind velocity auto spectra at points k and l, respectively, as defined by Eq. 30, and $Coh(k,l;f)$ is the spatial coherence function from IEC [47] which is expressed as:

$$Coh(k,l:f) = \exp\left(-a\sqrt{\left(\frac{fl}{\bar{v}_{hub}}\right)^2 + \left(\frac{0.12L}{L_c}\right)^2}\right) \tag{3.33}$$

in which a is the coherence decrement, L is the distance between points k and l on the grid, L_c is coherence scale parameter and $\bar{v}_{hub}$ is the mean wind speed at the hub. In the present study, the air density, the coherent decrement, the coherence scale parameters, the roughness length, and the drag coefficient are taken as 1200 kg/m^3, 12, 340.2 m,

0.005, and 1.2, respectively. In this study, a 3D wind velocity field with 961 points (31 $\times$ 31) which covers the rotors is generated based on Eqs. 3.31-33 using Turbsim code [82]. Next, the generated wind velocity field is used in NREL simulation tool [64] to simulate the time history of wind loading applied to the system. Finally, the generated wind loading time history is used in the developed code to consider aerodynamic loading.

3.5.2 Wave loading

Wave excitation on cylindrical structural members of fixed platforms can be calculated using the Morison equation [83]. The transverse sea wave force acting on a strip of a length dz of a monopile can be expressed as [84]

$$dF = \frac{\rho_w}{2} C_d D \upsilon |\upsilon| dz + \frac{\pi D^2}{2} C_m \rho_w \dot{\upsilon} dz \tag{3.34}$$

where C_d and C_m are the drag and inertia coefficients, respectively ($C_d = 1.2$ and $C_m = 2$ in the current study), D is the diameter of the member, $\dot{\upsilon}$ and υ are horizontal acceleration and velocity of fluid particles induced by wave excitations, and ρ_w is water density (1025 kg/m^3).

To generate wave time histories, the spectrum developed through Joint North Sea Wave Observation Project (JONSWAP) project is used [85].

$$S_{\eta\eta}(f) = \frac{\alpha g^2}{f^5} \exp\left[-\frac{5}{4} \left(\frac{f_m}{f}\right)^4 \right] \gamma^{\exp\left[-\frac{(f-f_m)^2}{2\sigma^2 f_m^2} \right]} \tag{3.35}$$

in which η is the function of water surface elevation, γ is the peak enhancement factor (3.3 for the north sea), g is the acceleration of gravity, and f is the wave frequency (Hz). The constants in this equation can be defined as

$$\alpha = 0.076 \left(U_{10}^{\ 2} / Fg \right)^{0.22} \tag{3.36}$$

$$f_m = 11 (v_{10} F / g^2)^{-1/3} / \pi \tag{3.37}$$

and

$$\sigma = \begin{cases} 0.07 & f \le f_m \\ 0.09 & f > f_m \end{cases} \tag{3.38}$$

where U_{10} is the mean wind velocity at 10 m from the sea surface, and F is the fetch length in which the wind blows without any change of direction.

Then total wave force acting on the structural members can be calculated as

$$F_f(t) = \int_0^d dF \phi_f(z) dz \tag{3.39}$$

where dF is the wave loading on the member mentioned in Eq. (33), and ϕ_f is the shape function of the offshore structure subjected to wave loading, d is the depth of the water surface, and z is the vertical direction.

3.5.3 Seismic Excitation

Time series of acceleration of strong ground motions recorded during past earthquake events are used to simulate seismic excitation. Two horizontal directions are selected to represent the behavior of earthquake events. In this study, sloshing of water surrounding the structure is ignored as it is believed to have insignificant effects. The seismic records are selected from PEER NGA Database [86] as it includes thousands of records with various mechanisms, soil types, intensities and durations. The details of the ground motion records used in this study are tabulated in Table 3.8. The magnitudes of the events range from 6.5 to 7.5. The seismic loading is assumed to start at the instant of 100 sec..

Table 3.8 Seismic records

ID	Earthquake	Magnitude	Year	Record Station	Soil Type
1	Kobe, Japan	6.9	1995	Kobe University	B
2	Northridge-01	6.69	1994	17645	D
3	Northridge-Landers	7.28	1992	17645 Saticoy St	D
4	Northbridge-Narrows01	5.99	1987	17645 Saticoy St	D
5	Tabas, Iran	7.35	1978	Tabas	C
6	Manjil, Iran	7.37	1990	Abbar	E

7	Manjil, Iran	7.37	1990	Abhar	D
8	Manjil, Iran	7.37	1990	Qazvin	C
9	Manjil, Iran	7.37	1990	Rudsar	D
10	Erzican, Turkey	6.69	1992	Erzincan	D
11	Loma Prieta	6.93	1989	Apeel10 - Skyline	D
12	Loma Prieta	6.93	1989	Apeel 2 - Redwood City	E
13	Cape Mendocino	7.01	1992	Cape Mendocino	B
14	Cape Mendocino	7.01	1992	Eureka - Myrtle & West	C
15	Cape Mendocino	7.01	1992	Fortuna - Fortuna Blvd	D
16	Cape Mendocino	7.01	1992	Petrolia	D
17	Cape Mendocino	7.01	1992	Shelter Cove Airport	D
18	Landers	7.28	1992	Amboy	C
19	Landers	7.28	1992	Baker Fire Station	D
20	Landers	7.28	1992	Bell Gardens - Jaboneria	D
21	Imperial Valley-06	6.53	1979	Aeropuerto Mexicali"	C
22	Imperial Valley-06	6.53	1979	Agrarias	D
24	Imperial Valley-06	6.53	1979	Bonds Corner	D
24	Imperial Valley-06	6.53	1979	Brawley Airport	C
25	Imperial Valley-06	6.53	1979	Calexico Fire Station	D
26	Imperial Valley-06	6.53	1979	Calipatria Fire Station	D
27	Imperial Valley-06	6.53	1979	Cerro Prieto	D
28	Imperial Valley-06	6.53	1979	Chihuahua	D
29	Imperial Valley-06	6.53	1979	Coachella Canal #4	C
30	Imperial Valley-06	6.53	1979	Compuertas	C

3.6 Summary

The structural models for jacket and monopiles for offshore wind turbines are described in this section. To use a computationally robust model for jacket foundation, a lumped mass model is used and the verification study is given. There is a very good agreement between the results of the lumped mass model and the finite element model. A maximum error of 3% is experienced because of the simplified model of lumped mass. This error is attributed to the difference in modelling the jacket in which multi-member members are simplified with lumped mass modelling. This model can be used for conceptual design of offshore wind turbine jackets in order to find the optimum configuration based on the limit states imposed by the relevant standards. A detailed parametric study is performed to investigate the effect of the important configurations

and geotechnical parameters on the natural frequencies. The first natural frequency of the jacket OWT is slightly affected by the soil stiffness. Therefore, this type of foundations may be suitable for soil conditions with weak mechanical properties.

Similarly, a model for offshore wind turbine monopiles based on the Timoshenko beam element is developed and a verification study is performed. There is a very good agreement between the results of natural frequency analyses. Some parametric studies concerning the effect of main variables such as embedded pile depth, pile diameter, pile thickness, water depth, and soil stiffness on the natural frequencies of the system are performed.

Then, detailed soil pile interaction model considering diameter effects is presented. Finally, the definition of various loading such as wind, wave and seismic used in the next sections is described.

Chapter 4 Parametric Study of Structural Vibration Control

4.1 Introduction

Highly dynamic nature of the applied loads on flexible and lightly damped offshore wind turbine (OWT) foundations affects the lifetime and serviceability of the system. In this chapter, the excessive vibration responses of OWTs are minimized using tuned mass dampers (TMD) and tuned liquid column dampers (TLCD). Due to high efficiency of TLCDs and TMDs for certain loading conditions, a combined TLCD-TMD is also utilized to improve the overall performance in a wide range of loading conditions. First, a parametric study was performed that highlights the sensitivity of these structural control devices. The effect of the mentioned devices on fixed offshore wind turbine foundations for the benchmark 5MW NREL turbine in various loading patterns was investigated. Then, the model was subjected to stochastically generated wind loading in operational, parked, startup, and shutdown conditions. The results suggest that the standard deviation of the dynamic responses can be greatly reduced with all structural control devices. However, TMDs are more efficient in operational conditions, whereas TLCDs show better performances in parked conditions. This highlights the possibility and efficiency of a combined TLCD-TMD system in which the dynamic responses are minimized efficiently in a wider selection of loading conditions.

4.2 Motivation

Previous studies have almost exclusively focused on the application of tuned mass dampers or tuned liquid column dampers separately and no previous research has investigated using both devices simultaneously for offshore wind turbines and no previous research has compared the effectiveness of these devices for offshore wind applications. Due to turbulent nature of environmental loading, offshore wind turbines oscillate under a wide range of dynamic loadings. A combination system of TLCDs and TMDs is utilized in this research in order to suppress a wider range of loading

conditions. Moreover, previous studies were limited to study of structural control devices for offshore wind turbines in operational and parked conditions and other special loading conditions such as startup and shutdown conditions are rarely studied in the literature. To fill this gap, in this research not only operational and parked but also startup and shutdown conditions are assessed. This study focuses on the jacket foundations using multiple lumped mass model and the baseline 5MW NREL turbine is considered [62]. First, free decay vibration, monotonic, impulse and harmonic loadings are assessed. Then, a number of stochastically generated wind loadings in operational, parked, startup, and shutdown conditions at various wind speeds are considered to demonstrate the impact of the mentioned structural control devices. Finally, a parametric study is carried out to investigate the effects of various parameters on the performance of the structural control devices.

4.3 Numerical Model

4.3.1 Tuned Liquid Column Dampers

TLCDs are composed of a U-shaped tube that is partially filled with liquid and dissipate vibration energy using the oscillation of the liquid between two columns. This oscillation of the liquid enables the system to re-establish equilibrium and dampen out the vibration. Fig 4.1 shows a schematic configuration of a TLCD attached to the main structure.

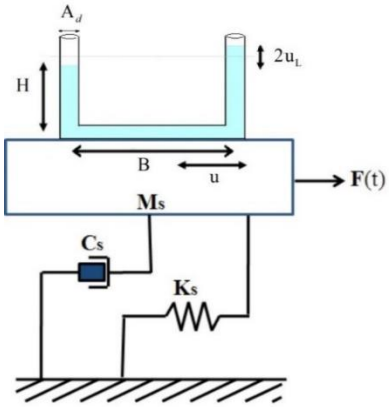

Figure 4.1 Schematic diagram of TLCD model

Two major assumptions are used in order to derive dynamic equations of TLCDs: (1) the liquid is incompressible and no pressure is created due to the oscillation of the liquid in the tube, (2) the sloshing of the liquid surface may be ignored as it is negligible compared to the sloshing of the whole body of water. The equation of motion of a U-shaped pipe attached to a structure for controlling vibration of the structure was developed by [27] and can be described as:

$$\rho A_d L_T \ddot{u}_L + \frac{1}{2}\rho A \xi |\dot{u}_L| \dot{u}_L + 2\rho A g u_L = -\rho A B \ddot{u} \tag{4.1}$$

where ρ is the density of the fluid, A_d is the cross-sectional area of the tube, B is the horizontal distance between two columns, g is the acceleration due to gravity, u_L is the change in the elevation of the liquid inside the columns and u is the horizontal deflection at the base of TLCD where it is attached to the OWT systems that can be located in nacelle, tower or transition piece. The overdot denotes differentiation with respect to time. ξ is the non-linear coefficient of head loss which is dependent on the opening ratio of the orifice ψ (ratio of the diameter of the orifice to the diameter of the horizontal tube). ξ can be calculated from the empirical formula developed from experimental results [87]:

$$\xi = (-0.6\psi + 2.1\psi^{0.1})^{1.6}(1-\psi)^{-2} \tag{4.2}$$

Eq. 4.1 can be rewritten by dividing by the mass of the liquid as

$$\ddot{u}_L + \frac{\xi}{2L}|\dot{u}_L|\dot{u}_L + \omega_L^2 u = -\alpha \ddot{u} \tag{4.3}$$

in which $L_T = B + 2H$ is the total length of the tube, $\alpha = B / L_T$ is the ratio of horizontal length to the total length, $\omega_L = \sqrt{2g / L_T}$ is the natural circular frequency of the TLCD.

The equation of motion of the main structure with n-degrees of freedom attached to the TLCD can be expressed as:

$$M_s\ddot{X} + C_s\dot{X} + K_sX = P(t) - \rho AB\ddot{u}_L R - \rho AL_T\ddot{u}R \tag{4.4}$$

in which $X = \{x_1, x_2, ..., x_n\}$ is the horizontal displacement vector of the main structure, $R = \{1, 0, ..., 0\}^T$ is a constant vector. K_s, M_s, and C_s are the n-dimensional stiffness, mass, and damping matrices of the main structure, respectively. $P(t)$ is n-dimensional vector of external force applied to the main structure.

Tuned liquid column dampers are tuned to the first natural frequency of the system by tuning ratio $\gamma = \omega_L / \omega_s$ which is controlled by the mass ratio $\mu = m_{TLCD} / m_s$. ω_L and ω_s are the frequency of the TLCD and natural frequency of the main structure, respectively. m_{TLCD} and m_s are the mass of TLCD and the mass of the main structure, respectively.

The equation of motion of the TLCD in conjunction with the main structure's equations is solved simultaneously in the nonlinear time domain using Newmark method [67] in order to consider the dynamic motion of the TLCD.

4.3.2 Tuned Mass Damper Systems

A tuned mass damper (TMD) is a device that consists of a spring, a damper, and a mass attached to a structure to control the dynamic vibration. The key aspect of a TMD is that its frequency needs to be tuned to a particular structural frequency so that it dampens out the vibration when that frequency is excited. The theory of multiple degrees of freedom (MDOF) systems using tuned mass dampers are illustrated and presented in the following section.

The governing equations for the MDOF system in Fig 4.2 are given as:

$$m_1\ddot{u}_1 + c_1\dot{u}_1 + k_1u - k_2(u_2 - u_1) - c_2(\dot{u}_2 - \dot{u}_1) = p_1 - m_1\ddot{u}_g$$

$$m_2\ddot{u}_2 + c_2(\dot{u}_2 - \dot{u}_1) + k_2(u_2 - u_1) - k_3(u_3 - u_2) - c_3(\dot{u}_3 - \dot{u}_2) = p_2 - m_2\ddot{u}_g$$

$$\vdots$$

$$m_d\ddot{u}_d + c_d\dot{u}_d + k_d u_d = -m_d(\ddot{u}_n + \ddot{u}_g) \tag{4.5}$$

where m_i, c_i, k_i, u_i, and p_i are mass, damping, stiffness, deflection, and point load for different degrees of freedom of main structure ($i = 1, 2, ..., n$), and m_d, c_d, k_d, and u_d are mass, damping, stiffness, and deflection for the TMD attached to the main structure.

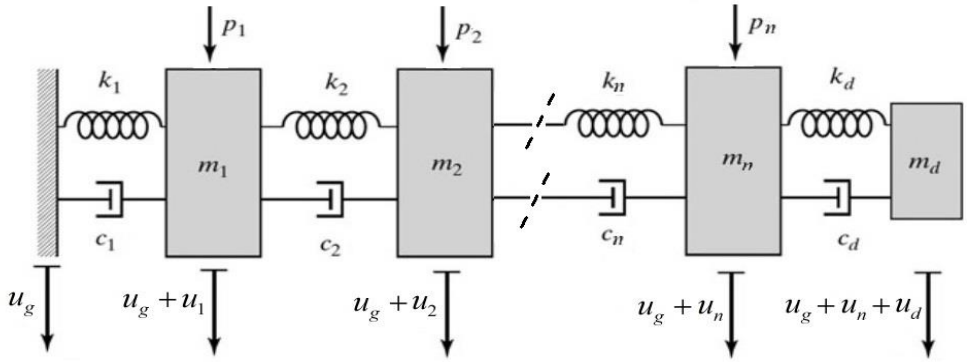

Figure 4.2 Multi degrees of freedom system equipped with a TMD

The integrated dynamic equations of offshore wind turbine can be expressed as:

$$\begin{bmatrix} M_s & \\ & m_d \end{bmatrix}\begin{bmatrix} \ddot{X}_s \\ \ddot{u}_d \end{bmatrix} + \begin{bmatrix} C_s & \\ & c_d \end{bmatrix}\begin{bmatrix} \dot{X}_s \\ \dot{u}_d \end{bmatrix} + \begin{bmatrix} K_s & \\ & k_d \end{bmatrix}\begin{bmatrix} X_s \\ u_d \end{bmatrix} = \begin{bmatrix} P(t) \\ -m_d\ddot{u}_n \end{bmatrix} - \rho AB\ddot{u}_L\begin{bmatrix} R \\ 0 \end{bmatrix} - \rho AL_T\ddot{u}\begin{bmatrix} R \\ 0 \end{bmatrix} \tag{4.6}$$

The schematic layout of integrated TLCD-TMD located in the nacelle is shown in Fig 4.3.

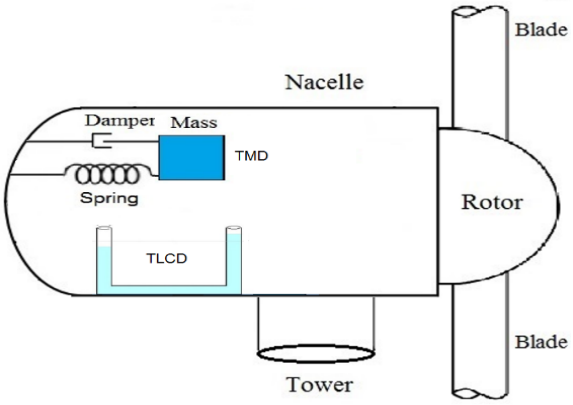

Figure 4.3 Schematic layout of TLCD-TMD in the nacelle

4.3.3 Turbine Model Description

In this study, NREL 5 MW wind turbine was considered as it is widely used as the turbine for benchmark studies [64]. This turbine is supported by baseline jacket foundation designed during the UpWind project [65]. The general configuration of the turbine is shown in Fig 3.2 and its particulars can be found in Table 3.2.

4.4 Numerical Results and Discussion

4.4.1 Basic Loading Functions

First, the complete offshore wind system equipped with TMD, TLCD and combined TLCD-TMD tuned to the first natural frequency of the system is subjected to an initial perturbation where the tower is displaced and allowed to oscillate freely. Three values of mass of the controller as 10 tons, 20 tons, and 40 tons are selected and the optimal parameters are obtained by tuning the structural control devices to the first natural frequency of the system. The TMD mass ratios corresponding to aforementioned masses are 1.1%, 2.2% and 4.4% respectively. The optimal tuning ratio is set as $\gamma = 1/(1+\mu)$. The parameters are tabulated in Table 4.1. For TLCDs, it is assumed that the type of the liquid is water. However, using liquids with higher density such as

glucose solution with a density of 1540 kg/m^3 results in 35% saving in the space required. The TMD and the TLCD are assumed to be installed in the nacelle and in the tower at the highest level, respectively.

Table 4.1 Optimal vibration controller parameters for the NREL 5 MW supported by a jacket

		TMD			*TLCD*				
Mass (kg)	*Mass ratio*	$k_d\,(N/m)$	$c_d\,(N/(m/s))$	$\omega_d\,(Hz)$	α	γ	μ	ξ	ψ
10,000	1.1%	41258	647	0.323	0.7	0.986	0.014	4.69	0.3
20,000	2.2%	80190	1275	0.319	0.7	0.972	0.029	4.69	0.3
40,000	4.4%	151915	2481	0.310	0.7	0.946	0.057	4.69	0.3

The time history of the deflection at the top of the tower shows how quickly the vibration is dampened out in Fig 4.4 As can be seen in this figure, increasing the mass of TMD and TLCD improves the damping capacity of the controller. Fig 4.4c compares the performance of a TMD, a TCD and a combined TLCD-TMD with a mass of 20 tons under free decay vibration. As the figure indicates combining two devices together (TLCD-TMD) can control the free decay vibration more effectively.

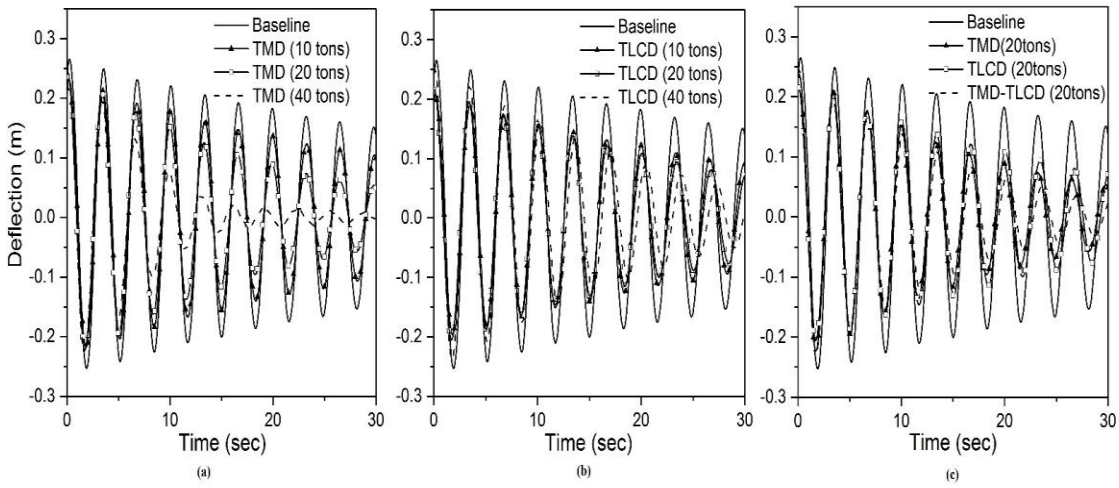

Figure 4.4 Free decay vibrations (a) TMD systems (b) TLCD systems (c) combined systems

Then, using logarithmic damping formula, the output damping ratio produced by damping devices is calculated by extracting the output damping of the uncontrolled system (baseline) from that of the controlled system according to the following formula;

$$\xi_{Damper} = \xi_{Controlled} - \xi_{Baseline} \tag{4.7}$$

Table 4.2 Output damping ratios produced from controller devices (%)

Mass (tons)	Mass ratio	TMD	TLCD	TLCD-TMD
10	1.1%	1.33	1.46	1.92
20	2.2%	2.54	2.21	4.43
40	4.4%	4.35	3.64	6.34

Table 4.2 tabulates the extra damping ratio produced when the controller devices are used. The output damping ratio for the combined device is much higher than the separate devices. For instance, the output damping ratio of TLCD-TMD with 20 tons is 43% higher than a TMD with a mass of 20 tons. Since free decay vibration oscillates under the natural frequency of the system which is not the case for operational cases, a study on the vibration control in the realistic operational case is more representative of the effectiveness of these systems and it is discussed in section 4.4. The time history of the deflections for three different loads (monotonic, impulsive and harmonic) and the effect of the controller devices on the deflection of the top of the tower is examined. The time to reach ultimate load in monotonic loading, the duration of the impulsive loading, and the period of the harmonic loading are shown as T_d (Fig 4.5) and were chosen as 1, 3.05 and 5 sec. The reason for choosing these values is to have the period of loading less, equal and larger than the natural period of the whole system. In order to show the efficiency of control devices, structural responses of the uncontrolled OWT are compared with the systems equipped with damping devices. In these cases, the mass of TMD, TLCD and combined TLCD-TMD was kept 20 tons and other parameters

were chosen in a way to tune to the natural frequency of the system according to Table 4.1.

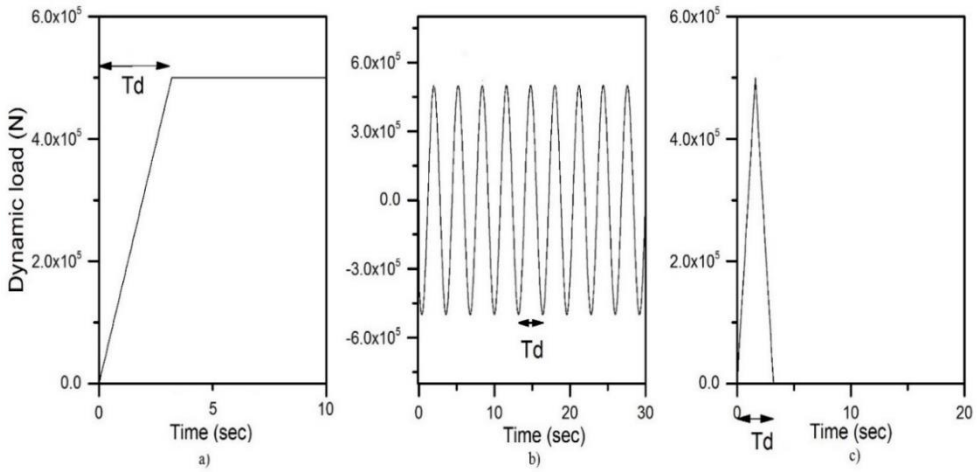

Figure 4.5 Loading functions in numerical examples (a) monotonic (b) harmonic (c) impulsive

The deflections for these loadings are shown in Fig 4.6 and 4.7. For monotonic loading, the results show that controller devices reduce amplitudes of deflection in the transition period and this reduction is more pronounced when the time to reach the ultimate load is smaller as this makes the loading more dynamic. This trend again can be seen for impulsive loading similar to monotonic loading.

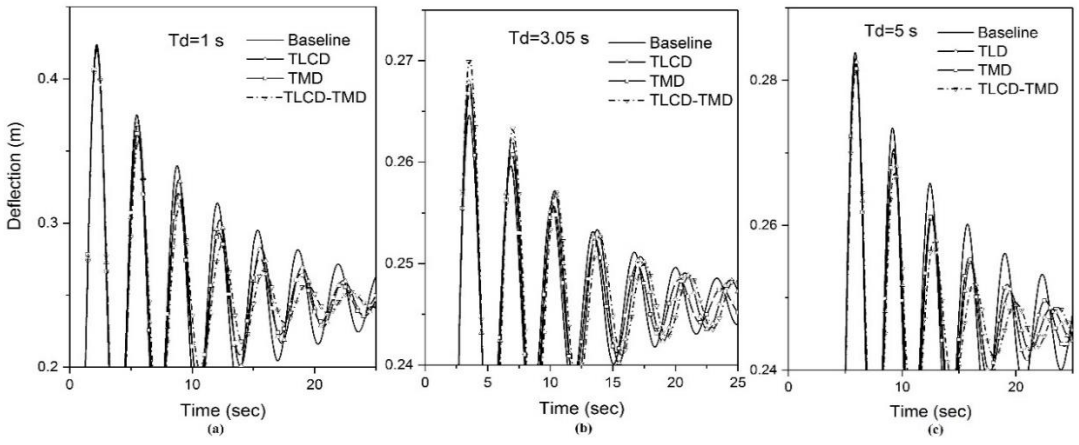

Figure 4.6 Structural responses under monotonic loading (a) T_d =1 sec **(**b) T_d =3.05 sec **(**c) T_d =5 sec

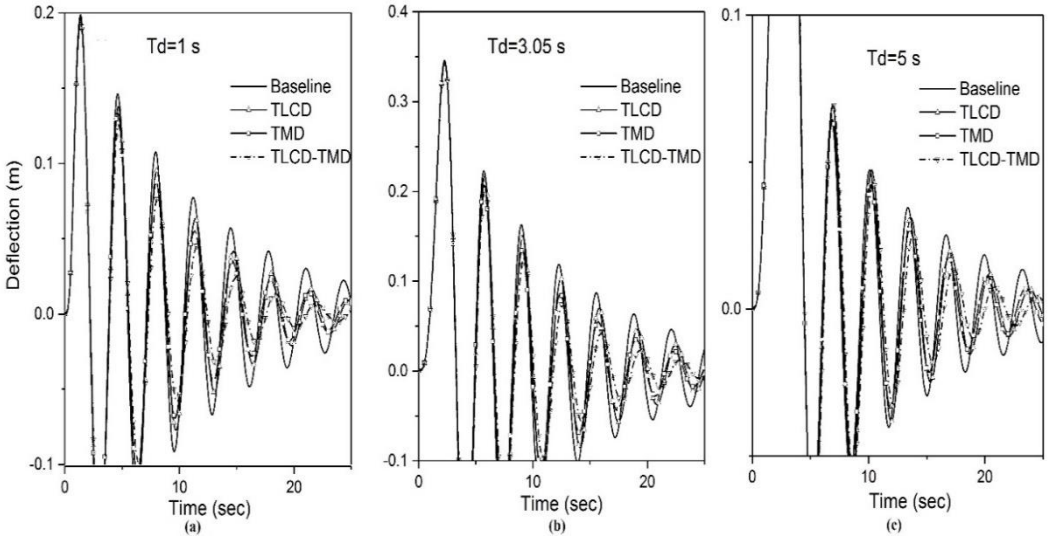

Figure 4.7 Structural responses under impulsive loading (a) T_d =1 sec **(**b) T_d =3.05 sec **(**c) T_d =5 sec

For harmonic loading, control devices reduce the amplitude of vibration considerably when the structure is excited with loading frequency equal to the natural frequency of the structure (Fig 4.8b) and this is more pronounced for combined TLCD-TMD, with 17% reduction in the amplitude of the vibration. However, when the period of harmonic loading is lower than natural period of OWT (Fig 4.8a), the control devices only have an impact in the transient period and it has negligible effects in the steady state of the time history. For harmonic loading with a larger period (Fig 4.8c), the amplitude of vibration even slightly increases due to increase in the mass of the whole system and subsequently decrease in natural frequency.

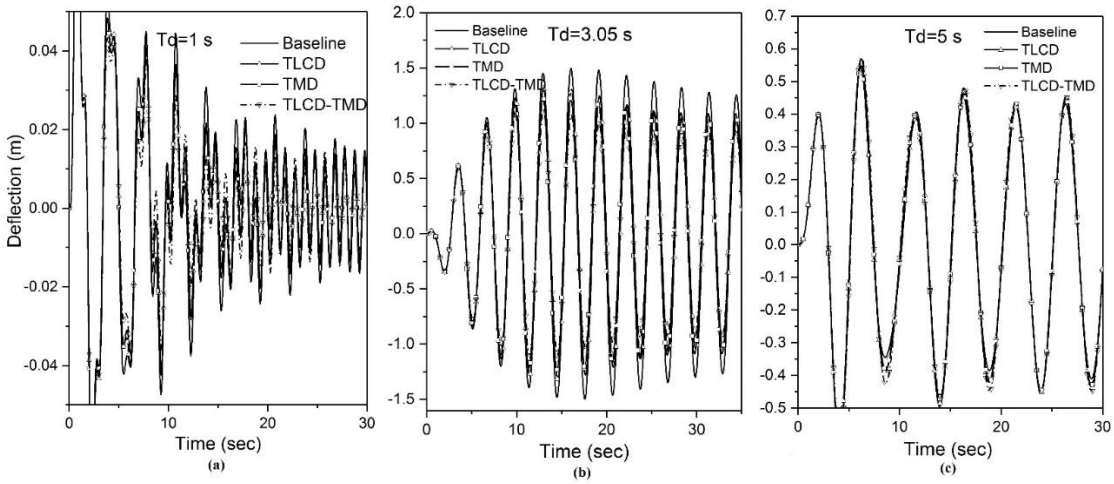

Figure 4.8 Structural responses under harmonic loading (a) T_d =1 sec **(**b) T_d =3.05 sec **(**c) T_d =5 sec

4.4.2 Parametric Study of TMD

In this section, harmonic forced vibration simulations were performed by a series of frequency loading with different TMD masses. The model was excited with $F = F_{st} \sin \omega t$, in which F_{st} is the static amplitude of the harmonic excitation and ω is the angular frequency of the excitation. The static amplitude F_{st} was kept constant and the excitation frequency swept in the range of 0.1 Hz to 1 Hz.

In order to scrutinize the responses relative to the baseline model without TMD, the results of models with TMD are normalized by the results without TMD and relative change in responses is demonstrated in Fig 4.9. It shows that there is a maximum of 35% decrease in the amplitudes for the TMD with a mass of 10 tons when the structure is excited with loading frequency equal to the natural frequency of the whole system. This relative change increases with higher TMD masses, with 80% decrease for a TMD with 40 tons mass. Also, the sharp peak of the curves slightly shifts to lower frequencies with increase in mass of TMD as it leads to a decrease in the natural frequency of the system. Beyond the suppression band, the TMD with 10 tons has a slight negative effect. However, heavier TMDs can increase the vibration responses up to 60% if

loading frequency is out of the suppression band. Therefore, this highlights the importance of correct tuning of TMDs especially for heavier TMDs.

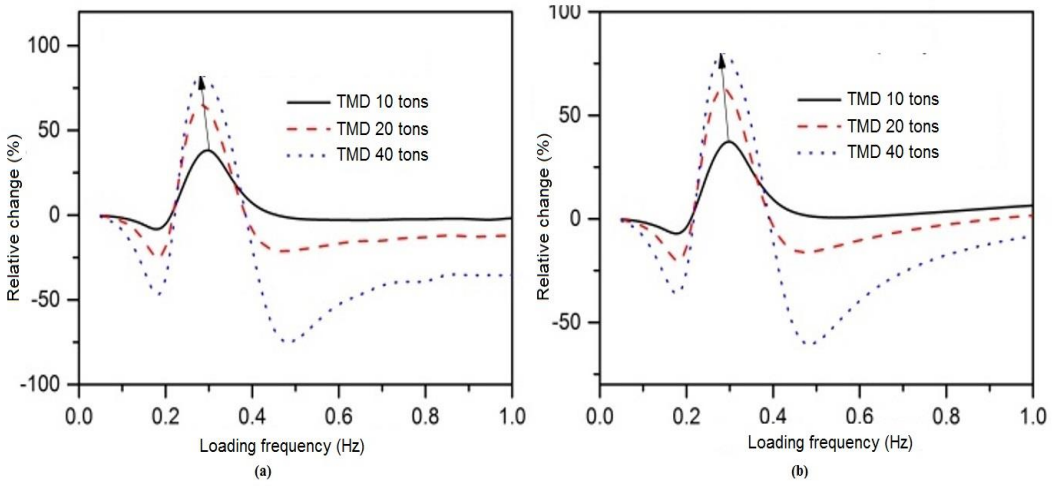

Figure 4.9 Relative change of (a) amplitude (b) standard deviation of deflection for different TMD masses

In order to investigate the effects of parameters of TMDs, a number simulations were run with different TMD spring stiffness and damping values and the standard deviation of the results for each time history was obtained and then a surface responses plot was built as depicted in Fig 4.10a. This graphical representation of TMD parameters is useful in finding the optimal values and to find out how TMD's efficiency changes. It should be noted that TMD mass was kept constant (20 tons) and only TMD stiffness and damping change. As the stiffness of TMD changes, the frequency of TMD changes, therefore it is expected that TMD's stiffness is a more important parameter in the surface responses plot and the responses are minimum when the stiffness is around 70000 N/m. Regarding damping values, it can be seen that an increase in damping reduces the responses. However, this change is more pronounced in lower TMD stiffness. Fig 4.10a displays a linear surface response plot in which a clear optimal value can be found. This surface plot was built for the model without position constraints.

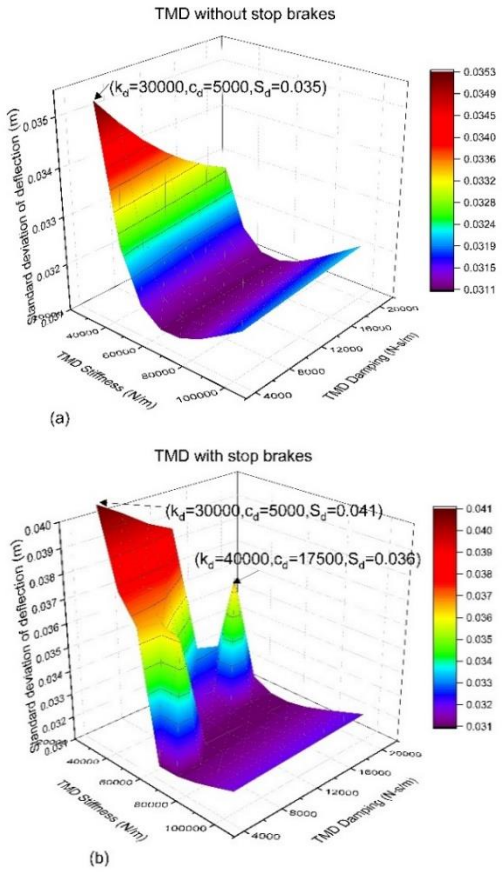

Figure 4.10 3D surface of standard deviation for the system (a) without stop brakes (b) with stop brakes

Since there is a limitation in space in the nacelle and the tower, position constraints should be modeled as stop brakes on the stroke of TMDs. The inclusion of stroke limiter is vital especially for floating offshore wind turbines in which there are larger deflections at the nacelle level. Hu and He (2017) [88] investigated an active mass damper system with a stroke limiter in which the strokes are limited. In this research, stop brakes are incorporated in the model as a spring which comes into contact with the TMD at a certain distance. The stiffness value of this stop brake and the maximum of stroke are two parameters in modeling space constraints. The maximum of stroke is assumed as 2.0 m and the stiffness value is assumed as 200 KN/m. After including this stop brake into the model, simulations were performed and surface response plot was constructed as in Fig 4.10b. It can be seen that the surface plot is nonlinear and this

nonlinearity is due to the effect of stop brakes. Furthermore, it is clear that the standard deviation of deflection increases for the case with stop brakes compared with the case without stop brakes. For instance, for a TMD stiffness of 30000 N/m and a TMD damping of 5000 N-s/m, the standard deviation increases from 0.035m to 0.041m, resulting in 17% increase in the standard deviation of dynamic responses.

4.4.3 Parametric Study of TLCD

This section describes a parametric study of controlled systems using TLCDs. First, the effect of the mass ratio of TLCD μ on the standard deviations of deflections is displayed in Fig 4.11a, in which it can be observed that higher TLCD mass ratios reduce the standard deviation of time histories more significantly under loading frequency equal to the natural frequency of the system. In addition, the suppression bandwidth of loading frequency is wider for higher mass ratios. For instance, the suppression bandwidth for the TLCD with the mass ratio of 0.5% is 0.27-0.33Hz, and it increases to a wider bandwidth of 0.24-0.35Hz when the mass ratio is increased to 2%; with approximately twice wider range of frequencies being suppressed. The normalized standard deviation for TLCDs with different ratios of the liquid horizontal length to its total length (B/L) is depicted in Fig 4.11b and suggests longer horizontal length of TLCDs weakens the dynamic responses more effectively and also it leads to wider suppression bands in which wider range of loading frequencies can be suppressed.

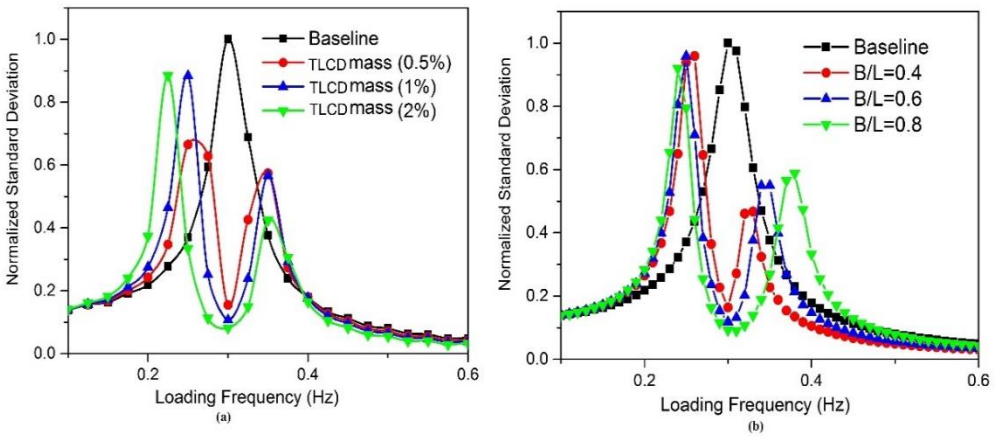

Figure 4.11 Normalized standard deviation (a) different mass ratios (b) different B/L ratios

4.4.4 Stochastic Loading

As harmonic loading is not the realistic loading pattern due to highly random nature of wind loading caused by turbulence, it is vital to investigate the behavior of the structural control devices in stochastic wind loading. This section focuses on stochastic time history using stochastic loading calculated per IEC standard [47] for operational and non-operational load cases.

4.4.4.1 Operational Loading

First, the effect of structural control devices on the vibration of the system under operational loading was studied. Fig 4.12a shows peak values of deflection and it can be seen that the maximum of the peak values occurs at rated wind speed due to the fact that maximum thrust force occurs at the rated wind speed in collective pitch control type of turbines. In partial loading conditions (wind speed lower than the rated wind speed), the optimal TMDs have a slight suppressive effect. However, TMD's performance in reducing peaks of deflection is better in fully loaded conditions (wind speed higher than rated wind speed). Fig 4.12b shows the standard deviation of responses and the figure suggests that the standard deviation increases in higher wind speeds. Also, the difference between the curves with and without TMDs increases as wind speed increases. Furthermore, increasing TMD mass from 20 to 40 tons causes even larger standard deviation of deflection in the fully loaded region. This means that increasing the mass of TMD does not necessarily improve the performance of this kind of structural controller as it results in higher flexibility of the system.

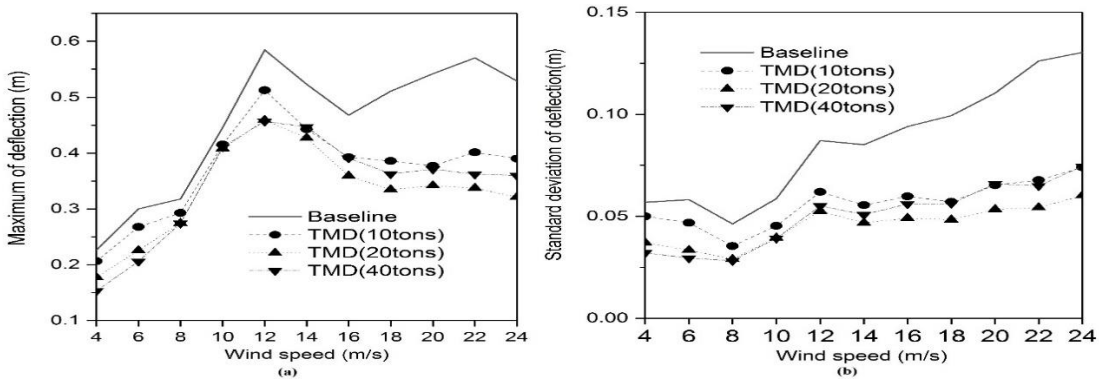

Figure 4.12 Deflection in operational conditions using TMDs (a) maximum (b) standard deviation

Next, similar simulations were performed for the systems controlled with TLCDs at different wind speeds and the results are depicted in Fig 4.13. As can be seen in this figure, TLCDs are effective in reducing the standard deviation of deflections at all wind speeds. Again increasing the mass of liquid in the optimal TLCD from 20 tons to 40 tons does not improve their suppression effects.

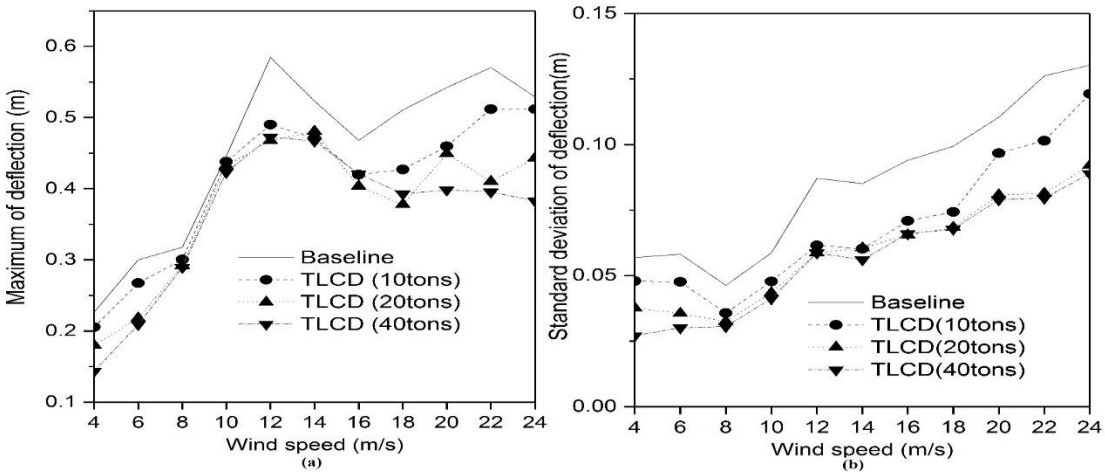

Figure 4.13 Deflection in operational conditions using TLCDs (a) maximum (b) standard deviation

Fig 4.14 compares the performances of TMD, TLD, and TLCD-TMDs with equal masses (20 tons) at different wind speeds compared to the uncontrolled system. The peak deflections (Fig 4.14a) and standard deviation of deflections (Fig 4.14b) are suppressed, however standard deviations experienced more significant reductions. At the rated wind speed, a combination of TMD and TLCD outperforms other devices in vibration control with 24 percent decrease in the peak deflections. In the partially loaded region, the curves for three vibration control devices are close to each other. It can be seen that the optimal TMD shows a better performance in operational conditions compared to the TLCDs.

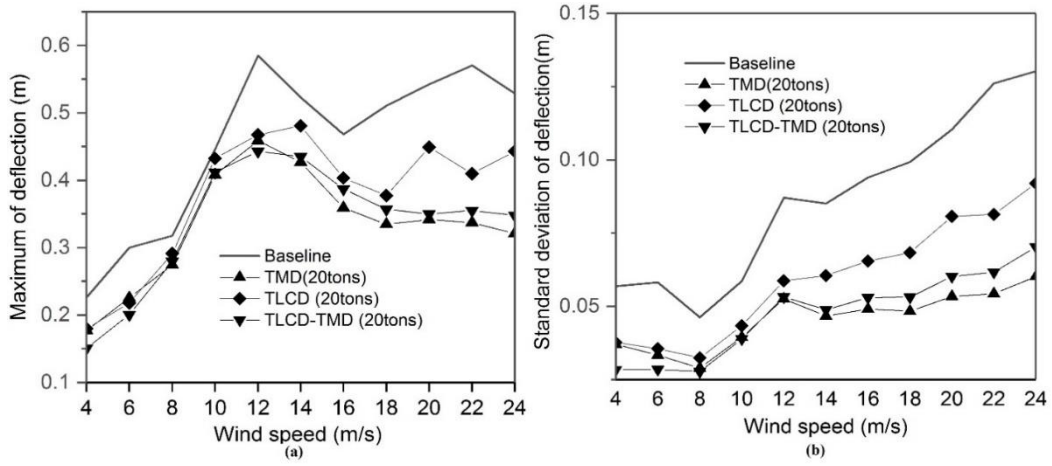

Figure 4.14 Deflection in operational conditions using TMD, TLCD, and TLCD-TMD (a) maximum (b) standard deviation

The trend for the standard deviation of deflections in terms of effectiveness of structural control devices is similar to those of maximum of peaks; with the optimal TMD showing better performance in the suppression of vibration followed by TLCD-TMD and TLCD. Also, a weaker performance of TLCDs at high operational wind speed is again proven for the standard deviation of deflection. The summary of the standard deviation of responses (absolute values and reduction percentage compared to the uncontrolled system) for different structural control devices at operational wind speeds are listed in Table 4.3. The optimal TLCD-TMD system has higher reduction percentage of standard deviation in all cases compared to TLCDs.

Table 4.3 Standard deviation of deflection for operational wind speed for TMD, TLCD, and TLCD-TMD (20tons)

Wind Speed (m/s)	Baseline	TLCD (20 tons)	TMD (20 tons)	TLCD-TMD (20 tons)
4	0.057	0.038(34%)	0.037(35%)	0.028(50%)
6	0.058	0.036(39%)	0.033(43%)	0.028(51%)
8	0.046	0.032(30%)	0.029(37%)	0.028(40%)
10	0.059	0.043(26%)	0.039(33%)	0.039(34%)
12	0.087	0.059(33%)	0.053(40%)	0.053(39%)
14	0.085	0.061(29%)	0.047(45%)	0.049(43%)
16	0.094	0.066(30%)	0.049(48%)	0.053(44%)
18	0.099	0.068(31%)	0.048(51%)	0.053(46%)
20	0.110	0.081(27%)	0.053(52%)	0.060(45%)
22	0.126	0.081(35%)	0.054(57%)	0.062(51%)
24	0.130	0.092(29%)	0.060(54%)	0.070(46%)

4.4.4.3 Non-Operational Loading

In non-operational loading conditions, rotors are not rotating and causing insignificant aerodynamic damping. Since aerodynamic damping is the biggest contributor to total damping in operational conditions, lack of this damping in non-operational conditions causes lower total damping and therefore results in high fatigue damage. Due to high frequency of occurrence of non-operational loading conditions and their high contribution to the total fatigue damage, the non-operational conditions such as parked condition may be considered design drivers. In this section, the effects of structural control devices on the responses of offshore wind turbine systems in parked condition are presented at different wind speeds. For the parked condition, the blades are feathered during the entire simulation. Fig 4.15 compares the maximum and standard deviation of deflection at the top of the tower equipped with TMD, TLCD and

combined TLCD-TMD with the uncontrolled system under parked conditions at different wind speeds. All vibration control devices reduce the peak and standard deviation values of responses to a great extent except for the TLCD at wind speed of 4m/s. In comparison, the vibration control devices have much higher positive performance under parked conditions due to the absence of aerodynamic damping and additional damping caused by these devices.

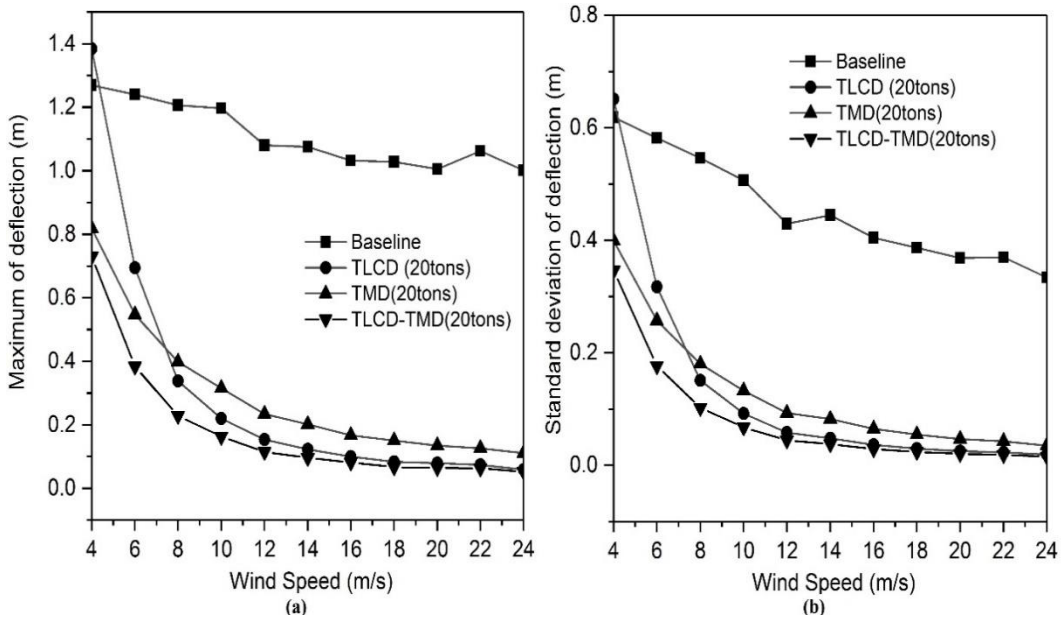

Figure 4.15 Deflection in non-operational conditions using TMD, TLCD, and TLCD-TMD (a) maximum (b) standard deviation

The percentage of reduction of the deflection compared to the uncontrolled system is demonstrated in Fig 4.16. It can be seen that TLCDs have better performance than TMDs at wind speeds higher than 6 m/s. In addition, the combined TLCD-TMD device has better performance than the rest of the devices, with the maximum of 93% reduction in the standard deviation of the responses for 24 m/s wind speed. Furthermore, there are trends in data to suggest that improvement percentage increases as wind speed increases.

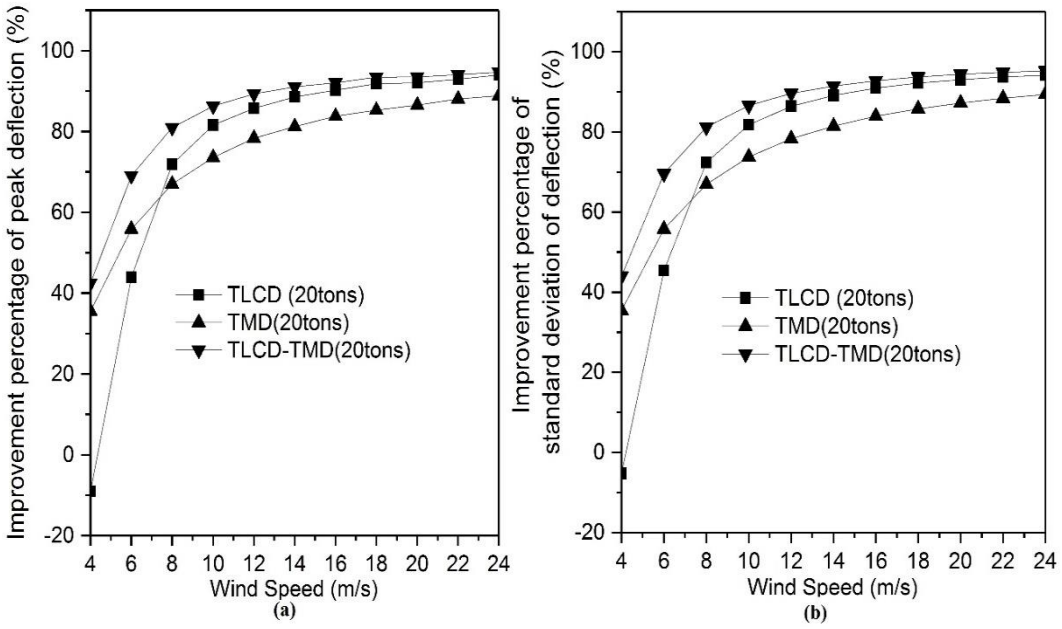

Figure 4.16 Improvement percentage of (a) maximum (b) standard deviation of deflection in non-operational conditions with TMD, TLCD, and TLCD-TMD

4.4.4.4 Startup and Shutdown Conditions

Wind turbines are switched on and off constantly in their lifetime due to weather conditions, maintenance, and other reasons. Therefore, it is important to investigate the effect of structural control devices on the offshore wind turbines in startup and shutdown conditions. The wind turbine studied in this research is controlled using a pitch-to-feather system. For startup conditions, the blades are pitched from feather (90º) to the run positions (12º) with a pitching rate of 2 deg/s during a time span of 39 sec allowing the wind to accelerate the rotor. To simulate shutdown conditions, the blades are pitched from normal angle (12º) to the feathered angle (90º). Fig 4.17 displays a representative 50 s time history of responses of the system after initiating the turbine at rated and cut-off wind speed using the mentioned structural control devices tuned to the first natural frequency of the system. The structural control devices show positive

performances in startup condition and this improvement is more pronounced at rated wind speed with the combined TLCD-TMD device.

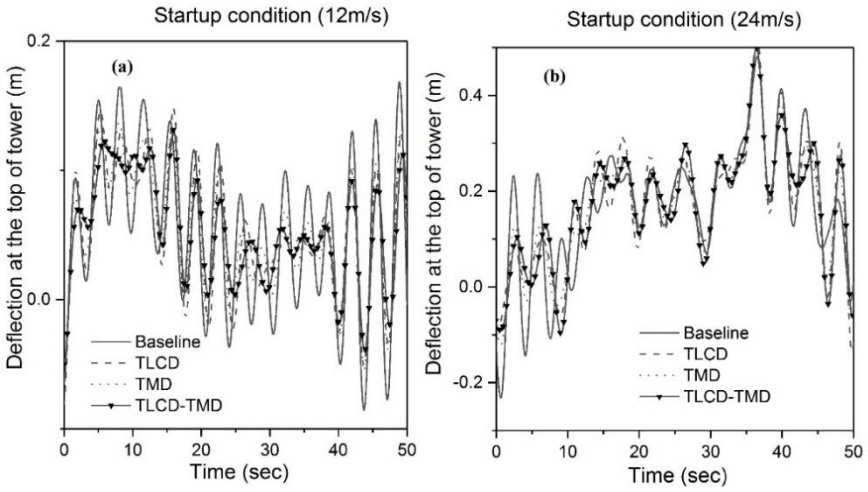

Figure 4.17 Time history of deflection in startup condition at wind speed (a) 12m/s (b) 24m/s using TMD, TLCD, and TLCD-TMD

The shutdown condition is assumed as normal with a pitch rate of 2 deg/s in which the blades are pitched from 12º to 90º during a time span of 39 sec. Fig 4.18 compares the responses of the controlled and uncontrolled system under shutdown condition. The structural control devices improve the structural responses, with the maximum improvement observed at rated wind speed (Fig 4.18a). In comparison, at the cut-off wind speed (Fig 4.18b) the optimal TLCD shows negative performance in some part of the time history, whereas the optimal TLCD-TMD is proved to outperform other devices during the whole time span.

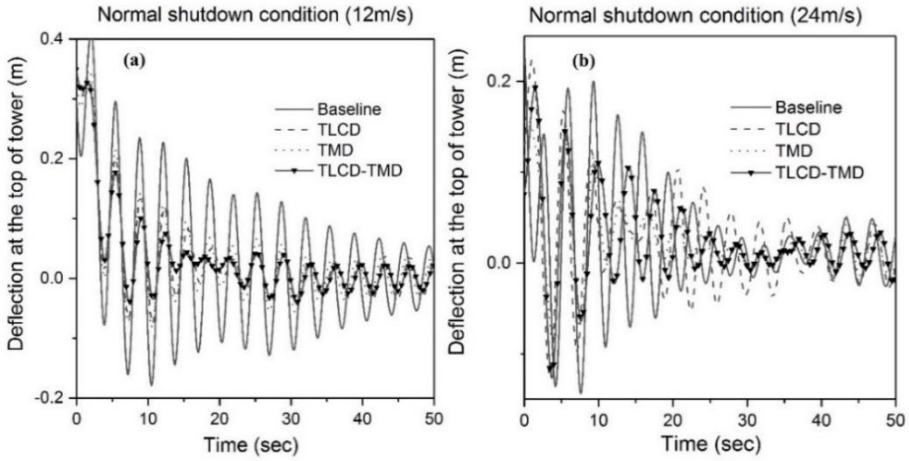

Figure 4.18 Time history of deflection in shutdown condition at wind speed (a) 12m/s (b) 24m/s using TMD, TLCD, and TLCD-TMD

4.6 Conclusion

In this chapter, the use of two passive structural control devices, i.e. tuned mass dampers and tuned liquid column dampers, in fixed offshore wind turbine foundations was investigated. A multiple lumped mass model for jacket foundations including structural control devices was developed. First, OWT foundation was subjected to various loading including initial perturbation, monotonic, impulsive, and harmonic loading conditions. A parametric study of the mentioned structural control devices was performed. Next, stochastic wind loading was applied to the system at various wind speeds for operational, parked, startup and shutdown conditions. The main findings of this study are as follows:

1. The optimal TMD has higher damping contribution to the total damping of the system compared to the system with the optimal TLCD in free decay vibration.
2. The results show that heavier tuned mass dampers dampen out a wider range of applied frequencies, however, they increase the vibration amplitudes for loading frequencies outside that bandwidth in a larger extent.
3. In operational conditions, the optimal TMD outperforms other devices as the standard deviations of the responses are reduced more than 55% when the liquid

mass was 20 tons. The optimal TLCD-TMD and TLCD are in the next orders with the maximum of 51% and 39% reduction, respectively.

4. In parked conditions, all the devices show greater performances compared to the operational conditions due to the absence of aerodynamic damping and presence of loading with frequencies closer to the frequency in which the devices are tuned to. This performance becomes better when wind speed increases with the maximum of 93% reduction in the standard deviation of deflection at wind speed 24 m/s for the TLCDs. Furthermore, TLCDs show higher vibration suppression capacity than TMDs in all wind speeds.
5. In startup and shutdown conditions, all control devices show positive performance in attenuating dynamic responses at rated wind speed. However, the optimal TLCD causes a slight increase in the responses at the cut-off wind speed due to its inability to adjust to the highly dynamic motion of the structure.
6. Since TMDs are more efficient in operational conditions, and TLCDs have better performance in parked conditions and due to the fact that the total fatigue damage is caused by the contribution of all the conditions, the combined TLCD-TMD can introduce better overall performance in whole lifetime of the system. The combined system can consist of a TMD installed in the nacelle and a TLCD installed inside the tower. To apply the combined TLCD-TMD in practice, more comprehensive studies with a focus on experimental investigations may be useful.

Chapter 5 Fragility Analysis

5.1 Introduction

High flexibility of offshore wind turbines (OWTs) makes them vulnerable to excessive vibrations. This chapter presents vibration control of offshore wind turbines induced by multi-hazard excitations. A model consisting of entire offshore wind turbine foundation and tower controlled by tuned liquid column dampers (TLCD) considering nonlinear soil pile interaction is established. The model is subjected to wave, wind, and seismic loading. The effect of severity of earthquake on the performance of the structural control device is investigated. A fragility analysis based on acceleration capacity thresholds is performed to estimate reliability improvement using the structural control devices. The fitted fragility functions based on multiple stripes analysis are constructed and compared with the empirical cumulative distribution curves. The results suggest that the use of an optimal TLCD with a mass ratio of 2.5% reduces the fragility of the system by as much as 6% and 12% for operational and parked conditions, respectively.

5.2 Motivation

Due to the fact that the wind farms developed in the last two decades were located in the places where earthquake events rarely occur, few studies considering seismic loading have been performed. There have been two main approaches regarding seismic hazards in wind turbines: deterministic and probabilistic. The fragility analyses performed in the previous studies were mostly based on conventional methods. Baker [52] investigated the effectiveness of various methods for fragility analysis under seismic loading based on drift threshold for general structures and showed that multiple stripe analysis produces more efficient fragility functions compared to other conventional methods. However, the applicability of this method for offshore wind turbines under multi-hazard condition should be investigated.

To fill aforementioned gaps, the present study investigates the structural control of the offshore wind turbines under multi-hazard conditions considering nonlinear soil pile interaction and a fragility analysis using multiple stripes analysis is performed for the model and reliability improvement is discussed. Tuned liquid column dampers are considered as the structural control device in this study because it can be installed not only in the nacelle but also in various elevations of the tower and also it requires a lower level of maintenance. The novelty of this study can be explained in two parts. On one hand, the structural dynamic responses such as displacement and base shear forces are investigated for the offshore wind turbine modelled as multi-degrees of freedom considering nonlinear soil pile interaction and equipped with the optimal structural control device. Wind, wave, seismic and gravity loadings are incorporated into the model. On the other hand, a fragility analysis based on the acceleration threshold is constructed for the controlled and uncontrolled systems in order to estimate the reliability improvement offered by the structural control devices. To perform a more robust fragility analysis, an optimized method of fragility analysis named multiple striped analysis is used that has not been utilized for offshore wind turbine systems.

5.3 Numerical Model

The equation of motion of a three-dimensional monopile wind turbine model equipped with TLCDs is established and solved using nonlinear Newmark method [67]. Details of the equation of the motion, wind turbine model, and soil-pile interaction are presented in the third chapter. Fig 5.1 shows a schematic configuration of a TLCD attached to the main structure.

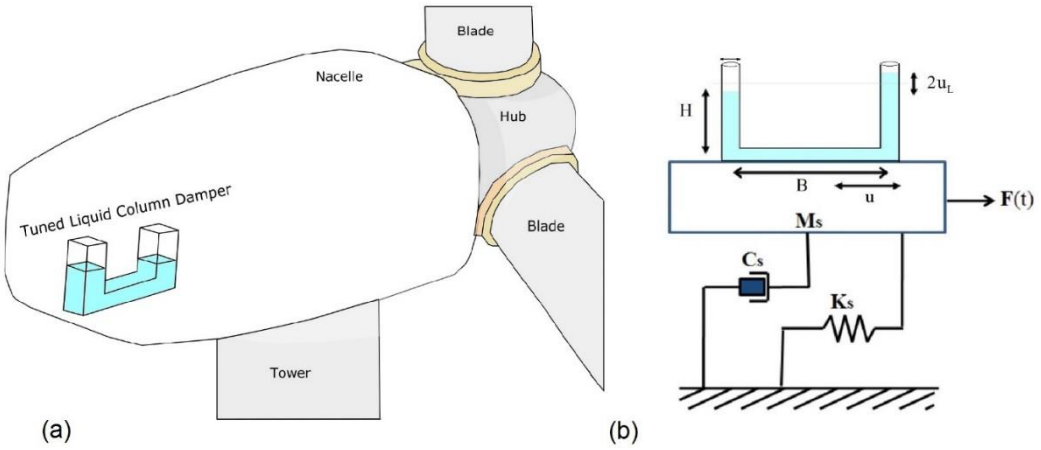

Figure 5.1 Schematic diagram (a) turbine (b) tuned liquid column damper

The arrangement of the baseline TLCD for this chapter is a TLCD with a mass ratio of 2.5% located in the nacelle. The type of the liquid is selected as water, resulting in a need for 22.675 m^3 space. This required volume can be reduced by using other liquids such as glucose solution with a density of 1540 kg/m^3, resulting in 35% saving in the required space. Alternatively, using multiple tuned liquid column dampers in nacelle and tower can be another practical solution. Here one single TLCD is assumed to be installed in the nacelle. The optimal tuning ratio is set as $\gamma = 1/(1+\mu)$ and other parameters are tabulated in Table 5.1.

Table 5.1 TLCD parameters

Mass ratio (μ)	2.5%	Total length (L)	9.89m
Frequency ratio (γ)	97.5%	Horizontal length (B)	5.93m
Length ratio (α)	0.6	Headloss coefficient (ξ)	0.3

In this study, NREL 5 MW wind turbine was considered as it is widely used as the turbine for benchmark studies [64]. This turbine is supported by baseline monopile foundation developed in the second phase of Offshore Code Comparison (OC3) project [70] conducted by NREL. The total length of the monopile is 66 m, in which 10 m, 20 m, and 36 m are above the mean sea level, in the water and under the seabed, respectively. The general configuration of the turbine is shown in Fig 3.20. The total offshore wind turbine system is modeled by three-dimensional Timoshenko beam theory.

The particulars of the offshore wind turbine can be found in Table 3.2. Table 3.4 tabulates the material properties of the steel used in the tower and monopile of the offshore wind turbine. The density of the steel in the tower is taken higher than that of the regular steel to take into account the weight of the paint, bolts, welds, and flanges which are not modeled directly [62].

Soil layer properties are shown in Fig 3.26a. The nonlinear resistance-deflection curves constructed based on the aforementioned method for different soil layers are illustrated in Fig 3.26b.

5.4 Numerical Results

5.4.1 Dynamic Response of Uncontrolled OWTs

In this section, the responses of the uncontrolled offshore wind turbine structure under multi-hazard conditions are discussed to give a preliminary insight into the dynamic responses. Not to further complicate the problem, the structural control devices are not considered in this subsection. Two major excitation scenarios are considered. In the first scenario, LC1, the turbine is operating under wind and wave loadings at the rated wind speed and the seismic event occurs at the instant of 100 s. The rated wind speed is the minimum wind speed at the hub in which the turbine generates the maximum electricity and this wind speed is selected as the most probable operational wind speed according to the probability distribution. In the second scenario, the parked turbine is subjected to higher wind and wave loadings in conjunction with the impact of earthquake excitation which comes in at the instant of 100 s. The detailed environmental parameters are listed in Table 5.2. The damping ratios used in this study are taken as 5% and 1% of critical damping for the operational and parked conditions, respectively, as used in the previous studies [44, 89, 90].

Table 5.2 Loading condition information

	Wind loading		Wave loading		
	Wind speed at the hub height (m/s)	Turbulence intensity (%)	Wave period (sec)	Significant wave height (m)	Damping
LC1	11.4	14.5	9.5	5.0	1%
LC2	40.0	11.7	11.5	7.0	5%

Fig 5.2 shows the sea elevation time history for the two cases. Fig 5.3 illustrates time history of the resultant wave loading acting on the monopile at the mean water level for two load cases. The maximum wave loading for the operational condition with 5 m significant wave height is 2300 kN. The corresponding value for the parked condition is 3900 kN when the significant wave height is 7 m, resulting in 69% increase in wave loading due to 40% increase in significant wave height. It is assumed that wind and wave loading apply in the same direction. Fig 5.4 shows the simulated wind forces for operational and parked conditions. It should be noted that even though values of wind loading are smaller than total wave loading, they have more impact on the dynamic responses as wind loading applies at higher height resulting in much larger moment values. Comparing Fig 5.4a with Fig 5.4b, it is clear that in the operational condition wind loading comprises a considerable mean constant value (around 650 kN in this simulation) and a turbulent component. This large mean constant force is due to the fact that the blades are faced toward the wind inflow at which most of the wind loading is facing the blades. On the other hand, in the parked condition shown in Fig 5.4b, the mean component is around zero because in the parked condition the blades are pitched in a way that they are subjected to the minimum wind loading resulting in a mean value close to zero.

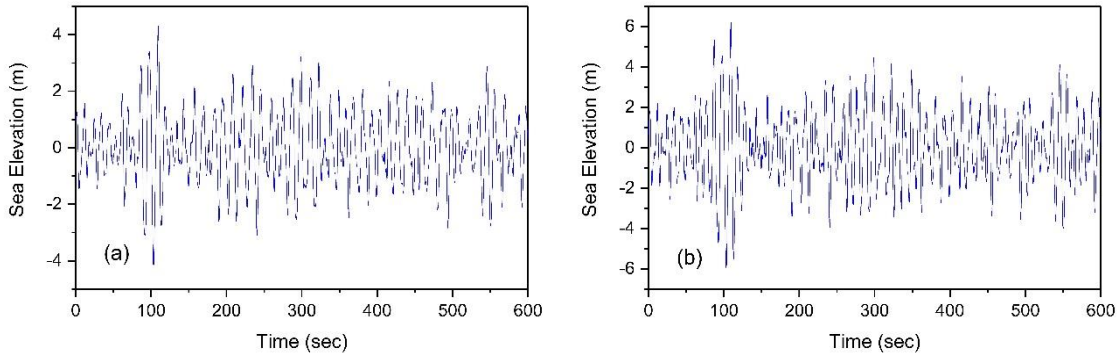

Figure 5.2 Sea elevation time history (a) operational (b) parked

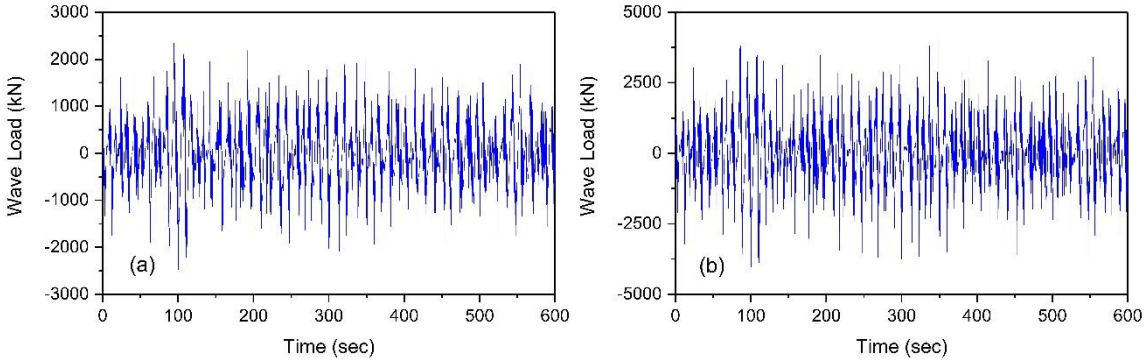

Figure 5.3 Time history of total wave loading on the monopile (a) operational (b) parked

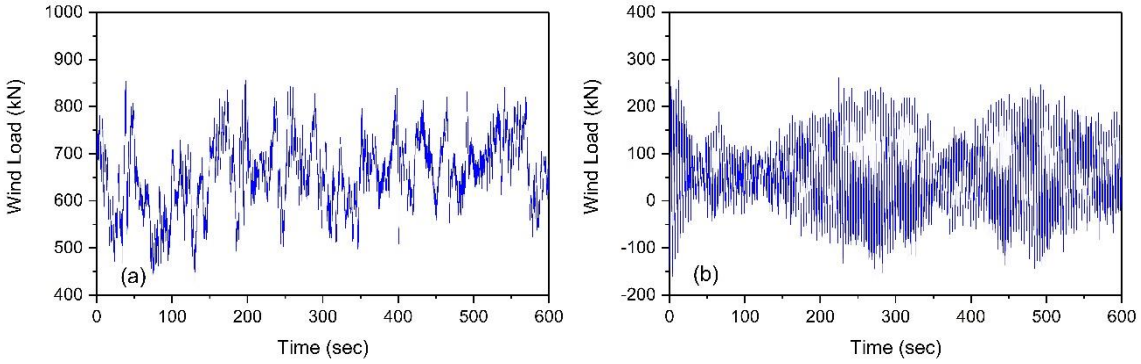

Figure 5.4 Time history of total wind loading on the top of the tower (a) operational (b) parked

In order to give a preliminary insight into the impact of seismic loading on the dynamic responses**,** the responses of the system under only one seismic record are presented in the figures for the sake of brevity. Fig 5.5 compares the responses of the structure under wave-wind loadings and wave-wind-seismic loadings without any structural control devices. At the first glance, it is clear that fore-aft displacement fluctuates around a high mean value of 0.5 m in the operational condition. However, this corresponding response for parked conditions has a very low mean value. This is again due to the fact that in operational conditions blades are positioned in a way to absorb the maximum of wind loading. It is worth mentioning that the maximum of deflection occurs at the instant of 118 s, 18 seconds after the earthquake motion starts. Furthermore, the maximum fore-aft displacement increases from around 0.76 m to 0.93 m, resulting in 22% increase, when the earthquake excitation exists. This increase

is more pronounced for the parked condition as the maximum of deflection increases from 0.1 m to 0.34 m, resulting in 250% change. This jump in the fore-aft deflection affects the serviceability of the whole system since the devices such as inverters, transformers, and electrical generators are highly sensitive to excessive vibrations especially those caused by large accelerations. Therefore, implementation of a structural control device to mitigate this additional acceleration is necessary and assessed in the next sections.

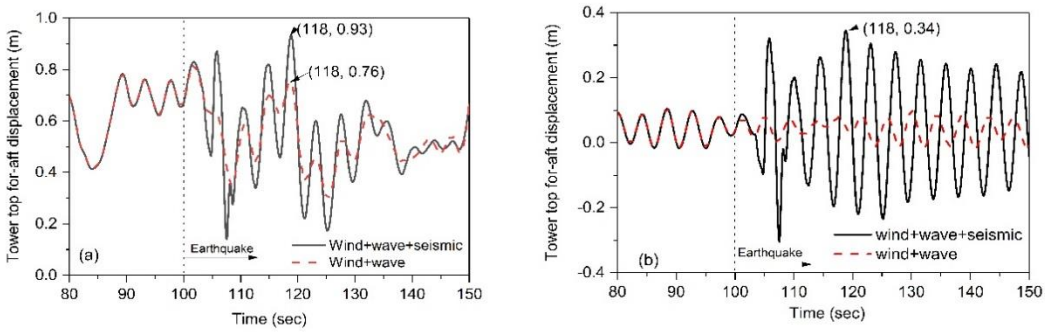

Figure 5.5 Tower top fore-aft displacement time history (a) operational (b) parked

Fig 5.6 and Fig 5.7 show time history of base shear and base moment, respectively. The peak values occur at the instant of 105 sec. Comparing this with the corresponding peak values of deflection in Fig 5.5, it is clear that the pile experiences the maximum responses 13 seconds before the top of the tower. This is due to the high slenderness of the system. Comparing the base shear time histories for two loading conditions (Fig 5.6a and Fig 5.6b), the maximum values appear at the instant of 105 sec and the values are almost identical. This shows that these maximum values are highly affected by seismic excitation. However, the corresponding peak values for base moments (Fig 5.7a and Fig 5.7b) are not identical. For instance, the base moment at the instant of 105 sec is 99780 kNm for operational condition, whereas the corresponding value for the parked condition is 54660 kNm.

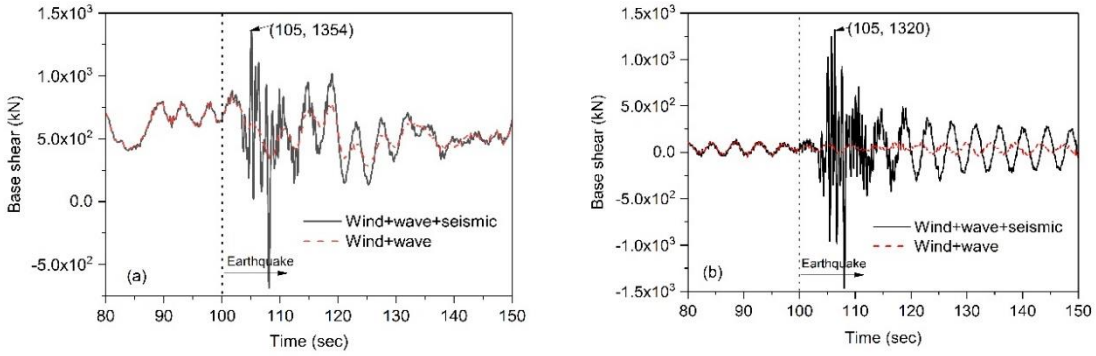

Figure 5.6 Fore-aft base shear time history (a) operational (b) parked

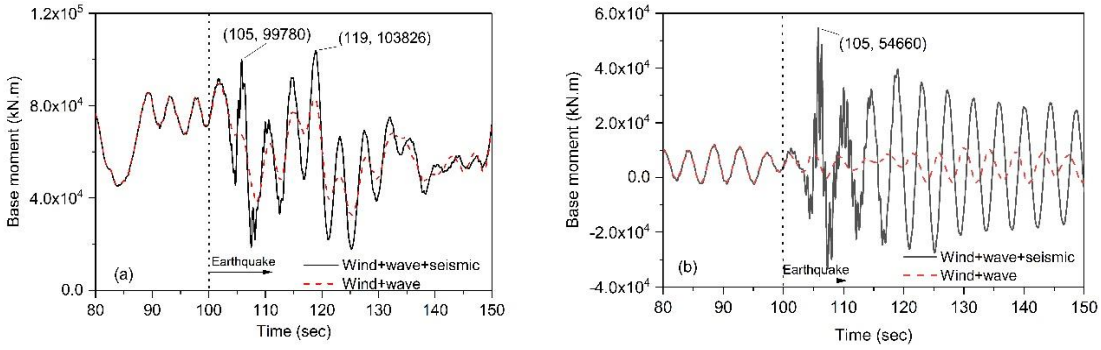

Figure 5.7 Base moment time history (a) operational (b) parked

Power spectral density (PSD) of time history is calculated using Fourier analysis. Fig 5.8 shows the power spectral density (PSD) of tower top displacement for the operational and parked conditions. For the operational condition (Fig 5.8a), the first peak appears close to zero due to energy spectrum from wind loading, and the second peak occurs at the frequency of 0.24 Hz which corresponds to the first natural frequency of the system. For the parked condition (Fig 5.8b), there is a peak at the frequency of 0.24 Hz corresponding to the first natural frequency. In this figure, it is clear that the energy spectrum of wind with the frequencies lower than 0.1 Hz is much lower compared to the operational condition because in the parked condition the system is absorbing a small portion of wind loading as a result of pitching mechanism in the blades. Comparing the PSD plots with and without seismic loading, an increase in PSD especially for the frequencies close to the natural frequency of the system is observed due to earthquake motions. This increase in the peak values of PSD is more

pronounced for the parked condition due to the fact that there is a lower total damping in the parked condition because of the lack of aerodynamic damping. Furthermore, the figure shows that earthquake energy lays in the broader frequency range.

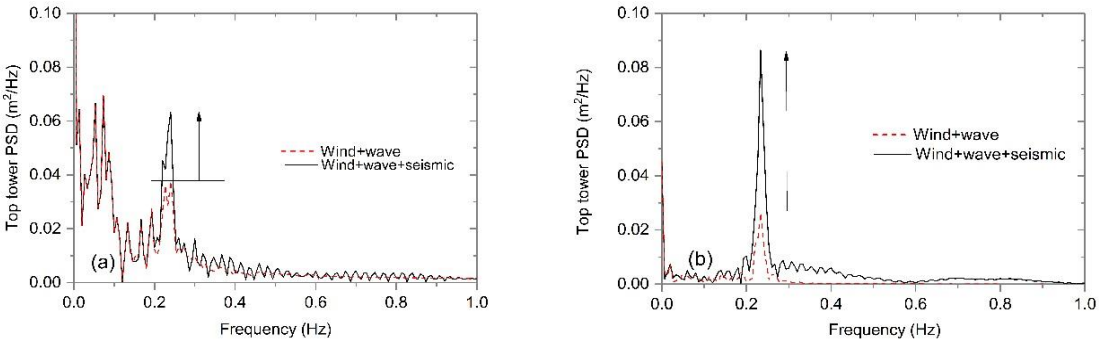

Figure 5.8 PSD of the fore-aft top tower displacement (a) operational (b) parked

5.4.2 Dynamic Response of OWTs with TLCDs

To mitigate the vibrations of offshore wind turbines subjected to environmental and seismic loadings, the baseline optimal TLCD as defined in Table 5.1 is used. Fig 5.9 compares the responses of the controlled and uncontrolled structure under wave-wind-seismic loadings . For two loading conditions, it is obvious that the TLCD reduces the amplitudes of vibration and this reduction is more pronounced after the instant of 100 sec when the earthquake occurs. For the operational condition (Fig 5.9a), the peak value decreases by 13% from 0.93 m to 0.81 m due to the extra damping caused by the TLCD. For the parked condition, the peak is halved from 0.34 m to 0.17 m, resulting in 50% decrease.

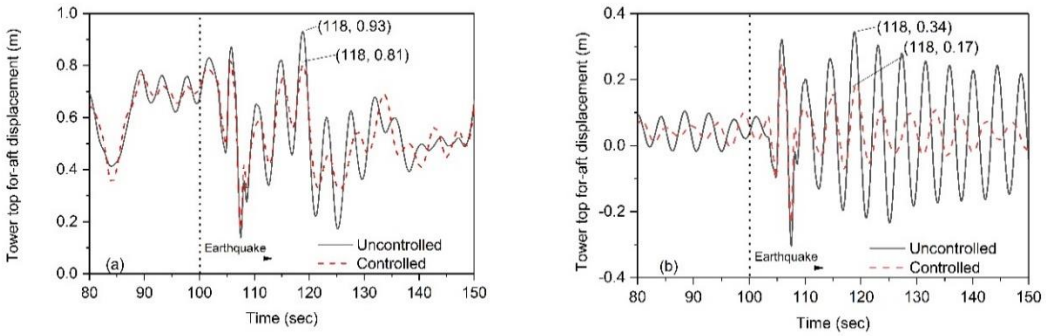

Figure 5.9 Time history of tower top fore-aft displacement (a) operational (b) parked

Fig 5.10 shows time histories of base shear forces. The figure shows that the TLCD is more efficient in mitigating the vibrations of seismic loading after the instant of 115 sec. This means that the TLCD is not able to work effectively in the first few seconds of the earthquake motions as it needs more time to adjust and respond to the seismic vibrations. For the vibrations before the instant of 115 sec, the controlled and uncontrolled systems have nearly similar base shear values. Fig 5.11 compares the base moment time histories for the controlled and uncontrolled systems for two loading conditions. The similar trend for the base moment can be seen. The controlled system experiences 13% and 43% reduction in the peak values of the base moment for the operational and the parked condition, respectively.

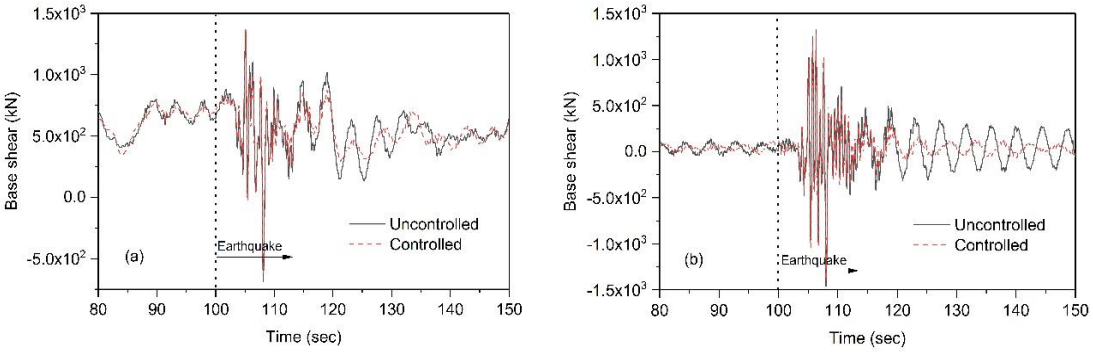

Figure 5.10 Fore-aft base shear time history (a) operational (b) parked

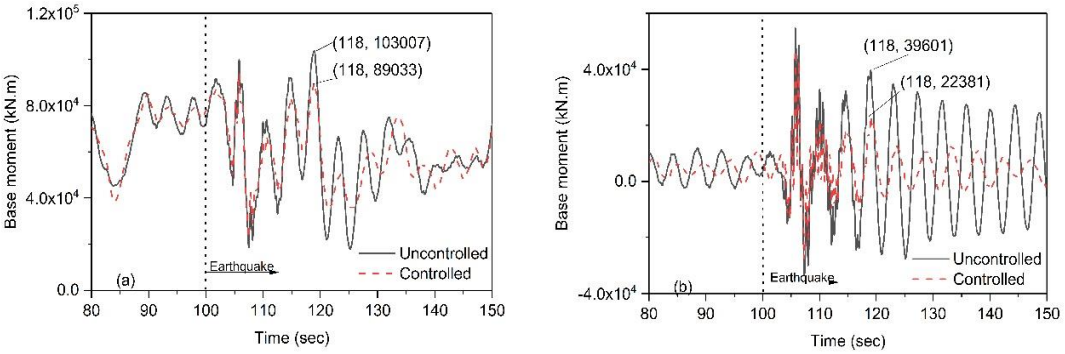

Figure 5.11 Base moment time history (a) operational (b) parked

Fig 5.12 shows the power spectral density (PSD) of tower top displacement for the controlled and uncontrolled system. For both loading conditions, the PSD values in the range close to the natural frequency of the system are reduced as the optimal structural control device is tuned to the natural frequency of the system. It is clear that the reduction in the peak of PSD is more significant for the parked condition.

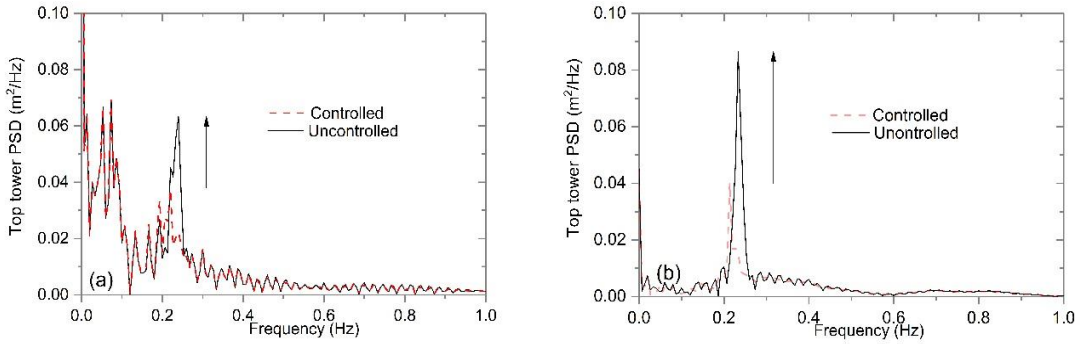

Figure 5.12 PSD of fore-aft displacement for controlled and uncontrolled systems (a) operational (b) parked

To investigate the effectiveness of the structural control systems on the excessive vibration of offshore wind turbines, the standard deviation of fore-aft displacement is tracked since the standard deviation of dynamic responses is a better representation for the fluctuation level of vibration. The standard deviation is compared to the uncontrolled wind turbine. To quantify this, the reduction coefficient of standard deviation is used as follows:

$$R_{\sigma} = \frac{\sigma_{Uncontrolled} - \sigma_{Controlled}}{\sigma_{Uncontrolled}} \tag{5.1}$$

where $\sigma_{Uncontrolled}$ and $\sigma_{Controlled}$ are the standard deviation of fore-aft displacement of the top tower without and with TLCDs, respectively.

To scrutinize the performance of the optimal structural control device for mitigating the structural responses under earthquake excitations, the dynamic response of offshore wind turbine is simulated under wave and wind loading in conjunction with earthquake ground motions with the peak ground acceleration ranging from 0.05g to 0.95g. The earthquake accelerations are scaled based on predefined peak ground acceleration (PGA) range and an optimal TLCD with the chosen mass ratio of 0.025 and the reduction coefficient of standard deviation is calculated and plotted in Fig 5.13a and Fig 5.13b for operational and parked conditions, respectively. As can be seen in the figures, the reduction coefficients for most earthquake records decrease when the peak ground acceleration of the earthquakes increases. This means that the effectiveness of tuned liquid column dampers for mitigating vibration of offshore wind turbine systems is higher for low-intensity earthquake records. This is expected as tuned liquid column dampers are more efficient for low amplitude vibrations [33, 91]. For operational conditions, the reduction coefficient for two of earthquake records becomes even negative for peak ground accelerations larger than 0.3g due to the existence of very large vibration amplitudes resulting in the inability of the dampers to perform. It should be noted that the probability of occurrence of earthquakes with low peak ground accelerations is higher than that of high-intensity earthquakes. The average of reduction coefficient for all records for operational and parked conditions are also shown in Fig 5.13a and Fig 5.13b, respectively. The reduction coefficient varies between 12-20% for the operational condition for PGA ranging from 0.05g to 0.95g. However, corresponding value for the parked condition is much higher, varying between 23-39%. This trend can be justified since total damping of the system for the parked condition is lower due to the absence of aerodynamic damping and the TLCD compensates for it.

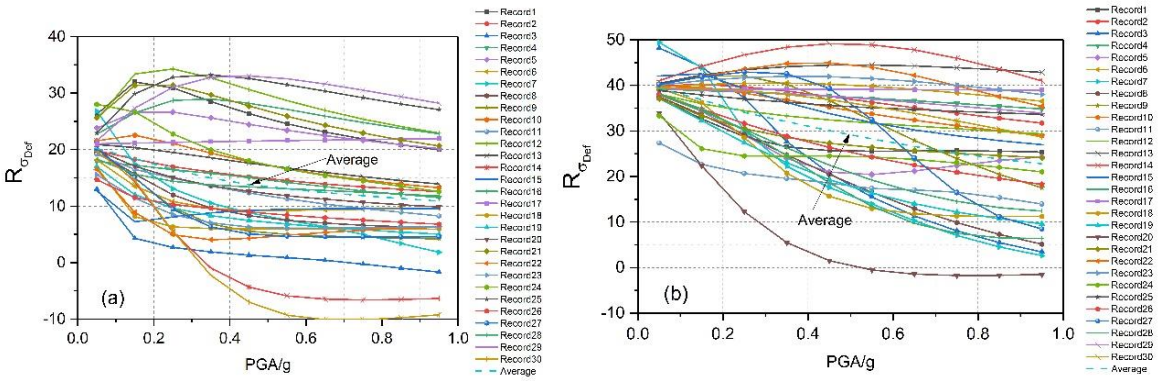

Figure 5.13 Reduction coefficient of the standard deviation of dynamic responses under multi-hazard conditions with different PGAs (a) operational (b) parked

To investigate the effect of TLCD mass ratio on the performance of the optimal structural control device for mitigating the structural responses, the dynamic response of offshore wind turbine is simulated under multi-hazards with the peak ground acceleration of 0.1g for different TLCD mass ratios ranging between 0 and 0.1. Then the reduction coefficient of the standard deviation of deflection and accelerations at the nacelle elevation for operational and parked conditions is captured and depicted in Fig 5.14 and Fig 5.15. With regard to the deflection in the operational condition (Fig 5.14a), the reduction coefficient of standard deviation of deflection is mostly positive for small TLCD mass ratios (lower than 0.15). When the mass ratio increases, the reduction coefficient decreases for some ground motions. Unlike operational condition, the reduction coefficients for the parked condition is positive for all seismic records (Fig 5.14b). It is interesting that the reduction coefficient does not increase necessarily by increasing TLCD mass ratios. For most seismic records, the effectiveness of TLCDs in mitigating deflections reduces for mass ratios larger than 0.15.

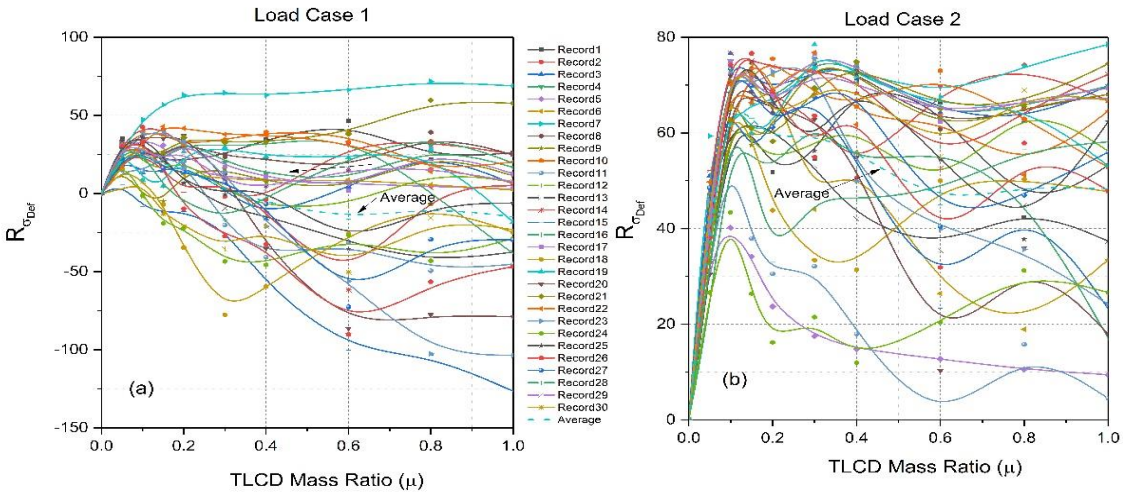

Figure 5.14 Reduction coefficient of the standard deviation of deflections in the nacelle under multi-hazard conditions with different TLCD mass ratios (a) operational (b) parked

Similarly, the reduction coefficient of the standard deviation of acceleration in the nacelle elevation is depicted in Fig 5.15 for operational and parked condition. At the first glance, it is clear that there is no negative reduction coefficient of acceleration even for larger TLCD mass ratios and the values of reduction coefficient are larger compared to those for deflection (Fig 5.14). This means that TLCD is more efficient in mitigating the acceleration rather than deflection. Furthermore, the reduction coefficient of acceleration mostly increases when the TLCD mass ratio increases, with maximum 75%.

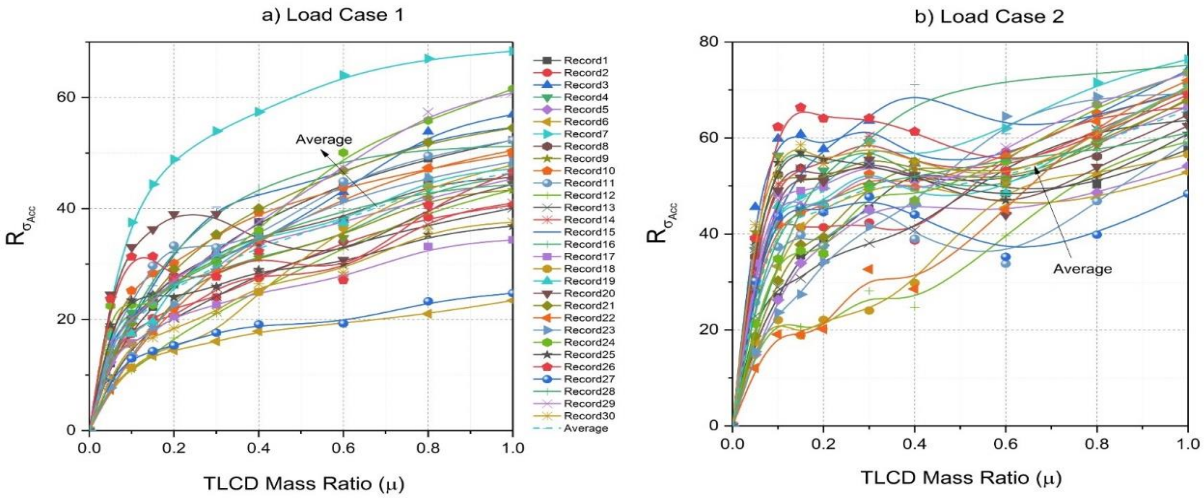

Figure 5.15 Reduction coefficient of the standard deviation of accelerations in the nacelle under multi-hazard conditions with different TLCD mass ratios (a) operational (b) parked

5.5 Fragility Analysis

The reliability improvements of TLCD-mounted wind turbines excited by environmental loading (wave and wind) in conjunction with earthquake ground motions are assessed by developing fragility curves. Excessive vibrations of wind turbines under multi-hazard damage the vibration-sensitive equipment inside the nacelle and reduce serviceability of the system resulting in inhibition of energy conversion [92]. Therefore, implementing structural control devices in the design of offshore wind turbines can improve the reliability of the mentioned equipment. The reliability improvements of the vibration controllers can be estimated by performing fragility analysis of the components [93]. In this study, a fragility analysis is performed based on the acceleration-based capacity limit state. In structural risk assessment, fragility functions are defined to estimate the probability of the event in which the demand (D) reaches or exceeds a certain capacity limit (C) for a given intensity measure (IM) of seismic excitations.

$$Fragility = P[C - D \le 0 \,|\, IM] \tag{5.2}$$

The fragility function in Eq. (5.2) is assumed as a lognormal cumulative distribution function defined in the following formulation [91, 94]:

$$P[C \mid IM = x] = \Phi\left(\frac{\ln(x/\theta)}{\beta}\right) \tag{5.3}$$

where $P[C \mid IM = x]$ is the probability that the demand of the structure exceeds the capacity under the excitation of a ground motion with $IM = x$, $\Phi(\bullet)$ is the standard normal cumulative distribution function, θ is the median values of the fragility function which can be defined as the *IM* level with 50% probability of failure, and β is the dispersion of *IM* (the standard deviation of *IM).* Generating fragility function curves based on the above formula requires estimating θ and β from the nonlinear structural analysis. Here we refer the estimation of these parameters as $\hat{\theta}$ and $\hat{\beta}$.

There are various procedures for estimating fragility function parameters based on the nonlinear dynamic analysis. The most common method is incremental dynamic analysis (IDA), in which ground motions are increased incrementally to find the *IM* level at which the demand surpasses the capacity of the structure [95]. Truncated incremental dynamic analysis is the second method which is the modified version of IDA method in which the lower number of samples are required [52]. Multiple stripes analysis (MSA) is another method, where a specified selection of *IM* levels for a group of ground motions are used and structural analyses are performed for each *IM* level to estimate failure probability. Multiple stripes analysis is chosen for this study as the most appropriate methodology since other methods require scaling ground motions up to very high values in order to find the *IM* level at which the criteria of failure is met and these *IM* levels are not practical and may lead to large nonlinearities and instabilities due to high slenderness of offshore wind turbine foundations. The second reason for choosing the MSA method is that it is less computationally expensive.

Fig 5.16 illustrates the flowchart of the methodology used in this research. In this method, nonlinear structural analyses are performed at a discrete selection of *IM* levels for a sample of ground motions. It should be noted that in this study the demand is chosen as the nacelle's accelerations since it is a measure of serviceability of the sensitive mechanical and electrical components inside the nacelle. The capacity in this study is the acceleration threshold at which the equipment inside the nacelle faces damages or misfunction. Here three acceleration thresholds of 7.5 m/s^2, 12.5 m/s^2, and

17.5 m/s^2 corresponding to acceleration thresholds in which functionality of generators, inverters, and electrical controls can be affected, respectively [92].

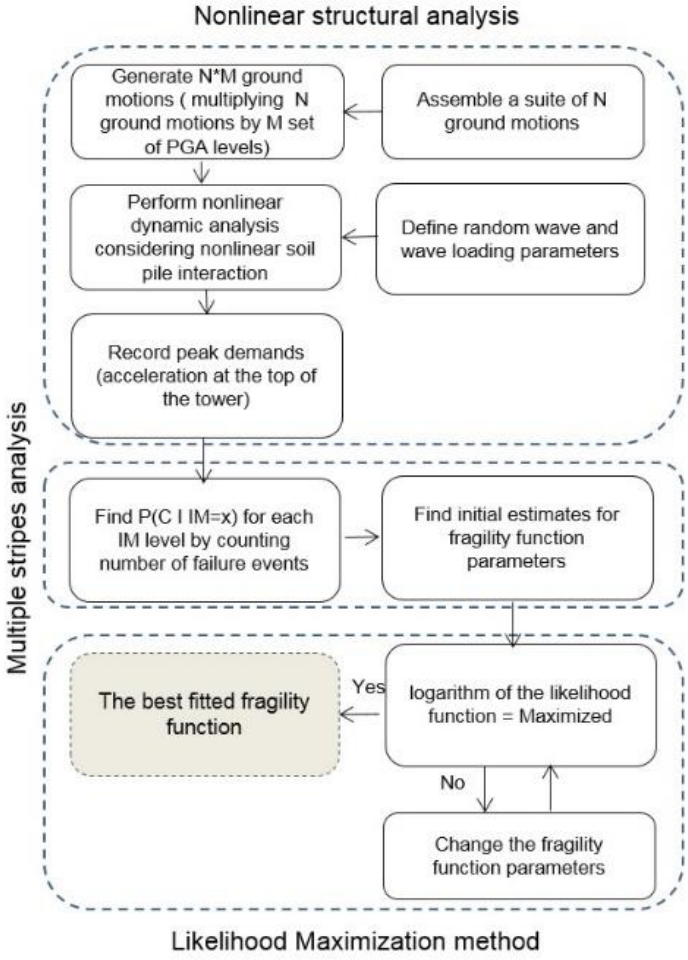

Figure 5.16 Fragility analysis based on MSA method

We can find the fraction of the ground motions at each intensity level *IM* at which the demand (accelerations) exceeds the capacity (acceleration threshold). The recorded data for the uncontrolled offshore wind turbine is shown in Fig 5.17 for three limit states. The probability of failure corresponding to each limit state at a given *IM* level can be calculated as the fraction of the records at which the peak acceleration of the nacelle exceeds the limit state. It can be seen that the number of failures increases with increasing *IM* levels. Then similar MSA analysis with the same loading for the system controlled with the optimal TLCD is performed and the results are shown in Fig 5.18. It can be seen that the points in the figure are shifted to lower values and the number of the failures are decreased.

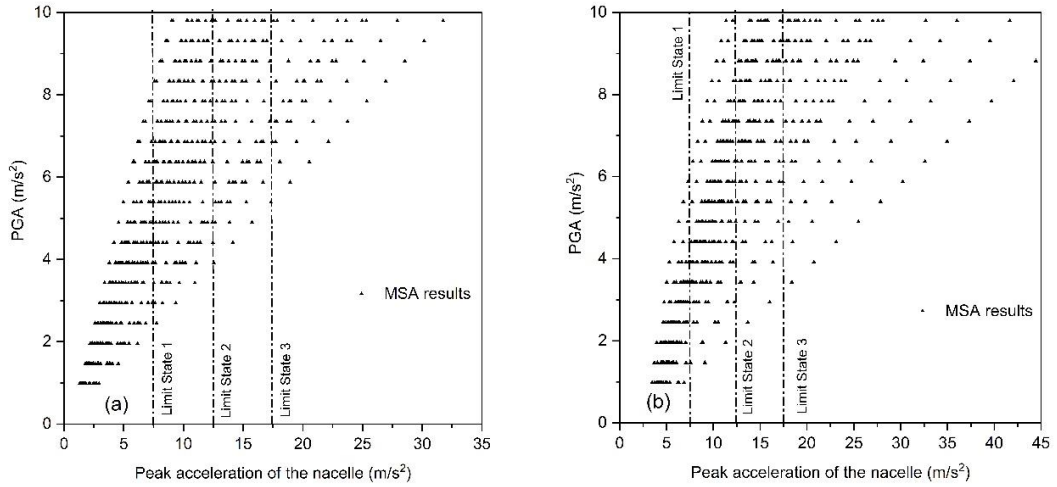

Figure 5.17 MSA analysis results for the uncontrolled offshore wind turbine (a) operational (b) parked

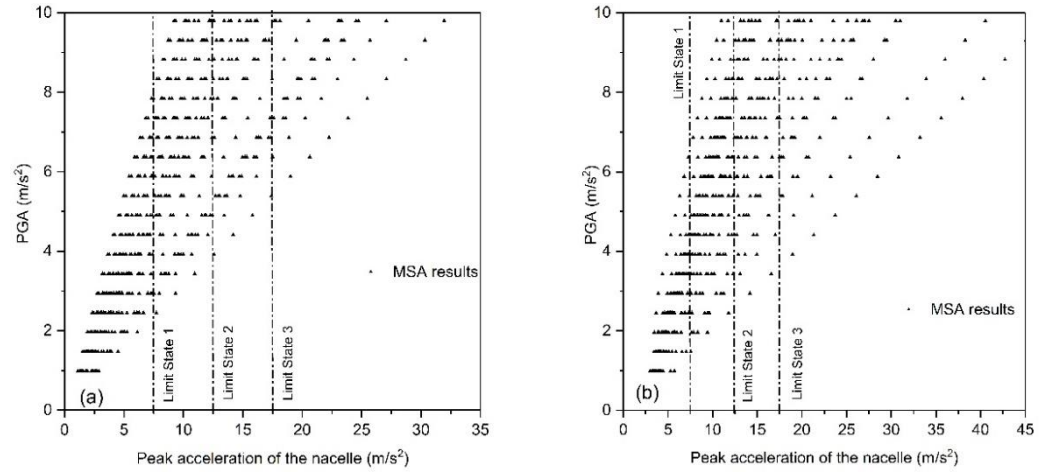

Figure 5.18 MSA analysis results for the controlled offshore wind turbine (a) operational (b) parked

Using the results illustrated in Fig. (5.17 and 5.18), the fragility curves should be established. The method used in constructing fragility curves is Maximum Likelihood approach. If we assume that our observation of failure or no-failure for a given ground motion is independent of that of other ground motions, the probability of observing z_j

failures out of n_j ground motion records at the intensity level of $IM = x_j$ can be defined as binominal distribution as

$$P(z_j \text{ failures under } n_j \text{ ground motions}) = \binom{n_j}{z_j} p_j^{z_j} (1-p_j)^{n_j - z_j} \tag{5.4}$$

in which p_j is the probability that a ground motion record with the intensity level of $IM = x_j$ causes the demand exceeds the capacity. The crucial part of the MSA method is to find a fragility function that predicts p_j with the highest probability of the observed data obtained from the nonlinear structural analysis. This step is named as the maximum likelihood approach in which the likelihood is defined as the product of binomial probabilities obtained from Eq. (5.4) at each intensity level as

$$\text{Likelihood} = \prod_{j=1}^{m} \binom{n_j}{z_j} p_j^{z_j} (1-p_j)^{n_j - z_j} \tag{5.5}$$

where $\prod$ denotes a product, and m is the number of intensity measure *IM* levels. By substituting Eq. (5.3) into the above equation, the likelihood function can be defined using fragility function parameters as

$$\text{Likelihood} = \prod_{j=1}^{m} \binom{n_j}{z_j} \Phi\left(\frac{\ln(x_j/\theta)}{\beta}\right)^{z_j} \left(1-\Phi\left(\frac{\ln(x_j/\theta)}{\beta}\right)\right)^{n_j - z_j} \tag{5.6}$$

Then the most accurate fragility function parameters can be calculated by maximizing the likelihood function in an optimization solver in MATLAB. Since it is easier to use the logarithm of the likelihood function in our solver, the final maximization equation can be defined as

$$\left\{\hat{\theta}, \hat{\beta}\right\} = \arg\max_{\theta,\beta} \sum_{j=1}^{m} \left\{ \ln\binom{n_j}{z_j} + z_j \ln\Phi\left(\frac{\ln(x_j/\theta)}{\beta}\right) + \left(n_j - z_j\right) \ln\left(1-\Phi\left(\frac{\ln(x_j/\theta)}{\beta}\right)\right) \right\} \tag{5.7}$$

The fragility function curves obtained from the estimated fragility parameters using Maximum Likelihood approach is plotted in Fig. 5.19-24 for different limit states under the operational and parked conditions. The fraction of analyses causing failure to a total

number of analyses is plotted as well. The higher the value of Likelihood function calculated from Eq. (5.6), the closer the fragility curve to the points in the following plots.

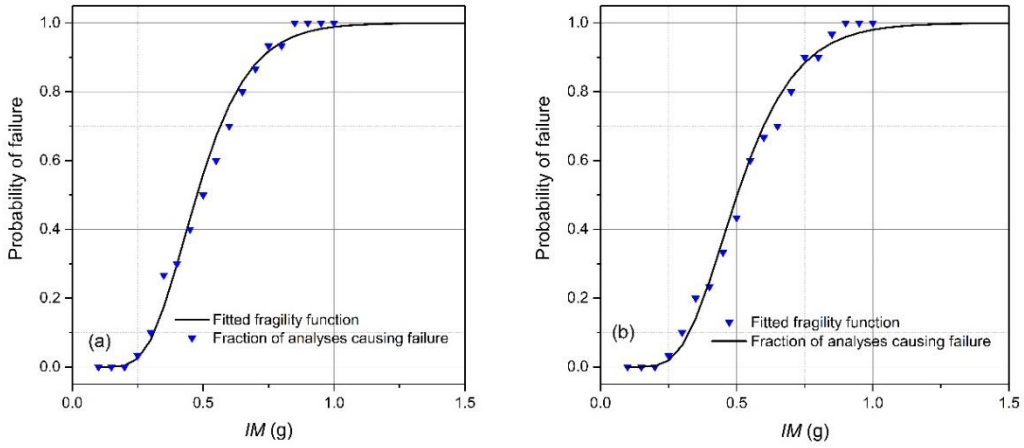

Figure 5.19 Fragility curved obtained from the estimated fragility curve parameters based on Likelihood approach versus observed fractions of failures for operational loading for limit state 1 (a) uncontrolled (b) controlled

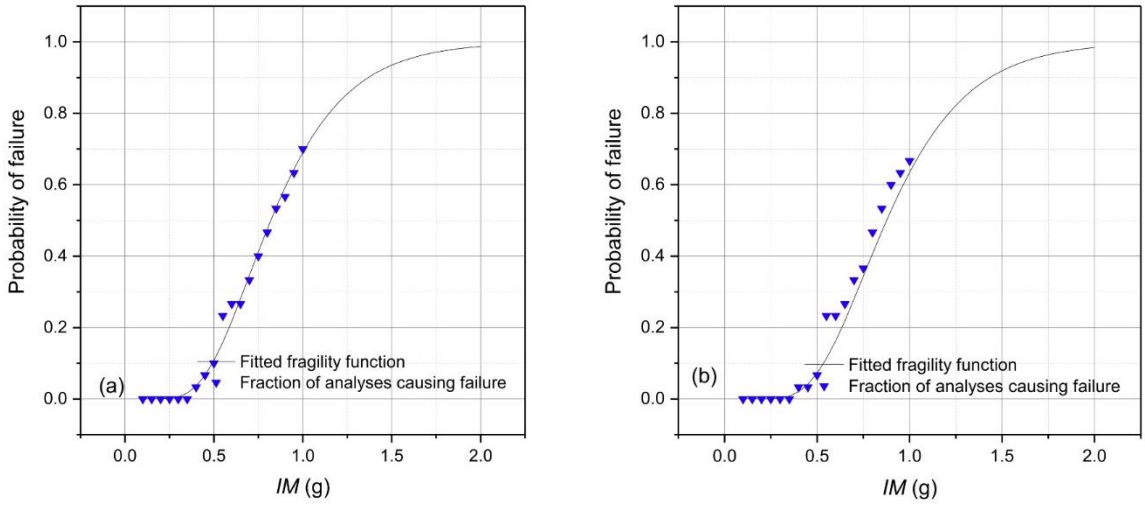

Figure 5.20 Fragility curved obtained from the estimated fragility curve parameters based on Likelihood approach versus observed fractions of failures for operational loading for limit state 2 (a) uncontrolled (b) controlled

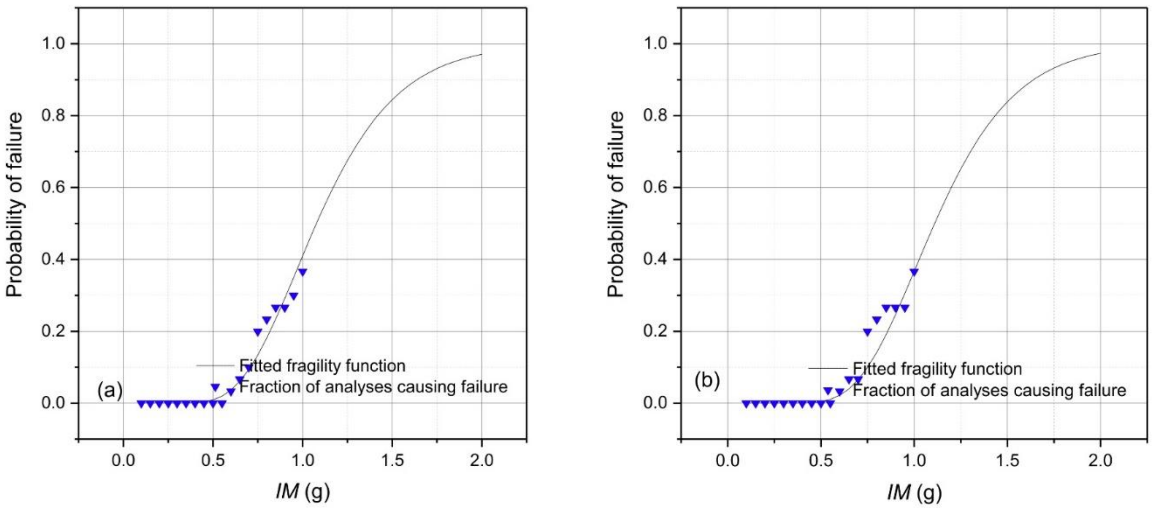

Figure 5.21 Fragility curved obtained from the estimated fragility curve parameters based on Likelihood approach versus observed fractions of failures for operational loading for limit state 3 (a) uncontrolled (b) controlled

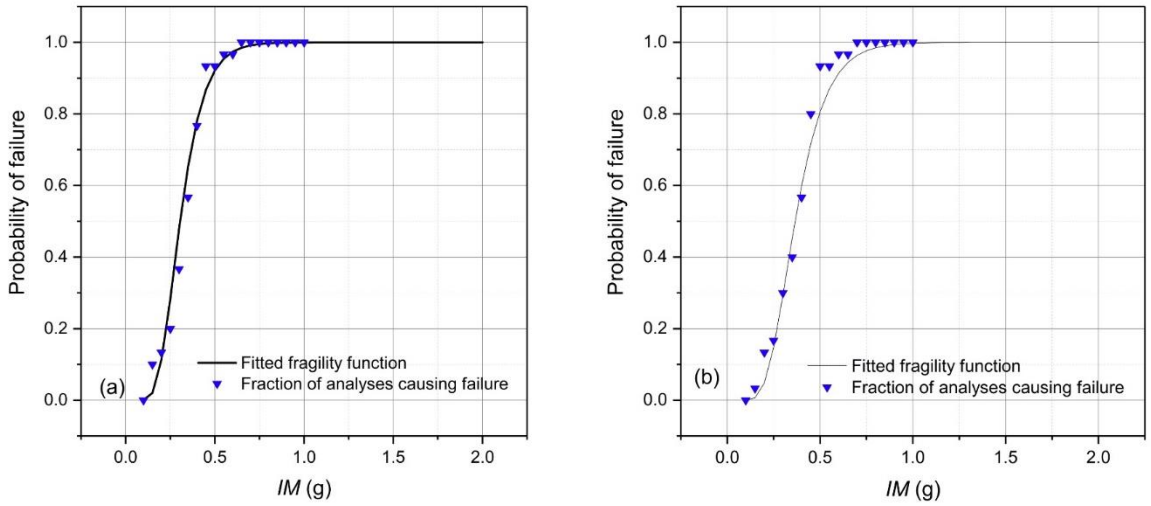

Figure 5.22 Fragility curved obtained from the estimated fragility curve parameters based on Likelihood approach versus observed fractions of failures for parked condition for limit state 1 (a) uncontrolled (b) controlled

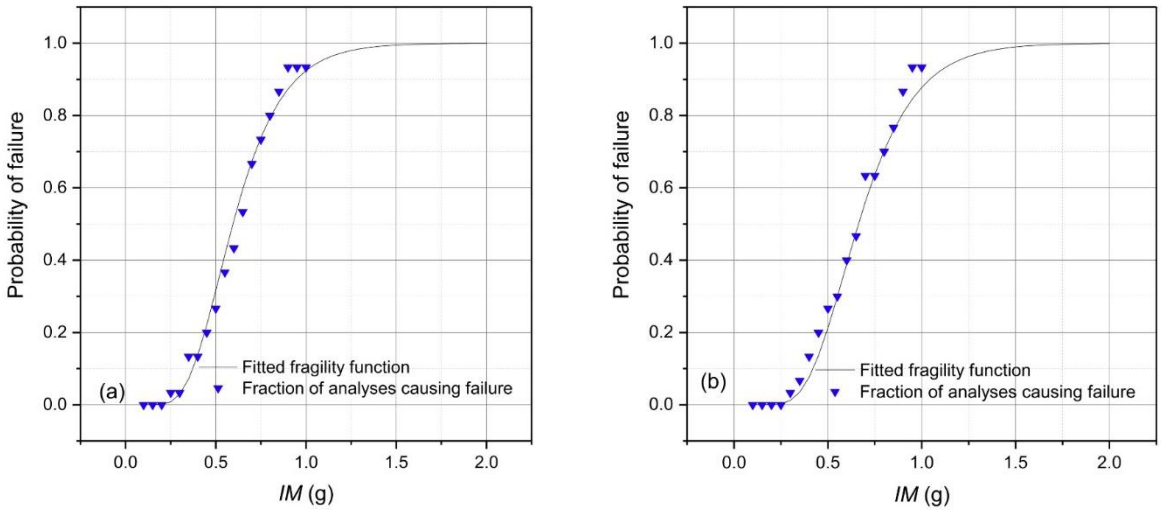

Figure 5.23 Fragility curved obtained from the estimated fragility curve parameters based on Likelihood approach versus observed fractions of failures for parked condition for limit state 2 (a) uncontrolled (b) controlled

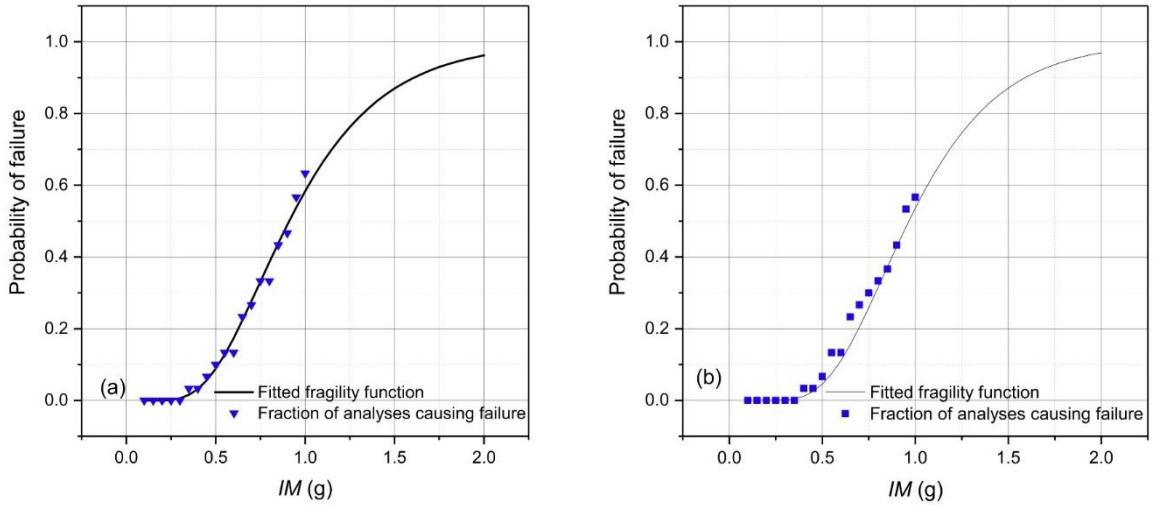

Figure 5.24 Fragility curved obtained from the estimated fragility curve parameters based on Likelihood approach versus observed fractions of failures for parked condition for limit state 3 (a) uncontrolled (b) controlled

Fig 5.25 shows fragility curves for the controlled and uncontrolled offshore wind turbines for three limit states under the operational and parked conditions. The solid lines correspond to the uncontrolled system in which there is no vibration control system and the dot lines correspond to the fragility curves of the controlled system. At the first glance, it is apparent that the fragility values for the parked condition at a given intensity measure are much higher than the corresponding fragility values for operational

condition and this difference is more pronounced in lower intensity measures. Since lower intensity measures are more probable to occur, the reliability of equipment inside the nacelle is much lower in the parked conditions at lower intensity measures. For instance, the fragility of the uncontrolled system at 0.5g intensity measure for the limit state 1 under the operational condition is 56%, whereas the corresponding fragility value for the parked condition is 90%, nearly 60% reduction in reliability. For limit state 2, the fragility of the uncontrolled system under operational loading at 0.5g intensity measure is 11%, however, the corresponding value for the parked condition is 31%, nearly tripled. This highlights the importance of a structural control device especially for the parked condition in which the lack of aerodynamic damping causes larger excessive vibrations, consequently lower reliability.

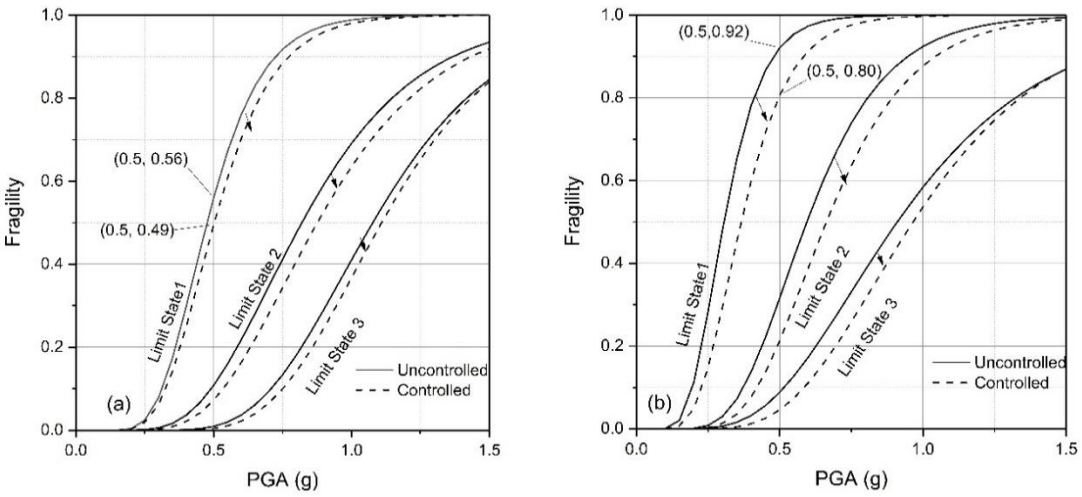

Figure 5.25 Reduction in fragility using the optimal TLCD for three limit states (a) operational (b) parked

Looking into the effect of the structural control device, it is clear that there is a shift to lower fragility values when the system is controlled with the optimal TLCD. For instance, the fragility of exceeding acceleration capacity of 0.5g for the operational condition is reduced from 56% to 49%, representing 7% decrease in fragility values. This fragility reduction is approximately doubled for the parked condition in which fragility is reduced from 92% to 80%, resulting in 12% reduction in fragility. Table 15 provides the fragility values and fragility reduction gained from the optimal TLCD for the predefined limit states under two loading conditions. The maximum fragility

reduction obtained from the tuned liquid column damper for operational load case is 9%, however, the corresponding maximum fragility reduction for the parked condition is 15%. This is expected because total damping of the system for the parked condition is low due to the lack of aerodynamic damping and a structural control device can compensate for this low damping value and boost the reliability of the system. The inclusion of an optimal tuned liquid column damper in the system reduces the overall fragility of the equipment, resulting in an increase in reliability of the system. This increases the energy conversion by reducing the number of interruptions and emergency shutdowns and consequently decreasing the number of maintenances required after the emergency shutdowns.

Table 5.3 Fragility values corresponding to three intensity measures for three limit states for wind turbines with and without TLCDs

		Operational Condition (LC1)			Parked Condition (LC2)		
		Intensity Measures (m/s^2)					
Limit States	Fragility	$IM = 0.5g$	$IM = 0.75g$	$IM = g$	$IM = 0.5g$	$IM = 0.75g$	$IM = g$
Limit State 1 ($LS = 7.5m/s^2$)	$P_{Uncontrolled}$	56%	91%	98%	93%	99%	100%
	$P_{Controlled}$	49%	88%	97%	80%	97%	99%
	$P_{reduction}$	***7%***	*3%*	*1%*	*13%*	*2%*	*1%*
Limit State 2 ($LS = 12.5m/s^2$)	$P_{Uncontrolled}$	11%	41%	69%	31%	74%	92%
	$P_{Controlled}$	7%	34%	63%	21%	61%	87%
	$P_{reduction}$	*4%*	*7%*	*6%*	*10%*	***13%***	*5%*
Limit State 3 ($LS = 17.5m/s^2$)	$P_{Uncontrolled}$	1%	13%	41%	9%	33%	58%
	$P_{Controlled}$	0%	9%	36%	4%	25%	53%
	$P_{reduction}$	*1%*	*4%*	*5%*	*5%*	*8%*	*5%*

5.6 Conclusion

In this section, a numerical model of NREL baseline offshore wind turbine controlled by optimal tuned mass liquid dampers (TLCDs) subjected to wind, wave, and earthquake excitations are established. The developed MATLAB code uses a nonlinear dynamic solution to consider the nonlinearities of TLCDs as well as soil-pile interaction. Numerical analyses are carried out for operational and non-operational loading in conjunction with seismic excitation to investigate the effectiveness of TLCD in reducing dynamic responses of multi-hazard conditions. The results show that the optimal TLCDs reduce the standard deviation of deflections of the top of tower up to 49%. It is found that the TLCDs show a better performance in mitigating undesired vibrations caused by low-intensity earthquakes rather than very high-intensity earthquakes.

With regard to fragility analysis, three limit state thresholds corresponding to high, medium and low sensitive equipment are defined. Multiple stripes analysis approach is utilized to construct empirical cumulative distribution. Having used the Likelihood Maximization approach, the fragility function curves are obtained for the predefined limit states. The fragility values decrease with the inclusion of the tuned liquid column damper for all cases, resulting in a boost in the reliability of the system under multi-hazard conditions. However, this fragility reduction varies for different limit states and intensity measures. The maximum fragility reduction is observed for medium and high sensitive equipment up to 13%. The corresponding values for low sensitive equipment are lower. Furthermore, the results show that the fragility reduction offered by the tuned liquid column dampers is higher for low-intensity earthquakes. In addition, the corresponding values for the parked condition are larger due to the lack of aerodynamic damping in this condition. Therefore, implementation of an optimal TLCD can increase the overall reliability of the system, especially for parked conditions under low-intensity earthquake motions. Consequently, it reduces downtime and maintenance needs resulting in higher rates of energy conversion. Future research efforts can be focused on assessment of reliability improvement offered by more optimized structural control devices including semi-active and active dampers.

Chapter 6 Semi-Active Vibration Control of Offshore Wind Turbines

6.1 Introduction

High flexibility of new offshore wind turbines (OWT) makes them vulnerable since they are subjected to large environmental loadings, wind turbine excitations and seismic loadings. A control system capable of mitigating undesired vibrations with the potential of modifying its structural properties depending on time-variant loadings and damage development can effectively enhance serviceability and fatigue lifetime of turbine systems. In this section, a model for offshore wind turbine systems equipped with a semi-active time-variant tuned mass damper is developed considering nonlinear soil–pile interaction phenomenon and time-variant damage conditions. The adaptive concept of this tuned mass damper assumes slow change in its structural properties. Stochastic wind and wave loadings in conjunction with ground motions are applied to the system. Damages to soil and tower caused by earthquake strokes are considered and the semi-active control device is retuned to the instantaneous frequency of the system using short-time Fourier transformation (STFT). The performance of semi-active time-variant vibration control is compared with its passive counterpart in operational and parked conditions. The dynamic responses for a single seismic record and a set of seismic records are presented. The results show that a semi-active mass damper with a mass ratio of 1% performs significantly better than a passive tuned mass damper with a mass ratio of 4%.

6.2 Motivation

The semi-active control mechanism is more suitable for the systems with high time-variant parameters such as offshore wind turbines. Semi-active vibration control devices for the application of buildings have been actively studied by a number of researchers [3, 96-100] in the last few decades. However, their application in wind energy is a new field. One of the earliest studies on semi-active control mechanism for wind turbines was done by Kirkegaard et al. [101], in which they presented an experimental and numerical investigation of semi-active vibration control of offshore wind turbines equipped with a magnetorheological (MR) fluid damper. The authors

claimed that using MR dampers for offshore wind turbines results in considerable reduction of the lateral displacement compared to the uncontrolled system. Later on, Karimi et al. [37] proposed a controllable valve in tuned liquid column dampers for the application of offshore wind turbines. In addition, the use of semi-active tuned mass dampers in control of flapwise vibrations of wind turbines was examined by Arrigan et al. [22]. The authors proposed a frequency-tracking algorithm for retuning the vibration control device and they observed significant vibration reductions owing to the semi-active mechanism. Furthermore, Weber [102] studied application of an adaptive tuned mass damper concept based on semi-active controller using MR dampers. Their results showed that the real-time controlled MR semi-active tuned mass damper is a robust device for reducing structural vibrations. Semi-active control mechanism for tuned liquid column dampers (TLCDs) was also studied by Sonmez et al. [38]. The authors used a control algorithm based on short-time Fourier transformation (STFT) and investigated the effectiveness of the proposed device under random excitations. More recently, Sun [25] explored semi-active tuned mass dampers for the NREL (National Renewable Energy Laboratory) 5 MW baseline wind turbine excited by environmental loadings in conjunction with seismic motions considering post-earthquake damage to soil and tower stiffnesses. The author demonstrated the superiority of semi-active vibration control over the passive one in multi-hazard conditions. Although Sun's [25] work is well founded, it is limited to only one earthquake record (1994 Northridge Newhall 90) and further study for a suite of earthquake records with different frequency contents and intensities is required. Another limitation of the aforementioned work is that soil–pile interaction was modeled using a simplified method (closed-form solution) in which the stiffness of embedded pile is considered with a constant rotation and lateral stiffness value in seabed level. More advanced soil–pile interaction model based on time-variant nonlinear stiffness considering soil damage phenomena can enhance the previous works. In addition, the effect of semi-active tuned mass dampers on other structural responses such as base shear and base moment should be investigated.

To fill this gap, this study investigates semi-active tuned mass dampers for offshore wind turbines under multi-hazard conditions considering time-variant nonlinear soil–pile interaction properties and time-variant damage. A detailed model of the modern NREL 5 MW wind turbine equipped with semi-active tuned mass dampers (STMD) is developed. Stochastically wave and wind loadings in conjunction with seismic

loadings are applied to the system and dynamic responses such as displacement, base shear, and base moments are investigated. Compared to the previous models, the developed model has the capacity to consider soil–pile interactions more realistically. Furthermore, a suite of seismic records is used with the aim to consider a wider range of seismic characteristics in the simulations.

6.3 Model Description of Semi-Active Vibration Control Algorithm

There are three main parameters that define a tuned mass damper: mass, stiffness, and damping. Mass of vibration control device cannot be changed in time domain due to practical reasons and only stiffness and damping of the device are altered in time domain depending on instantaneously structural properties of the system and instant dynamic responses. There have been studies on algorithms for time-variant properties of semi-active tuned mass dampers by [22, 38, 98, 100]. In most of the previous studies, the stiffness of semi-active TMD is tuned according to instantaneously identified frequency using short-time Fourier transform and the damping parameters are modulated based on the TMD deflection in each time step.

6.3.1. Varying Stiffness

Stiffness of the semi-active tuned mass damper can be modified based on the identified dominant frequency using short-time Fourier transformation (STFT) function as suggested in the previous studies such as [25, 45, 102]. Unlike the standard Fourier transform, short-time Fourier transformation adds a time dimension to the base function parameters. A signal $x(\tau)$ is multiplied by a moving window function as $h(\tau - t)$:

$$\hat{x}(\tau) = x(\tau)h(\tau - t) \tag{6.1}$$

in which $\hat{x}(\tau)$ is a weighted signal, τ is the moving time and t is the fixed time.

The spectrum $S(t,\omega)$ at the fixed time can be defined by applying Fourier transform to $\hat{x}(\tau)$:

$$S(t,\omega) = \frac{1}{2\pi}\int e^{-j\omega t}\hat{x} = \frac{1}{2\pi}\int e^{-j\omega t}x(\tau)h(\tau - t) \tag{6.2}$$

and the power spectral density $P(t,\omega)$ of time *t* is calculated as

$$P(t,\omega) = \left|S(t,\omega)\right|^2 = S(t,\omega).\overline{S(t,\omega)} \tag{6.3}$$

Then, the dominant frequency at time *t* can be identified using following equations:

$$\omega_{inst} = \left\{\omega \middle| P(t_i,\omega) = \max\left\{P(t_i,\omega)\right\}\right\} \tag{6.4}$$

$$\omega_{id} = \frac{\sum_{k=\max\{1,i-m+1\}}^{i} \omega_{inst}(t_k)\max\left\{P(t_k,\omega)\right\}}{\sum_{k=\max\{1,i-m+1\}}^{i} \max\left\{P(t_k,\omega)\right\}} \tag{6.5}$$

where ω_{id} is the dominant frequency at time t_i determined through finding the average of instantaneous frequencies over *m* time steps ($m=3$) , and ω_{inst} is the instantaneous frequency. In this study, a moving window of 500 time steps ($n=500$) with a Hamming window is used. The length of the hamming window is taken 1024, L, resulting in the vector of P_i with the size of $N\times 1$, where $N=(0.5*L)+1$. The dominant frequency at each time step is calculated and then stiffness of the tuned mass is retuned using the dominant frequency as

$$k_d^t = k_d^{t=0}\left(\frac{\omega_{id}}{\omega_n}\right)^2 \tag{6.6}$$

in which k_d^t is the time-variant stiffness of tuned mass damper that can be realized through a variable stiffness device, $k_d^{t=0}$ is the initial stiffness of tuned mass damper at the time of zero, and ω_n is the predamage fundamental frequency of the system in which the TMD was tuned to before the development of any damages.

6.3.2. Varying Damping

The damping of tuned mass dampers can be altered according to the dynamic responses in order to increase the effectiveness of the device. In the previous studies by Abe and Igusa [103], the authors investigated the time-variant damping for tuned mass dampers and concluded that TMD can improve its performance if the damping of TMD is time-dependent in such a way that its damping value changes to zero for the duration in which the relative displacement of TMD is increasing. This results in an increase in the efficiency of the system for controlling excessive vibrations. This

time-dependent damping algorithm has been used in other works [25, 100, 104]. In this method, the relative displacement of TMD is tracked in each time step and if it is larger than that of the previous time step, the damping of TMD is set to zero , $c_d^{\,t} = 0$; otherwise the damping value is set to $2c_{opt}$, $c_d^{\,t} = 2c_{opt}$. c_{opt} is the optimal value of TMD's damping which can be determined from an estimation method suggested by Sadek et al. [105].

6.3.3 Damage Development

Dynamic performance of passive tuned mass dampers is threatened by changes in the natural frequency of the system. This change in the natural frequency can occur either gradually over the lifetime of the system due to soil degradation under long-term cyclic loading or rapidly over a short period of time due to seismic excitation. Figure 6.1a shows the effect of soil stiffness changes (damage or stiffening in soil) on the first and second natural frequency of the system. The figure shows that a 50% reduction in soil stiffness leads to 2.2%, and 4.8% reduction in the first and second natural frequencies of the system, respectively. The figure indicates that the second natural frequency changes more and degradation of soil stiffness has a larger effect on the frequency change rather than stiffening of soil. Similarly, the frequency change of the system due to tower damage is shown in Figure 6.1b. The figure suggests that tower damage reduces the natural frequency to a greater extent. For example, 20% stiffness reduction of tower leads to 5.9% decrease in the first natural frequency of the system.

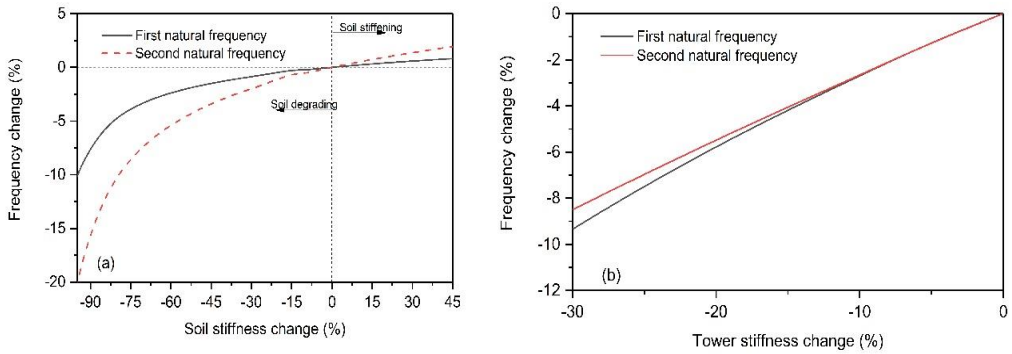

Figure 6.1 Frequency change due to (a) soil degrading/stiffening, (b) tower stiffness reduction

The degradation stiffness model of monopile foundations under long-term cyclic loading was studied by Martin Achmus et al. [46]. Sun also considered soil and tower stiffness damage development for seismic loading using simplified linear stiffness reduction scenarios [29]. In this study, a rapid degradation stiffness model is assumed as the focus of the study is on the short-term damage development due to seismic excitation. Therefore, the damage development model similar to Sun [29] is assumed with the values in which a 5% reduction in natural frequency occurs. To model damage development, it is assumed that damage begins developing at the start of earthquake and soil stiffness and tower stiffness reduce linearly in 20 s as depicted in Figure 6.2 Tower stiffness and tower stiffness are assumed to reduce 30% and 15%, respectively. The reduction in the stiffness of the tower is assumed in the whole tower.

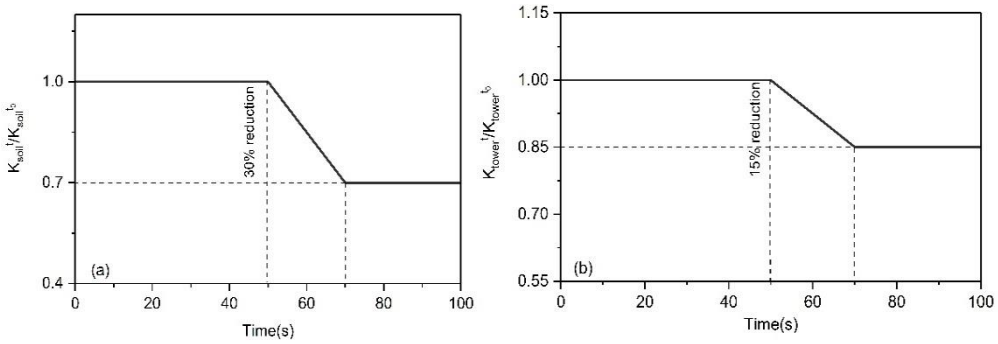

Figure 6.2 Damage development: (a) soil stiffness, (b) tower stiffness

6.4. Numerical Results

6.4.1 Response to a Single Seismic Record

To give a preliminary insight into the dynamic responses of offshore wind turbines equipped with semi-active and passive tuned mass dampers considering frequency change as a result of damage development, the responses to a single seismic record for different loading conditions are discussed in this section. Four loading conditions are adopted according to IEC (International Electrotechnical Commission) standards [47] and their properties are tabulated in Table 6.1. In the first loading condition scenario (LC1), the turbine is operating under steady wind loading at the rated wind speed. In the second loading condition (LC2), the parked turbine is subjected to a steady wind speed of 40 m/s. For both of these loading conditions, there is no wave loading which

represents calm sea conditions. Loading conditions LC3 and LC4 are the same as LC1 and LC2 but with stochastic wind and wave loadings. For all these loading conditions, the seismic event in conjunction with damage development occurs at the instant of 50 s.

Table 6.1 Loading condition (LC) information.

	Wind		Wave		Seismic	
Loadcases	**Wind Speed at the Hub Height (m/s)**	**Turbulence Intensity (%)**	**Wave Period (sec)**	**Significant Wave Height (m)**	**Starting Instant**	**Damping**
LC1	11.4 (Operational)	0	-	-	50 s	1%
LC2	40.0 (Parked)	0	-	-	50 s	5%
LC3	11.4 (Operational)	14.5	9.5	5.0	50 s	1%
LC4	40.0 (Parked)	11.7	11.5	7.0	50 s	5%

The identified dominant frequency according to short-time Fourier transport function is calculated in each time step and the stiffness of semi-active tuned mass damper is retuned according to Equation 6.6. The dynamic responses of the offshore wind turbine subjected to a single seismic record (Kobe) are discussed here. In the following section, baseline denotes uncontrolled system. For the controlled systems, PTMD and STMD denote passive TMD and semi-active TMD, respectively. The parameters of the tuned mass dampers used in this section are tabulated in Table 6.2. Figure 6.3 compares the nacelle displacement responses of the turbine under steady wind loadings. At first glance, it is clear that for LC1 and LC2, STMD is superior to PTMD. In Figure 6.3a, the peak of nacelle displacement decreased from 0.96 m to 0.91 m for operational loading LC1 and the dynamic response of PTMD is nearly as much as the baseline system especially after the end of earthquake and damage development. This shows that the PTMD becomes off-tuned and unable to control the vibration. However, STMD can retune to the new frequency and mitigate the dynamic responses. The displacement reductions are more pronounced for the parked condition (LC2) in which the peak of nacelle displacement for STMD is 0.19 m compared to 0.26 m of the passive tuned mass damper, nearly 16% more reductions compared to the baseline system.

Table 6.2 TMD parameters.

Mass (kg)	k_d **(N/m)**	c_d **(N/(m/s))**	ω_d **(Hz)**
20,000	41,657	10,000	0.229

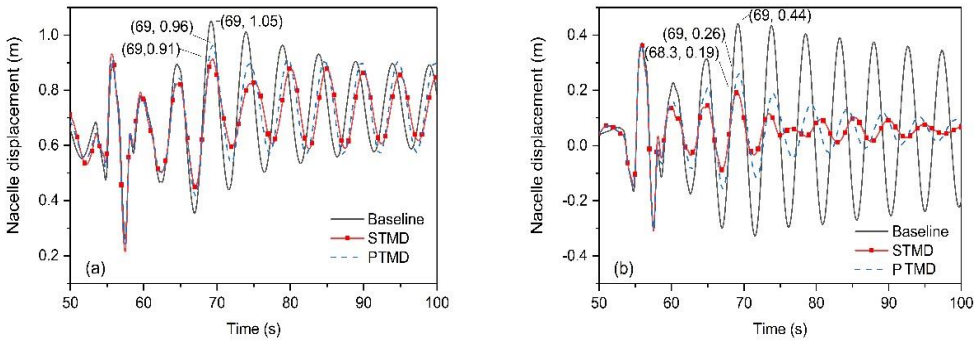

Figure 6.3 Time history of nacelle displacement under steady wind loading and seismic excitation considering damage development. (a) LC1, (b) LC2. PTMD: passive tuned mass damper.

To scrutinize the energy spectrum of dynamic responses, the power spectral density (PSD) of the nacelle displacements for LC1 and LC2 is obtained and presented in Figure 6.4. Fast Fourier transformation based on Hamming window is used to capture a smooth PSD curve. Figure 6.4a indicates that there are two distinct peaks corresponding to the energy of wind loading and turbine frequency (1P) whose frequencies are around zero and 0.2 Hz, respectively. It is clear that the PSD for energy from wind loading (frequencies close to zero) shows negligible changes for PTMD and STMD as these devices are tuned to the first natural frequency of the system. However, a 37% reduction in the peak of the power spectrum for the STMD system can be observed for the turbine frequency (1P). Similarly, power spectral density of the nacelle displacement for LC2 (parked condition) is shown in Figure 6.4b. Compared to the operational condition (Figure 6.4a), energy spectrum corresponding to frequency of wind loading (close to zero) has much lower peak due to the fact that in parked condition the turbine absorbs a small portion of wind loading as a result of pitching mechanism in the blades and the energy is concentrated around the frequency range of first natural frequency of structure. This is expected because in the parked condition the vibration of structural modes dominates compared to the operational condition where the vibration due to external excitations dominates. The figure also indicates that the peak of spectrum for the STMD system is reduced as much as 92% compared to the baseline system (uncontrolled system). However, this percentage reduction is lower for the PTMD with 76% reduction. These reductions for both PTMD and STMD are higher in the parked condition (Figure 6.4b) compared to the

operational condition (Figure 6.4a) because in the parked conditions the aerodynamic damping is negligible and these structural control devices compensate for low total damping value of the system.

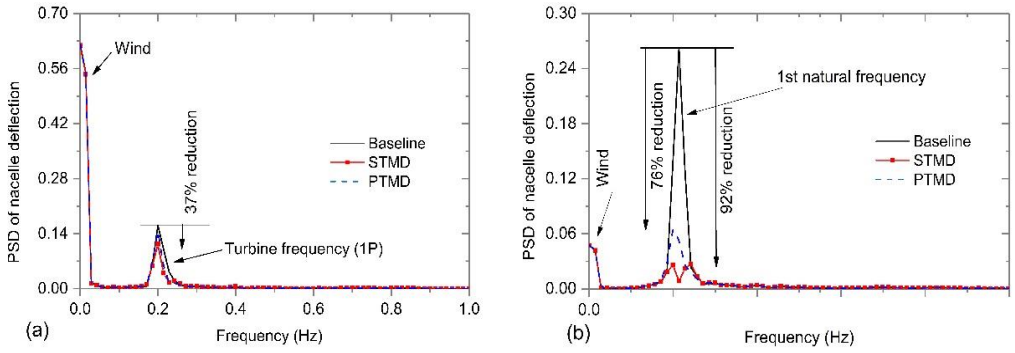

Figure 6.4 Power spectral density (PSD) of nacelle displacement under steady wind loading and seismic excitation considering damage development. (a) LC1, (b) LC2

Figure 6.5 compares the nacelle displacement responses of the turbine under stochastic wave–wave loadings in conjunction with seismic ground motion and damage development (LC3 and LC4). Again it can be seen that the STMD system shows a better performance in mitigating vibrations and reducing peak displacements. For example, the peak value of displacement is decreased from 1.5 m of the baseline system to 1.27 m of the STMD system for the operational condition (LC3), with 15% reduction. This reduction percentage for the PTMD system is lower, as much as only 6%. Therefore, the STMD's effectiveness in reducing the peak values is more than twice that of the PTMD. For the parked condition (LC4), higher vibration reductions are observed. For example, the peak nacelle displacement reduced from 1.91 m to 1.01 m as a result of the implementation of the semi-active tuned mass damper. This means that the semi-active achieves 47% reduction in the peak nacelle displacement.

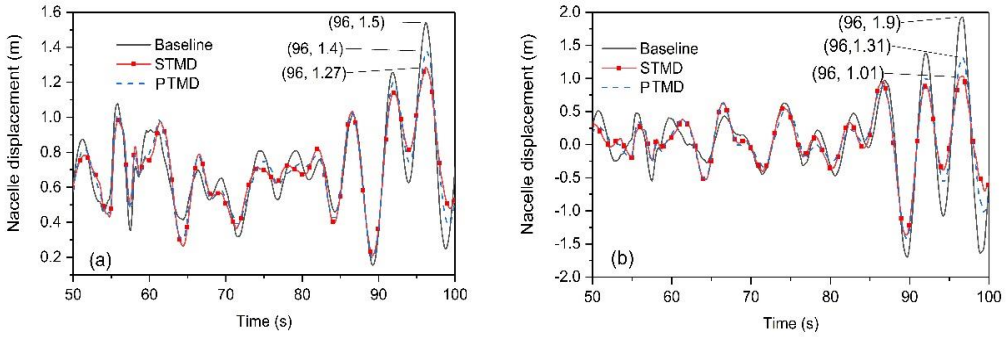

Figure 6.5 Time history of nacelle displacement under stochastic wind–wave loadings and seismic excitation considering damage development. (a) LC3, (b) LC4.

Looking into power spectral density of the nacelle displacement for LC3 and LC4 in Figure 6.6, some energy is concentrated around the frequency of 0.1 Hz that corresponds to the energy of wave loadings. Similar to Figure 6.4, more PSD reduction is observed for parked condition (LC4). However, the difference between the reduction in PSD for PTMD and STMD is less than 10%.

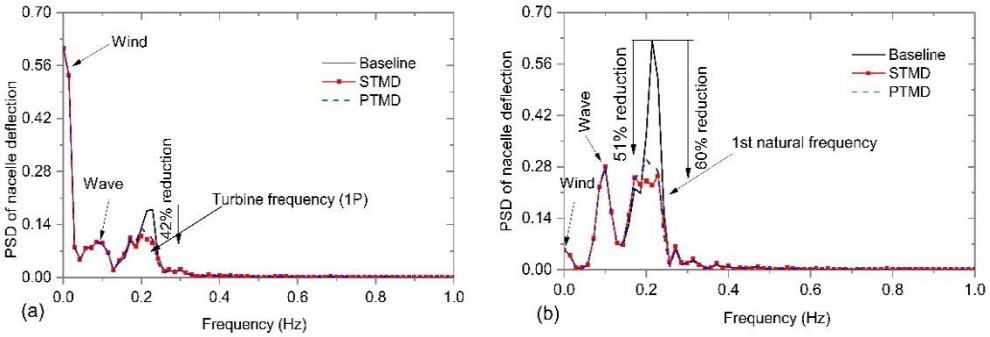

Figure 6.6 PSD of nacelle displacement under stochastic wind–wave loadings and seismic excitations considering damage development. (a) LC3, (b) LC4

Figures 6.7 and 6.8 show a representative 50 s window time history of the base shear force for steady (LC1 and LC2) and stochastic loadings (LC3 and LC4), respectively. For steady wind loadings (LC1 and LC2), larger base shear is obtained during ground motion and both passive and semi-active TMDs have slight effects on the dynamic responses during the ground motion and damage development. However, the displacements after the damage development are reduced owing to the vibration

control devices. For both load cases, STMD is superior to the PTMD. On the other hand, for stochastic loading (Figure 6.8), changes in the base shear due to tuned mass dampers are insignificant.

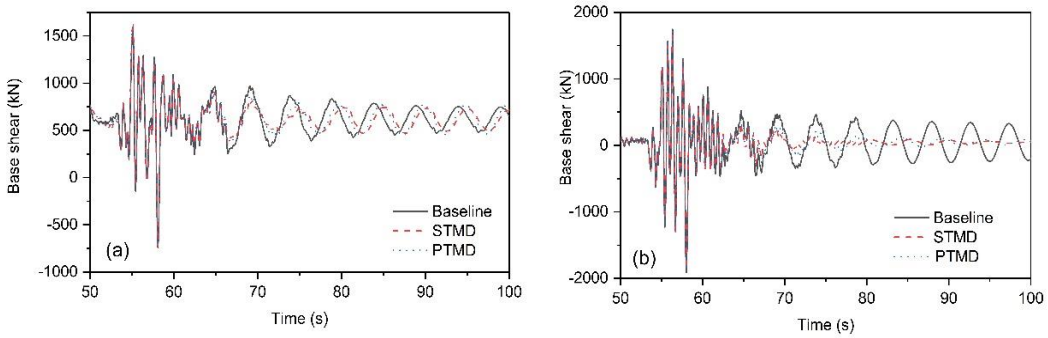

Figure 6.7 Time history of fore–aft base shear force under only steady wind loading and seismic excitation considering damage development. (a) LC1, (b) LC2

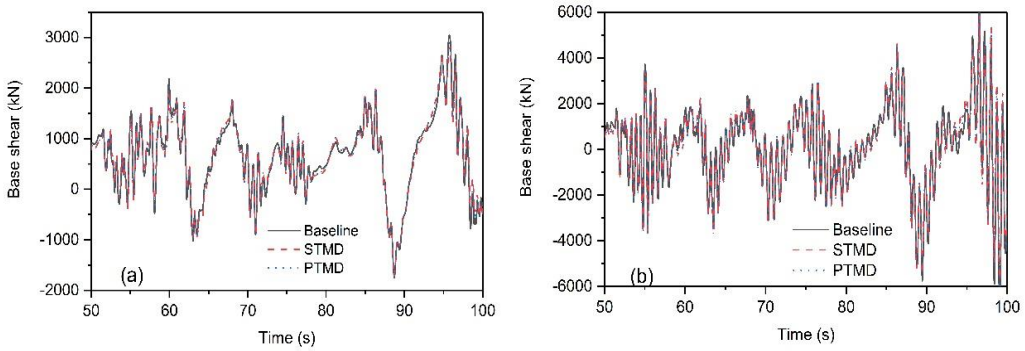

Figure 6.8 Time history of fore–aft base shear force under stochastic wind–wave loadings and seismic excitations considering damage development. (a) LC3, (b) LC4.

Figures 6.9 and 6.10 compare the base overturning moment time histories for the controlled and uncontrolled systems. Figure 6.9 shows that the vibration control devices mitigate the base moment values after the development of damage for steady loading. For load case (LC1), the peak values of the base moment, which occur at 69 s, reduce 10% and 15% when PTMD and STMD are used, respectively. This reduction is higher for the parked condition (LC2), where PTMD and STMD reduce the base moment values up to 43% and 57%, respectively. For stochastic loading (Figure 6.10),

the effect of the vibration control devices is less significant for this single seismic motion record.

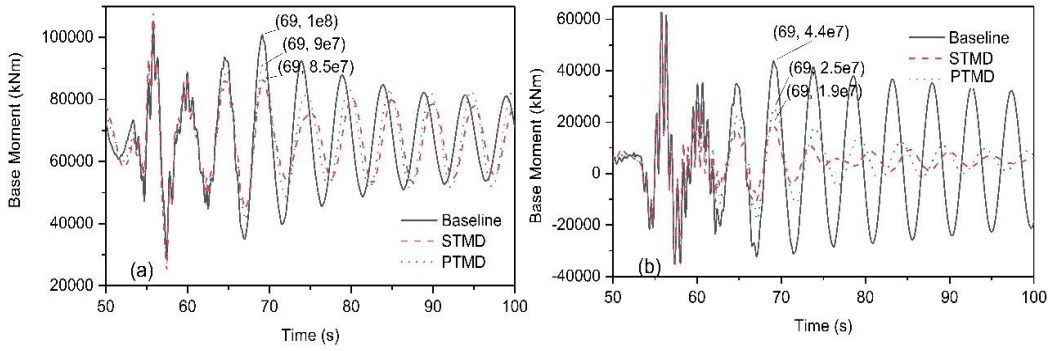

Figure 6.9 Time history of the fore–aft base moment under only steady wind loading and seismic excitation considering damage development. (a) LC1, (b) LC2

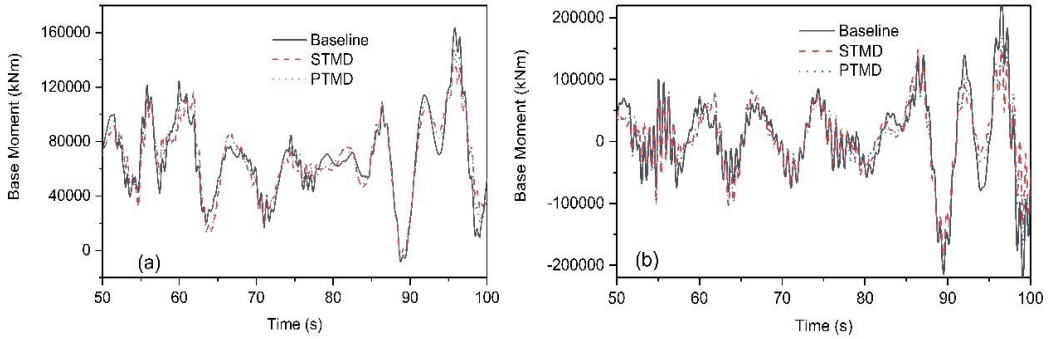

Figure 6.10 Time history of the fore–aft base moment under stochastic wind–wave loadings and seismic considering damage development. (a) LC3, (b) LC4

It should be noted that the semi-active tuned mass damper used in this study has both varying stiffness and damping and the combined effect of them is shown in the results. Individual effects of them were also investigated to determine the contribution of each in the response reduction and the results showed that the contribution of each effect individually varies depending on the load cases. However, for all load cases, the contribution of varying damping is larger than the contribution of varying stiffness. For example, the contribution of the varying damping in the response reduction (nacelle deflection) is 57%, whereas the corresponding contribution of varying stiffness is 43%.

6.4.2 Response to a Seismic Record Set

In this section, more analyses based on a set of ground motion records with different soil and intensity properties as listed in Table 3.8 are performed and the influences of the structural control devices on the dynamic responses are systematically investigated. Standard deviation and peak values of each time history are taken for the systems equipped with optimal PTMD and STMD with mass ratios ranging between 1% and 4% and compared with the baseline system (uncontrolled system) as the percentage of reduction (improvement). The positive values mean a reduction in the responses which can be defined as the effectiveness of the structural control device. On the other hand, negative values denote increases in the response which means that the vibration control device worsens the vibration performance. The standard deviations and peak values of fore–aft displacements of the nacelle are tracked as they are representative of serviceability and fatigue lifetime of the system, respectively. Then, these values are compared with those of the uncontrolled system (offshore wind turbine without any structural control devices) as the percentage of reduction.

$$\text{Peak Response Reduction} = \frac{Peak_{Uncontrolled} - Peak_{Controlled}}{Peak_{Uncontrolled}} \tag{6.7}$$

$$\text{Std Response Reduction} = \frac{Std_{Uncontrolled} - Std_{Controlled}}{Std_{Uncontrolled}} \tag{6.8}$$

in which Peak and Std denote peak and standard deviation of deflections, respectively. Controlled denotes the offshore wind turbine equipped with structural control devices, and Uncontrolled denotes the baseline offshore wind turbine without any vibration control devices. Figure 6.11a and Figure 6.11b illustrates the standard deviation reduction of the nacelle displacement for STMD and PTMD, respectively, for loading condition LC3. For STMD, it is clear that dynamic responses reduce as the mass ratio increases for most ground motions. However, a different trend for PTMD (Figure 6.11b) is observed in which negative performances are seen for most ground motion records and even increasing the mass ratio of TMD does not improve the performance. This behavior is expected since the passive tuned mass damper is unable to mitigate

the vibrations as it becomes off-tune by changing the frequency of the system due to damage development.

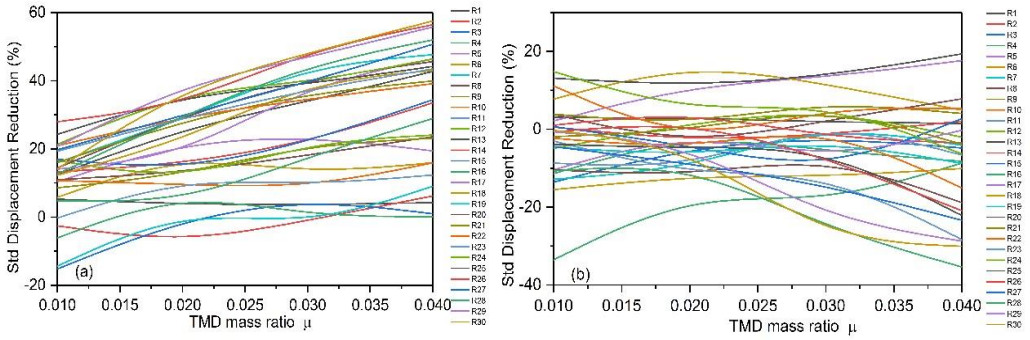

Figure 6.11 Standard deviation reduction of fore–aft displacement for LC3 under a set of seismic records. (a) STMD, (b) PTMD.

Figure 6.11 shows standard deviation reduction for all seismic records for only nacelle displacement under LC3 loading conditions. For the sake of brevity, the dynamic response reductions for all the seismic records are averaged for each loading condition and presented in Figures 6.12 and 6.13. The average of reduction percentage in the standard deviation of dynamic responses for all ground motion records for load cases LC3 and LC4 (stochastic wind and wave loading in conjunction with seismic excitation and damage development) is obtained and plotted in Figure 6.12. Dashed lines correspond to semi-active tuned mass dampers and solid lines are for passive tuned mass dampers. For the operational condition (Figure 6.12a), the standard deviation of nacelle displacements reduces by 20% for STMD with 1% mass ratio and this reduction percentage increases to 39% by increasing the mass ratio to 4%. On the other hand, the PTMD with 1% mass ratio leads to only 10% standard deviation reduction, half of its STMD counterpart. It is interesting that the performance of PTMD becomes worse when the mass ratio increases up to 4%, resulting in 10% increase in the standard deviation of deflection. This suggests that increasing the mass ratio of PTMD cannot improve its dynamic performance and even it worsens the dynamic performance due to the controller becoming off-tune as well as the reduction in the natural frequency of system as a result of the additional mass of tuned mass damper. From the results shown in Figure 6.12, it is concluded that a semi-active mass damper with a mass ratio of 1% shows much better performance than a passive tuned

mass damper with a mass ratio of 4% for the case when there is a change in natural frequency of the system. This means that STMD with a very low mass ratio is more effective than a PTMD with a large mass ratio. Similar trends can be observed for base shear force and base moment responses; however, it should be noted that base shear force and base moment experience lower dynamic response reduction with the vibration control devices. For example, the standard deviation of the base shear force shows a maximum of 7% reduction for STMD with a mass ratio of 3%. Therefore, it could be concluded that the considered structural control devices have more influence on nacelle displacement and base overturning moments rather than base shear force.

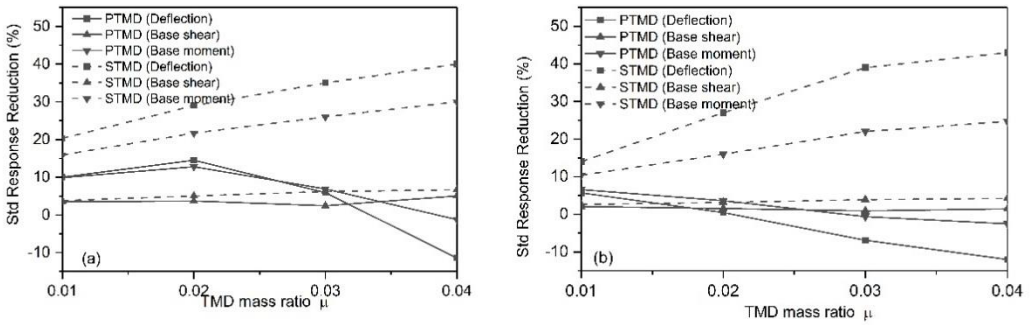

Figure 6.12 Standard deviation reduction of fore–aft displacement for stochastic wind–wave loadings and seismic excitation. (a) LC3, (b) LC4.

Similarly, the average reduction percentage in peak values of dynamic responses for all ground motion records is plotted in Figure 6.13. Similar trends to the results of standard deviations are observed with some differences. For example, for the operational loading LC3, the reduction in the peak value of the nacelle displacement is 11% for the STMD with a mass ratio of 1% and it increases to 32% with a fourfold increase in the mass ratio. It is worthy to note that the PTMD's effectiveness in mitigating the peak values of dynamic responses is very low for all the mass ratios. This means that PTMD systems have negative impacts on the peak values, resulting in a deterioration in serviceability of the system. Similar trend for LC4 can be seen in Figure 6.13b; however, the peak response reductions are higher for STMDs compared to the operational loading.

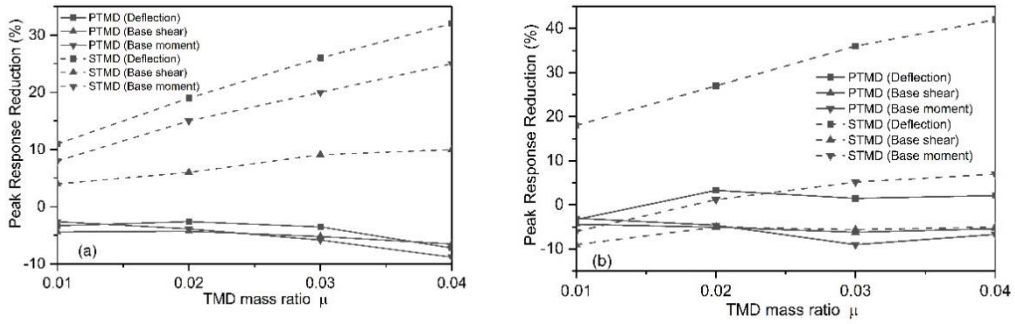

Figure 6.13 Peak response reduction of fore–aft displacement for stochastic wind–wave loadings and seismic excitation. (a) LC3, (b) LC4.

Since changes in the natural frequency of the system are inevitable due to various reasons and a number of measurement campaigns in operational wind farms have observed a difference between design natural frequency and real natural frequency, semi-active tuned mass dampers are a better option for massive tuned mass dampers. Therefore, implementation of this kind of vibration control device can mitigate undesired vibrations and reduce the dynamic response, especially the displacements and base overturning moments to a great extent. Consequently, it has the potential to reduce fatigue damages and increase the lifetime of the system, resulting in an improvement in lifecycle of wind turbines and reduction in the cost of energy production. In terms of practicality of implementation, MR dampers can be used as time-variant damping devices and variable stiffness devices can be used in order to change the stiffness of the device.

6.6 Conclusions

In this section, a numerical model for an offshore wind turbine controlled by semi-active tuned mass dampers (STMD) subjected to wind, wave, and earthquake excitations considering time-variant damage development are presented. Nonlinear soil–pile interaction is considered. Short-time Fourier transform (STFT) is utilized to identify the changes in the natural frequency of the system and to retune the semi-active tuned mass damper. Time-variant stiffness and damping of STMD are modified in each time step according to a vibration control algorithm based on short-time Fourier transform. Numerical analyses are carried out for operational and

nonoperational conditions to investigate the performance of STMD compared to the PTMD under multihazards. Dynamic responses for a single earthquake record as well as a set of earthquake records are presented. The results show that STMDs perform significantly better than PTMDs, especially when there is a change in natural frequency of the system. A semi-active mass damper with a mass ratio of 1% shows much better performance than a passive tuned mass damper with a mass ratio of 4%. A semi-active tuned mass damper with a mass ratio of 2% can reduce the standard deviation of the displacement and base overturning moment up to 20% and 16%, respectively. However, its passive counterpart increases the dynamic responses. This significant difference between the performances of the passive and semi-active devices is for the case when the natural frequency is shifted by up to only 5% and is even higher for the case with higher frequency changes. The results highlight the significance of implementation of a semi-active tuned mass damper for offshore wind turbines which are subjected to varying natural frequency due to gradual or sudden damage development. To implement the aforementioned structural control devices in the design of offshore wind turbines, more comprehensive studies with a focus on the experimental investigations and practicalities of these devices are needed. Furthermore, the maintenance requirements of these devices should be investigated in the scope of total maintenance regime of the offshore wind turbine.

Chapter 7 Conclusions and Recommendations

7.1 Achievements against the objectives

The ultimate goal of this research was to create numerical models for fixed offshore wind turbine foundations (jackets and monopiles) equipped with vibration control devices in time domain considering non-linear soil-pile interaction and then investigate the effect of different types of vibration control devices on the overall behaviour of the system under harmonic and stochastically generated loadings. Furthermore, another goal was to estimate the reduced fragility of the system equipped with vibration control devices under multi-hazard conditions using multiple stripe analysis. Finally, the last goal was to compare the behaviour of semi-active vibration control devices with passive vibration control devices.

Throughout this research conducted for vibration control of offshore wind turbine foundations, several concluding statements have been derived, which are concisely summarized in the upcoming.

- Lumped mass model can be used for the conceptual design of offshore wind turbine jackets in order to find the optimum configuration based on the limit states imposed by the relevant standards. A detailed parametric study was performed to investigate the effect of the important configurations and geotechnical parameters on the natural frequencies. The first natural frequency of the jacket OWT is slightly affected by the soil stiffness. Therefore, this type of foundations may be suitable for soil conditions with weak mechanical properties.
- A model for offshore wind turbine monopiles based on the Timoshenko beam element is developed and a verification study is performed. There is a very good agreement between the results of natural frequency analyses. Some parametric studies concerning the effect of main variables such as embedded pile depth, pile diameter, pile thickness, water depth, and soil stiffness on the natural frequencies of the system are performed.

- The results show that heavier tuned mass dampers dampen out a wider range of applied frequencies, however, they increase the vibration amplitudes for loading frequencies outside that bandwidth in a larger extent. Since TMDs are more efficient in operational conditions, and TLCDs have better performance in parked conditions and due to the fact that the total fatigue damage is caused by the contribution of all these conditions, the combined TLCD-TMD can introduce better overall performance in whole lifetime of the system. The combined system can consist of a TMD installed in the nacelle and a TLCD installed inside the tower.
- With regard to fragility analysis, three limit state thresholds corresponding to high, medium and low sensitive equipment are defined. Multiple stripes analysis approach is utilized to construct empirical cumulative distribution. Having used the Likelihood Maximization approach, the fragility function curves are obtained for the predefined limit states. The fragility values decrease with the inclusion of the tuned liquid column damper for all cases, resulting in a boost in the reliability of the system under multi-hazard conditions. However, this fragility reduction varies for different limit states and intensity measures. The maximum fragility reduction is observed for medium and high sensitive equipment up to 13%. The corresponding values for low sensitive equipment are lower. Furthermore, the results show that the fragility reduction offered by the tuned liquid column dampers is higher for low-intensity earthquakes. In addition, the corresponding values for the parked condition are larger due to the lack of aerodynamic damping in this condition. Therefore, the implementation of an optimal TLCD can increase the overall reliability of the system, especially for parked conditions under low-intensity earthquake motions. Consequently, it reduces downtime and maintenance needs resulting in higher rates of energy conversion.
- A numerical model for offshore wind turbines controlled by semi-active tuned mass dampers (STMD) subjected to wind, wave, and earthquake excitations considering time-variant damage development are presented. Short-time Fourier transform (STFT) is utilized to identify the changes in the natural frequency of the system and to retune the semi-active tuned mass damper. Time-variant stiffness and damping of STMD are modified in each time step

according to a vibration control algorithm based on short-time Fourier transform. Numerical analyses are carried out for operational and non-operational conditions to investigate the performance of STMD compared to the PTMD under multi-hazards. Dynamic responses for a single earthquake record as well as a set of earthquake records are presented. The results show that STMDs perform significantly better than PTMDs, especially when there is a change in the natural frequency of the system. A semi-active tuned mass damper with a mass ratio of 1% shows much better performance than a passive tuned mass damper with a mass ratio of 4%. A semi-active tuned mass damper with a mass ratio of 2% can reduce the standard deviation of the displacement and base overturning moment up to 20% and 16%, respectively. However, its passive counterpart increases the dynamic responses when there is a change in the natural frequency of the system due to damages. This significant difference between the performances of the passive and semi-active devices is for the case when the natural frequency is shifted by up to only 5% and is even higher for the case with higher frequency changes. The results highlight the significance of implementation of a semi-active tuned mass damper for offshore wind turbines which are subjected to varying natural frequency due to gradual or sudden damage development.

7.2 Gaps and recommended future work

As a consequence of the time constraints, some interesting aspects within the framework of offshore wind turbines were disregarded. Nevertheless, in this last section of the document, some further steps for future implementation are brought to light.

- Other types of vibration control devices could be considered. A comprehensive study concerning the feasibility of implementation of the vibration control devices in terms of space needed in the nacelle and tower is necessary.
- Other limit states such as fatigue considerations could be considered in the fragility analysis.
- The maintenance requirements of these devices could be investigated in the scope of total maintenance regime of the offshore wind turbine.

- Concerning fragility analysis, other methods such as incremental fragility analysis could be used and compared with Multiple Stripe Analysis method.
- With regard to the way seismic motion is applied to the embedded piles, more advanced methods such as free field analysis could be used due to the fact that applying identical input ground motions to all the embedded pile supports may lead to underestimation of seismic loading because of multi-layer nature of soil.
- To implement the aforementioned structural control devices in the design of offshore wind turbines, more comprehensive studies with a focus on the experimental investigations and practicalities of these devices are needed.
- More comprehensive studies with a focus on experimental investigations may be useful.

7.3 Novelty and contribution to the field

Owing to the high number members and joints in jacket foundations, the task of performing dynamic structural analysis of offshore wind jackets is time consuming and requires huge computational effort. Therefore, using conventional finite element methods especially in conceptual design is computationally expensive. A model based on lumped mass modelling is developed and used in this research for some parametric studies as well as for investigating the influence of vibration control devices on the overall behaviour of the system.

The literature was lacking of combined TLCD-TMD in which two types of vibration control devices are used simultaneously to mitigate excessive vibration of offshore wind turbine systems. In this research, the application of TLCD-TMD was studied. Also, the effect of vibration control devices on the behaviour of offshore wind turbines under a wide range of loading conditions such as operational, parked, startup and shutdown is investigated.

With regard to fragility analysis, the application of using Multiple Stripe Analysis for performing fragility analysis of offshore wind turbines equipped with vibration control devices under multi-hazard conditions is investigated. The reduced fragility of the systems due to the implementation of vibration control devices is also studied.

With regard to study on semi-active vibration control systems for offshore wind turbines under multi-hazard conditions, the previous studies were limited to only one earthquake record and their model was based on a very simplistic soil pile interaction. In this research, a suite of earthquake records with different frequency contents and intensities is used. Furthermore, more advanced soil–pile interaction model based on time-variant nonlinear stiffness considering soil damage phenomena enhanced the previous works. In addition, the effect of semi-active tuned mass dampers on other structural responses such as base shear and base moment is also investigated.

7.4 Research outputs

- **Arash Hemmati** and Oterkus, Erkan (2018) "Semi-active structural control of offshore wind turbines considering damage development". Journal of Marine Science and Engineering, 6 (3). ISSN 2077-1312

- **Arash Hemmati**, Erkan Oterkus, Mahdi Khorasanchi (2019)"Vibration suppression of offshore wind turbine foundations using tuned liquid column dampers and tuned mass dampers". Ocean Engineering, 172 286-295.

- **Arash Hemmati**, Erkan Oterkus, Nigel Barltrop., "Fragility reduction of offshore wind turbines using tuned liquid column dampers" Journal of Soil Dynamics and Earthquake Engineering, *under revision*.

- **Arash Hemmati**, Mahdi Khorasanchi, Nigel Barltrop., "Analysis of offshore wind turbine foundations with soil damping models" Proceedings of the 36th International Conference on Ocean, Marine and Arctic Engineering June 25-30, 2017, Trondheim, Norway.

- **Arash Hemmati**, Erkan Oterkus, Mahdi Khorasanchi., "Effect of tuned mass dampers on fixed offshore wind turbine foundations" Wind Europe Conference, Nov 28-30, 2017, Amsterdam, Netherlands.

- **Arash Hemmati**, Mahdi Khorasanchi, Nigel Barltrop., "Offshore wind turbine foundation design including soil damping models" Offshore Wind Conference Jun 6-8, 2017, London, UK.

- **Arash Hemmati**, Erkan Oterkus, "Vibration control of fixed offshore wind turbines using structural control devices" All-energy conference, 2-3 May, 2018, Glasgow, UK.

- **Arash Hemmati**, Mahdi Khorasanchi, Nigel Barltrop., "Investigation of effect of soil damping on non-slender piles for offshore wind turbine foundations" All-energy conference, 10-11 May, 2017, Glasgow, UK.

References

1. *International Energy Agency*. Key trends and statistics 2018]; Available from: https://www.iea.org/statistics/.

2. *WindEurope*. Offshore Wind in Europe: Key trends and statistics 2017 2018]; Available from: https://windeurope.org/.

3. Symans, M.D. and M.C. Constantinou, *Semi-active control systems for seismic protection of structures: a state-of-the-art review.* Engineering Structures, 1999. **21**(6): p. 469-487.

4. Chen, J.-L. and C.T. Georgakis, *Spherical tuned liquid damper for vibration control in wind turbines.* Journal of Vibration and Control, 2013. **21**(10): p. 1875-1885.

5. Lackner, M., M. Rotea, and R. Saheba, *Active Structural Control of Offshore Wind Turbines*, in *48th AIAA Aerospace Sciences Meeting Including the New Horizons Forum and Aerospace Exposition*. 2010, American Institute of Aeronautics and Astronautics.

6. Fitzgerald, B., B. Basu, and S.R.K. Nielsen, *Active tuned mass dampers for control of in-plane vibrations of wind turbine blades.* Structural Control and Health Monitoring, 2013. **20**(12): p. 1377-1396.

7. Fitzgerald, B. and B. Basu, *Active Tuned Mass Damper Control of Wind Turbine Nacelle/Tower Vibrations with Damaged Foundations.* Key Engineering Materials, 2013. **569-570**: p. 660-667.

8. Staino, A. and B. Basu, *Dynamics and control of vibrations in wind turbines with variable rotor speed.* Engineering Structures, 2013. **56**: p. 58-67.

9. Krenk, S., M.N. Svendsen, and J. Høgsberg, *Resonant vibration control of three-bladed wind turbine rotors.* AIAA journal, 2012. **50**(1): p. 148-161.

10. Maldonado, V., et al., *Active Vibration Control of a Wind Turbine Blade Using Synthetic Jets.* International Journal of Flow Control, 2009. **1**(4).

11. Fitzgerald, B. and B. Basu, *Cable connected active tuned mass dampers for control of in-plane vibrations of wind turbine blades.* Journal of Sound and Vibration, 2014. **333**(23): p. 5980-6004.

12. Kareem, A., T. Kijewski, and Y. Tamura, *Mitigation of motions of tall buildings with specific examples of recent applications.* Wind and structures, 1999. **2**(3): p. 201-251.

13. Lackner, M.A. and M.A. Rotea, *Structural control of floating wind turbines.* Mechatronics, 2011b. **21**(4): p. 704-719.

14. Yilmaz, O.C., *The Optimization of Offshore Wind Turbine Towers Using Passive Tuned Mass Dampers*. 2012, University of Massachusetts.

15. Stewart, G.M. and M.A. Lackner, *The impact of passive tuned mass dampers and wind–wave misalignment on offshore wind turbine loads.* Engineering Structures, 2014. **73**: p. 54-61.

16. Stewart, G. and M. Lackner, *Offshore Wind Turbine Load Reduction Employing Optimal Passive Tuned Mass Damping Systems.* IEEE Transactions on Control Systems Technology, 2013. **21**(4): p. 1090-1104.

17. Lackner, M.A. and M.A. Rotea, *Passive structural control of offshore wind turbines.* Wind Energy, 2011a. **14**(3): p. 373-388.

18. Enevoldsen, I. and K. Mørk, *Effects of a vibration mass damper in a wind turbine tower.* Journal of Structural Mechanics, 1996. **24**(2): p. 155-187.

19. Murtagh P. J, et al., *Passive control of wind turbine vibrations including blade/tower interaction and rotationally sampled turbulence.* Wind Energy, 2008. **11**(4): p. 305-317.

20. He, E.M., Ya Qi Hu, and G.L.Y. Yang Zhang, *Vibration and Load Suppression of Offshore Floating Wind Turbine.* Advanced Materials Research, 2014. **1025-1026**: p. 891-896.

21. Fitzgerald, B., S. Sarkar, and A. Staino, *Improved reliability of wind turbine towers with active tuned mass dampers (ATMDs).* Journal of Sound and Vibration, 2018. **419**: p. 103-122.

22. Arrigan John, et al., *Control of flapwise vibrations in wind turbine blades using semi-active tuned mass dampers.* Structural Control and Health Monitoring, 2011. **18**(8): p. 840-851.

23. Dinh, V.-N. and B. Basu, *Passive control of floating offshore wind turbine nacelle and spar vibrations by multiple tuned mass dampers.* Structural Control and Health Monitoring, 2015. **22**(1): p. 152-176.

24. Zuo, H., K. Bi, and H. Hao, *Using multiple tuned mass dampers to control offshore wind turbine vibrations under multiple hazards.* Engineering Structures, 2017. **141**: p. 303-315.

25. Sun, C., *Semi-active control of monopile offshore wind turbines under multi-hazards.* Mechanical Systems and Signal Processing, 2018. **99**: p. 285-305.

26. Bauer, H.F., *Oscillations of immiscible liquids in a rectangular container: a new damper for excited structures.* Journal of Sound and Vibration, 1984. **93**(1): p. 117-133.

27. Sakai, F., S. Takeda, and T. Tamaki. *Tuned liquid column damper-new type device for suppression of building vibrations*. in *Highrise Buildings*. 1989. Nanjing, China.

28. Welt, F. and V. Modi, *Vibration damping through liquid sloshing, Part I: a nonlinear analysis.* Journal of vibration and acoustics, 1992. **114**(1): p. 10-16.

29. Fujino, Y., et al., *Tuned liquid damper (TLD) for suppressing horizontal motion of structures.* Journal of Engineering Mechanics, 1992. **118**(10): p. 2017-2030.

30. Lepelletier, T. and F. Raichlen, *Nonlinear oscillations in rectangular tanks.* Journal of Engineering Mechanics, 1988. **114**(1): p. 1-23.

31. Yalla, S.K. and A. Kareem, *Optimum absorber parameters for tuned liquid column dampers.* Journal of Structural Engineering, 2000. **126**(8): p. 906-915.

32. Ghaemmaghami, A.R., R. Kianoush, and O. Mercan, *Numerical modeling of dynamic behavior of annular tuned liquid dampers for the application in wind towers under seismic loading.* Journal of Vibration and Control, 2015. **22**(18): p. 3858-3876.

33. Colwell, S. and B. Basu, *Tuned liquid column dampers in offshore wind turbines for structural control.* Engineering Structures, 2009. **31**(2): p. 358-368.

34. Zhang, Z., B. Basu, and S.R.K. Nielsen, *Tuned liquid column dampers for mitigation of edgewise vibrations in rotating wind turbine blades.* Structural Control and Health Monitoring, 2015. **22**(3): p. 500-517.

35. J, A. and B. B. *Vibration control of wind turbine blades using tuned liquid dampers*. in *the eleventh international conference on civil, structural and environmental, engineering computing*. 2007. Stirlingshire, UK.

36. Mensah, A.F. and L. Dueñas-Osorio, *Improved reliability of wind turbine towers with tuned liquid column dampers (TLCDs).* Structural Safety, 2014. **47**: p. 78-86.

37. Karimi, H.R., M. Zapateiro, and N. Luo. *Semiactive vibration control of offshore wind turbine towers with tuned liquid column dampers using H output feedback control*. in *2010 IEEE International Conference on Control Applications*. 2010.

38. Sonmez, E., et al., *A study on semi-active Tuned Liquid Column Dampers (sTLCDs) for structural response reduction under random excitations.* Journal of Sound and Vibration, 2016. **362**: p. 1-15.

39. Prowell, I., et al., *Experimental and numerical seismic response of a 65 kW wind turbine.* Journal of Earthquake Engineering, 2009. **13**(8): p. 1172-1190.

40. Prowell, I., et al., *Shake table testing and numerical simulation of a utility-scale wind turbine including operational effects.* Wind Energy, 2014. **17**(7): p. 997-1016.

41. Zhao, X. and P. Maisser, *Seismic response analysis of wind turbine towers including soil-structure interaction.* Proceedings of the Institution of Mechanical Engineers, Part K: Journal of Multi-body Dynamics, 2006. **220**(1): p. 53-61.

42. Zhao, X., P. Maißer, and J. Wu, *A new multibody modelling methodology for wind turbine structures using a cardanic joint beam element.* Renewable Energy, 2007. **32**(3): p. 532-546.

43. Bazeos, N., et al., *Static, seismic and stability analyses of a prototype wind turbine steel tower.* Engineering Structures, 2002. **24**(8): p. 1015-1025.

44. Witcher, D., *Seismic analysis of wind turbines in the time domain.* Wind Energy, 2005. **8**(1): p. 81-91.

45. Song, B., Y. Yi, and J.C. Wu, *Study on Seismic Dynamic Response of Offshore Wind Turbine Tower with Monopile Foundation Based on M Method.* Advanced Materials Research, 2013. **663**: p. 686-691.

46. Alati, N., G. Failla, and F. Arena, *Seismic analysis of offshore wind turbines on bottom-fixed support structures.* Philosophical Transactions of the Royal Society A: Mathematical, Physical and Engineering Sciences, 2015. **373**(2035).

47. Commission, I.E., *IEC 61400 Design requirements for offshore wind turbines*. 2009.

48. Jin, X., H. Liu, and W. Ju, *Wind Turbine Seismic Load Analysis Based on Numerical Calculation.* 2014, 2014. **60**(10): p. 11.

49. Nuta, E., C. Christopoulos, and J.A. Packer, *Methodology for seismic risk assessment for tubular steel wind turbine towers: application to Canadian seismic environment.* Canadian Journal of Civil Engineering, 2011. **38**(3): p. 293-304.

50. Mardfekri, M. and P. Gardoni, *Multi-hazard reliability assessment of offshore wind turbines.* Wind Energy, 2015. **18**(8): p. 1433-1450.

51. Kim, D.H., S.G. Lee, and I.K. Lee, *Seismic fragility analysis of 5 MW offshore wind turbine.* Renewable energy, 2014. **65**: p. 250-256.

52. Baker, J.W., *Efficient analytical fragility function fitting using dynamic structural analysis.* Earthquake Spectra, 2015. **31**(1): p. 579-599.

53. Jalbi, S., M. Shadlou, and S. Bhattacharya, *Chapter 16 - Practical Method to Estimate Foundation Stiffness for Design of Offshore Wind Turbines A2 - Letcher, Trevor M*, in *Wind Energy Engineering*. 2017, Academic Press. p. 329-352.

54. Zaaijer, M., *Foundation modelling to assess dynamic behaviour of offshore wind turbines.* Applied Ocean Research, 2006. **28**(1): p. 45-57.

55. Manuel, E.B.a.L. *Foundation Models for Offshore Wind Turbines*. in *47th AIAA Aerospace Sciences Meeting and The New Horizons Forum and Aerospace Exhibit*. 2009. Orlando, Florida.: American Institute for Aeronautics and Astronautics (AIAA).

56. Winkler, E., *The theory of the bending of beams on an elastic foundation.* Die Lehre von der Elastizität und Festigkeit, Prague, 1867: p. 182.

57. API-RP2A-WSD. *Recommended practice for planning, designing and constructing fixed offshore platforms working stress design* in *Twenty-*. 2000.

58. S. P. H. Sørensen, A.H.A. *Small-displacement soil-structure interaction for horizontally loaded piles in sand*. in *Proceedings of the 17th Nordic Geotechnical Meeting Challenges in Nordic Geotechnic*. 2016. Reykjavik, Iceland.

59. Sørensen, S.P.H., *Soil-Structure Interaction For Nonslender, Large-Diameter Offshore Monopiles*, in *Civil Engineering*. 2012, Aalborg University: Aalborg. p. 328.

60. Sørensen, S.P.H., L.B. Ibsen, and A.H. Augustesen. *Effects of diameter on initial stiffness of py curves for large-diameter piles in sand*. in *The European Conference on Numerical Methods in Geotechnical Engineering*. 2010. CRC Press LLC.

61. Kallehave, D., C.L. Thilsted, and M. Liingaard. *Modification of the API py formulation of initial stiffness of sand*. in *Offshore site investigation and geotechnics: integrated technologies-present and future*. 2012. Society of Underwater Technology.

62. Jonkman, J., et al., *Definition of a 5-MW Reference Wind Turbine for Offshore System Development*. 2009, National Renewable Energy Laboratory.

63. Thomson, W., *Theory of vibration with applications*. 2018: CrC Press.

64. Jonkman, J.M. and M.L. Buhl Jr, *FAST User's Guide-Updated August 2005*. 2005, National Renewable Energy Laboratory (NREL), Golden, CO.

65. Vorpahl, F., *Description of a basic model of the `UpWind reference jacket' for code comparison in the OC4 project under IEA Wind Annex 30*. 2013, Fraunhofer Institute for Wind Energy and Energy System Technology IWES.

66. De Vries, W.E.V., N.K. · Passon, P. · Fischer, T. · Kaufer, D. · Matha, D. · Schmidt, B. · Vorpahl, F., *Support Structure Concepts for Deep Water Sites*. 2011, Delft University of Technology.

67. Newmark, N.M., *A method of computation for structural dynamics.* Journal of the engineering mechanics division, 1959. **85**(3): p. 67-94.

68. Panzer, H., et al., *Generating a parametric finite element model of a 3D cantilever Timoshenko beam using MATLAB.* 2009, Lehrstuhl für Regelungstechnik.

69. Steinboeck, A., A. Kugi, and H. Mang, *Energy-consistent shear coefficients for beams with circular cross sections and radially inhomogeneous materials.* International Journal of Solids and Structures, 2013. **50**(11-12): p. 1859-1868.

70. Jonkman, J., W. Musial, and W. Musial, *Offshore Code Comparison Collaboration (OC3) for IEA Task 23 Offshore Wind Technology and Deployment*. 2010, National Renewable Energy Laboratory.

71. Doherty, P. and K. Gavin, *Laterally loaded monopile design for offshore wind farms.* Proc. Inst. Civ. Eng.-Energy, 2011. **165**(1).

72. DNV, *DNV-OS-J101 Design of Offshore Wind Turbine Structures*. 2014.

73. Reese, L.C., W.R. Cox, and F.D. Koop, *Analysis of laterally loaded piles in sand.* Offshore Technology in Civil Engineering Hall of Fame Papers from the Early Years, 1974: p. 95-105.

74. Murchison, J.M. and M.W. O'Neill. *Evaluation of py relationships in cohesionless soils*. in *Analysis and design of pile foundations*. 1984. ASCE.

75. Dobry, R., et al., *Horizontal stiffness and damping of single piles.* Journal of Geotechnical and Geoenvironmental Engineering, 1982. **108**(GT3).

76. Budhu, M. and T.G. Davies, *Nonlinear analysis of laterality loaded piles in cohesionless soils.* Canadian geotechnical journal, 1987. **24**(2): p. 289-296.

77. Poulos, H.G. and T.S. Hull. *The role of analytical geomechanics in foundation engineering*. in *Foundation engineering: Current principles and practices*. 1989. ASCE.

78. Ashford, S.A. and T. Juirnarongrit, *Evaluation of pile diameter effect on initial modulus of subgrade reaction.* Journal of Geotechnical and Geoenvironmental Engineering, 2003. **129**(3): p. 234-242.

79. Hald, T., et al. *Revisiting monopile design using py curves. Results from full scale measurements on Horns Rev*. in *Proceedings of European Offshore Wind 2009 Conference*. 2009.

80. Kaimal, J.C., et al., *Spectral characteristics of surface-layer turbulence.* Quarterly Journal of the Royal Meteorological Society, 1972. **98**(417): p. 563-589.

81. Murtagh, P.J., B. Basu, and B.M. Broderick, *Along-wind response of a wind turbine tower with blade coupling subjected to rotationally sampled wind loading.* Engineering Structures, 2005. **27**(8): p. 1209-1219.

82. Jonkman, B.J., *TurbSim user's guide: Version 1.50*. 2009, National Renewable Energy Lab.(NREL), Golden, CO (United States).

83. DNV, O.S.D.-O., *J101: Design of Offshore Wind Turbine Structures.* Det Norske Veritas, 2004.

84. (DNV), D.N.V., *DNV-RP-C205: environmental conditions and environmental load*. 2010: Norway.

85. Hasselmann, K., et al., *Measurements of wind-wave growth and swell decay during the Joint North Sea Wave Project (JONSWAP).* Ergänzungsheft 8-12, 1973.

86. Chiou, B., et al., *NGA project strong-motion database.* Earthquake Spectra, 2008. **24**(1): p. 23-44.

87. Wu, J.-C., et al., *Design guidelines for tuned liquid column damper for structures responding to wind.* Engineering Structures, 2005. **27**(13): p. 1893-1905.

88. Hu, Y. and E. He, *Active structural control of a floating wind turbine with a stroke-limited hybrid mass damper.* Journal of Sound and Vibration, 2017. **410**: p. 447-472.

89. Lavassas, I., et al., *Analysis and design of the prototype of a steel 1-MW wind turbine tower.* Engineering structures, 2003. **25**(8): p. 1097-1106.

90. Valamanesh, V. and A. Myers, *Aerodynamic damping and seismic response of horizontal axis wind turbine towers.* Journal of Structural Engineering, 2014. **140**(11): p. 04014090.

91. Ghafory-Ashtiany, M., M. Mousavi, and A. Azarbakht, *Strong ground motion record selection for the reliable prediction of the mean seismic collapse capacity of a structure group.* Earthquake Engineering & Structural Dynamics, 2011. **40**(6): p. 691-708.

92. Dueñas-Osorio, L. and B. Basu, *Unavailability of wind turbines due to wind-induced accelerations.* Engineering Structures, 2008. **30**(4): p. 885-893.

93. Choi, S.-K., *Reliability-based structural design [internet resource]*, ed. R.V. Grandhi, A.C. Robert, and Springerlink. 2007: London : Springer.

94. Porter, K., R. Kennedy, and R. Bachman, *Creating fragility functions for performance-based earthquake engineering.* Earthquake Spectra, 2007. **23**(2): p. 471-489.

95. Vamvatsikos, D. and C.A. Cornell, *Incremental dynamic analysis.* Earthquake Engineering & Structural Dynamics, 2002. **31**(3): p. 491-514.

96. Yalla, S.K., A. Kareem, and J.C. Kantor, *Semi-active tuned liquid column dampers for vibration control of structures.* Engineering Structures, 2001. **23**(11): p. 1469-1479.

97. Hrovat, D., P. Barak, and M. Rabins, *Semi-active versus passive or active tuned mass dampers for structural control.* Journal of Engineering Mechanics, 1983. **109**(3): p. 691-705.

98. Sun, C. and S. Nagarajaiah, *Study on semi-active tuned mass damper with variable damping and stiffness under seismic excitations.* Structural Control and Health Monitoring, 2014. **21**(6): p. 890-906.

99. Karnopp, D., M.J. Crosby, and R. Harwood, *Vibration control using semi-active force generators.* Journal of engineering for industry, 1974. **96**(2): p. 619-626.

100. Nagarajaiah, S. and E. Sonmez, *Structures with semiactive variable stiffness single/multiple tuned mass dampers.* Journal of Structural Engineering, 2007. **133**(1): p. 67-77.

101. Kirkegaard, P.H., et al. *Semiactive vibration control of a wind turbine tower using an MR damper*. in *Proceedings of The Fifth European Conference on Structural Dynamics*. 2002. Balkema Publishers, AA/Taylor & Francis The Netherlands.

102. Weber, F., *Dynamic characteristics of controlled MR-STMDs of Wolgograd Bridge.* Smart materials and structures, 2013. **22**(9): p. 095008.

103. Abe, M. and T. Igusa, *Semi-active dynamic vibration absorbers for controlling transient response.* Journal of Sound and Vibration, 1996. **198**(5): p. 547-569.

104. Sun, C., *Mitigation of offshore wind turbine responses under wind and wave loading: Considering soil effects and damage.* Structural Control and Health Monitoring, 2018. **25**(3).

105. Sadek, F., et al., *A method of estimating the parameters of tuned mass dampers for seismic applications.* Earthquake engineering and structural dynamics, 1997. **26**(6): p. 617-636.

106. Abramowitz, M. and I.A. Stegun, *Handbook of mathematical function: with formulas, graphs and mathematical tables*, in *Handbook of mathematical function: with formulas, graphs and mathematical tables*. 1965, Dover Publications.

Appendix A: Gaussian quadrature weights

The aim of this appendix is to describe the Gaussian quadrature (Legendre-Gauss quadrature) weights used in numerical modelling of soil pile interaction. This method is an approximate method of calculation of certain integral. The domain of numerical integration is normalized as $[-1,1]$. In this method, the function can be written as $f(x)=\omega(x)g(x)$ in which $g(x)$ is approximately polynomial and $\omega(x)$ is known. Then the function can be approximated by the following equation:

$$\int_{-1}^{1} f(x)dx = \int_{-1}^{1} \omega(x)g(x)dx \approx \sum_{i=1}^{n} \omega_i' g(x_i')$$

where ω_i' is weight, x_i' is the point and n is the number of points considered. For Gauss-Legendre quadrature method when $\omega(x)=1$, the weights can be obtained by the following formula base on the work by [106]:

$$\omega_i = \frac{2}{(1-x_i^2)\left[P_n'(x_i)\right]^2}$$

in which $P_n(x)$ is the associated polynomials: The following table tabulates the weights and points according to aforementioned formula for the number of points up to three. In this study four points are considered.

n	Points	weights
2	+0.577350	1
	-0.577350	1
3	+0.774597	0.555555
	0	0.88888
	-0.774597	0.555555
4	+0.861136	0.347855
	+0.339981	0.652145
	-0.339981	0.652145
	-0.861136	0.347855

Appendix B: Newmark's method for solving nonlinear systems

N. M. Newmark developed a time-stepping method to solve structural dynamics implicitly. This method is based on the following formula:

$$\dot{u}_{i+1} = \dot{u}_i + \left[(1-\gamma)\Delta t\right]\ddot{u}_i + (\gamma\Delta t)\ddot{u}_{i+1}$$

$$u_{i+1} = u_i + (\Delta t)\dot{u}_i + \left[(0.5-\beta)(\Delta t)^2\right]\ddot{u}_i + \left[\beta(\Delta t)^2\right]\ddot{u}_{i+1}$$

In these formula, the parameters β and γ are used to define the variation of acceleration over each time step. These parameters determine precision and stability of the solution. The aforementioned equations coupled with the equation of motions with some iterations are used at the end of each time step to compute deflection, velocity and acceleration at time $i+1$.

The Newmark's method for nonlinear systems can be explained briefly in the following.

1. Initial calculations
   1.1 State determination: $(f_S)_0$ and $(k_T)_0$
   1.2 $\ddot{u}_0 = \dfrac{p_0 - c\dot{u}_0 - (f_S)_0}{m}$
   1.3 Select Δt.
   1.4

$$a_1 = \frac{1}{\beta(\Delta t)^2}m + \frac{\gamma}{\beta\Delta t}c$$

$$a_2 = \frac{1}{\beta\Delta t}m + (\frac{\gamma}{\beta} - 1)c$$

$$a_3 = (\frac{1}{2\beta} - 1)m + \Delta t(\frac{\gamma}{2\beta} - 1)c$$

2. Calculations for each time instant, i=0,1,2,…
   2.1 Initialise $j = 1, u_{i+1}^{(j)} = u_i, (fs)_{i+1}^{(j)} = (fs)_i, and (k_T)_{i+1}^{(j)} = (k_T)_i$
   2.2 $\hat{p}_{i+1} = p_{i+1} + a_1 u_i + a_2\dot{u}_i + a_3\ddot{u}_i$
3. For each iteration, $j = 1, 2, 3...$
   3.1 $\hat{R}_{i+1}^{(j)} = \hat{p}_{i+1} - (fs)_{i+1}^{(j)} - a_1 u_{i+1}^{(j)}$
   3.2 Check convergence against criteria. If the criteria is met go to step 4; otherwise go to step 3.3
   3.3 $(\hat{k}_T)_{i+1}^{j} = (k_T)_{i+1}^{j} + a_1$
   3.4 $\Delta u^{(j)} = R_{i+1}^{j} \div (\hat{k}_T)_{i+1}^{(j)}$
   3.5 $u_{i+1}^{(j+1)} = u_{i+1}^{(j)} + \Delta u^{(j)}$
   3.6 State determinations: $(fs)_{i+1}^{(j+1)}$ and $(k_T)_{i+1}^{(j+1)}$

Replace j by $j+1$ and repeat the steps to determine final value of u_{i+1}

4. Calculations for acceleration and velocity

4.1 $\dot{u}_{i+1} = \frac{\gamma}{\beta\Delta t}(u_{i+1} - u_i) + (1 - \frac{\gamma}{\beta})\dot{u}_i + \Delta t(1 - \frac{\gamma}{2\beta})\ddot{u}_i$

4.2 $\ddot{u}_{i+1} = \frac{1}{\beta(\Delta t)^2}(u_{i+1} - u_i) - \frac{1}{\beta\Delta t}\dot{u}_i - (\frac{1}{2\beta} - 1)\ddot{u}_i$

5. Repeat for next time step. Replace i by $i+1$ and perform steps 2 to 4 for the next time step.

In these equations, γ and β Newmark parameters which are in the range of 0 and 1 and in order to achieve an unconditionally stable time integration analysis, the following should be met:

$\gamma \geq 0.5$

$\beta \geq 0.25(0.5 + \gamma)^2$